



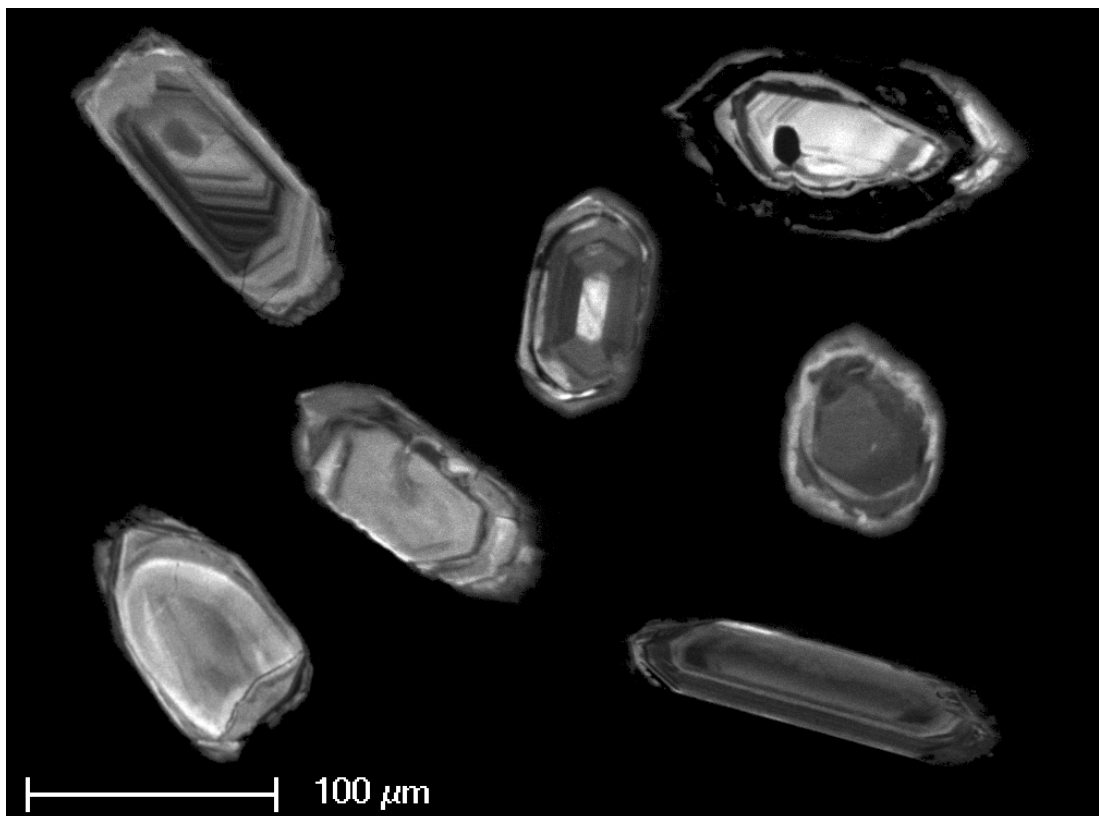
Stockholm
University

Master Thesis

Degree Project in
Geology 60 hp

Refining the geometry of the nappe stack in the Dora-Maira Massif (Western Alps): a petrological and geochronological study

Mikaela Krona



Stockholm 2023

Department of Geological Sciences
Stockholm University
SE-106 91 Stockholm

Acknowledgements

First of all, I want to express my gratitude to my supervisor Dr. Paola Manzotti for her guidance, support and mentorship during the writing of this thesis. She continues to be a source of inspiration in my studies. For this, I cannot thank her enough. I want to thank Dr. Fransesco Nosenzo for giving his expertise and assistance during lab work and for always taking time to answer all of my questions. I would also like to extend my thanks to Dr. Michel Ballèvre for offering his help and knowledge during the acquisition of the geochronological data. Many thanks to Dr. Marc Poujol for assisting with the laser ablation ICP-MS and recalculating the ages. I am grateful to Victoria Pease, for helping with the bulk-rock analysis. I want to thank Kerstin Lindén for her assistance with the zircon mounts. Also, I am thankful to have been a part of IGV during these years and I appreciate all the help from the administration.

There have been many people that I have gotten the chance to get to know during these five years at Stockholm University. I am grateful for all the moments spent with everyone in Geologklubben, with whom I've spent many laughs and hours of fun. In particular, I want to thank Bella, Elise and Sandra, who have been with me ever since that first day of university. You are the ones with whom I shared all the sweat, laughter and tears during my studies, and it would not have been the same without you. Last but not least, I would like to thank my family, who have supported me during the writing of this thesis and throughout my studies. Finally, a special mention to my partner Jonte, who is always there for me through thick and thin.

Abstract

The Alps is one of the most well-studied mountain belts on the Earth, but nonetheless there are areas which are still largely unexplored. The southern Dora-Maira Massif has been intensely studied since the discovery of coesite in 1984, whereas only a few studies focused on its northern sector. Recently, a new ultra-high pressure unit (i.e. the Chasteiran Unit) has been discovered in this part of the Massif, emphasizing the necessity to refine the geometry of the northern Dora-Maira Massif. Therefore, this study aims to define the different geological units and their tectonic boundaries in the Germanasca valley in northern Dora-Maira by combining petrological and geochronological data. Specifically, this thesis aims to assess if the area comprised between the Cialancia and Rabbioso bridges belongs to the Pinerolo Unit (a Carboniferous monocyclic unit) or if it is part of the Muret Unit (a Palaeozoic polycyclic unit).

In order to reach these aims, 32 samples were petrographically investigated and 4 samples out of 32 were selected for detailed geochronological investigations. These samples comprise i) a mylonitic orthogneiss located structurally above the Chasteiran Unit, and ii) three samples structurally located above the mylonitic orthogneiss, and collected between the Cialancia and Rabbioso bridges, namely two metasediments and a felsic layer interbedded with the metasediments. U-Pb dating of zircon from the mylonitic orthogneiss yielded an age of 442 ± 2 Ma interpreted to be the age of the magmatic protolith. This body is granitic/rhyolitic in composition and represents an Ordovician intrusion or a volcanic layer. Detrital zircon geochronology was conducted on the two metasediments, providing in both samples a main zircon population at 600-750 Ma and a Cambro-Silurian maximum age of deposition. U-Pb dating of the felsic layer does not provide conclusive geochronological results due to a large number of inherited zircons. These data suggest that the metasediments and thus the area between the Cialancia and Rabbioso bridges do not belong to the Carboniferous Pinerolo Unit, as previously thought, but more likely to the Muret Unit which lies on top of the newly discovered ultra-high pressure Chasteiran Unit. In conclusion, the magmatic protolith of the mylonitic orthogneiss is Ordovician whereas both metasediments display a main population of zircon at 600-750 Ma and a maximum age of deposition in Cambro-Silurian.

Keywords: zircon geochronology, U-Pb dating, Dora-Maira Massif, continental subduction, sediment provenance, bulk rock chemistry, petrography

Table of Contents

1	Introduction	3
2	Geological setting	5
2.1	The formation of the Western Alps	5
2.2	The Dora-Maira Massif	7
3	Theoretical background	9
3.1	U-Pb geochronology	9
3.2	Zircon: a geochronometer	10
3.2.1	Textures of zircon	12
4	Methods	13
4.1	Whole-rock geochemistry	14
4.2	Mineral separation	15
4.3	CL imaging	15
4.4	U-Pb dating of zircons	16
5	Results	18
5.1	Sample description	18
5.2	Petrography	23
5.2.1	GM213	23
5.2.2	GM214	24
5.2.3	CH2231A-B	25
5.2.4	CH2232A-B	26
5.2.5	CH2233A-B	27
5.2.6	CH2240(1-2)	28
5.2.7	CH2249(1-2)	29
5.3	Whole-rock geochemistry	30
5.4	Zircon textures and geochronology	34
5.4.1	GM213	34
5.4.2	GM214	35
5.4.3	CH2241	35
5.4.4	CH2240	37
5.4.5	CH2249	38
6	Discussion	39
6.1	Nature and timing of magmatism in the northern Dora-Maira Massif	39
6.2	Timing of sedimentation	40
6.3	Sediment provenance	41
6.4	Refining the geometry of the nappe stack	42
7	Conclusion and future perspectives	45
	References	46
	Appendix A: Sample preparation	53
	Appendix B: Petrographic descriptions	57
	Appendix C: Bulk rock chemistry	70
	Appendix D: U-Pb geochronology	71

1 Introduction

The study of orogenic belts is important to decipher the processes that cause exhumation of deeply buried rocks. The Western Alps provides an excellent study area for investigating these processes, with outstanding outcrop exposures and varying metamorphic grade. The discovery of coesite in the famous whiteschists in the southern Dora-Maira Massif (Chopin, 1984), had large implications on the tectonic model for the re-surfacing of ultra-high pressure (UHP) metamorphic rocks. Most importantly, it showed that not only the oceanic crust could undergo subduction but also the continental crust which was previously thought too buoyant to subduct. Apart from the discovery of UHP lithologies in metamorphic rocks deriving from continental material, the theory of continental subduction is supported by different lines of evidence from the ongoing India-Asia collision, such as mass-balance calculations (e.g. Ingalls et al., 2016) and seismic data (e.g. Schneider et al., 2013). The UHP terrain of the Western Gneiss Region in Norway represents another early discovery of exhumed continental crust (Smith, 1984).

There are many questions remaining regarding the mechanisms of continental subduction and subsequent exhumation. The order in which geological units are assembled have implications for the tectonic model of continental subduction. During subduction, the pre-existing crust might become dismembered and as a result, different slices of the subducting material will reach peak pressure-temperature (P-T) conditions at different dates (Bonnet et al., 2022). Therefore, the characterization of terrains which have undergone continental subduction is crucial in order to recognise its geometry which in turn will contribute to the understanding of their tectonic evolution. Finally, it allows to further constrain the model of continental subduction. While P-T estimations give insight on the metamorphic evolution, age constraints provide broader knowledge of the spatial extent of a unit and its geological history.

With time, zircon has proved to be one of the best tools for geochronologists due to its resistance to physical and chemical weathering (Corfu et al., 2003). The main reason that zircon is such a powerful tool in geochronology is because it can be dated using the uranium-lead (U-Pb) decay system. U-Pb dating is essentially three decay series that can be combined to obtain a statistically significant age (White, 2015). Geochronology using zircon and the U-Pb decay system has played a major role in interpreting the sedimentary record on a global scale in geological units where fossils are absent (Fedo et al., 2003). In combination with stratigraphic correlation and using fossils, the success of zircon geochronology revolutionized the development of the geological timescale (Bowring and Schmitz, 2003). In addition, technological advances during the 20th century has made zircon dating a cost-effective, precise and fast approach which led to a surge in geochronological studies in the last 20 years (Bowring and Schmitz, 2003; Košler and Sylvester, 2003).

Since the ground-breaking discovery of coesite, the southern Dora-Maira Massif has been intensely studied and its metamorphic history and structure is well defined (Groppo et al., 2019). By contrast, the northern Dora-Maria is less explored resulting in knowledge gaps in terms of its geometry and metamorphic history. However, recent efforts have led to a better understanding of the northern Dora-Maira. The latest development was the discovery of the new UHP sliver which structurally occupies the same position as the coesite-bearing unit in the southern Dora-Maira, but records 200°C lower temperature (Manzotti et al., 2022). In addition, the polycyclic Muret unit has been described in detail which represents the only unit that has been identified structurally on top of the lowermost Pinerolo Unit in the northern Dora-Maira Massif (Nosengo et al., 2022). However, there are still uncertainties remaining in the northern part of the massif.

The aim of this study is to further refine the geometry of the northern Dora-Maira Massif by combining petrological and geochronological data using samples from the Germanasca valley situated west of Torino (Fig. 1). Historically, the metasediments of the Germanasca valley (between the Cialancia and Rabbioso bridges) have been thought to belong to the basal unit of the massif, the Pinerolo Unit, of Carboniferous age (Bussy and Cadoppi, 1996). Although lacking geochronological data, the metasediments were hypothesized to be Permian in age. On the contrary, recent findings (e.g. Manzotti et al., 2022) suggest that these metasediments belong to the polycyclic Muret Unit. Specifically, this study aims to test this interpretation on the basis of the age of the igneous protolith and the maximum age of deposition of the sediments now constituting the metasedimentary rocks in the Germanasca valley. In addition, it will contribute to better understanding of the tectonic evolution of the northern Dora-Maira Massif. These aims will be achieved through petrological characterization of 32 samples collected in the Germanasca valley. Moreover, a few selected samples will be investigated by geochronology and geochemistry. Finally, a provenance analysis will be conducted on the metasediments with the aim of reconstructing the geological history of the sediments.

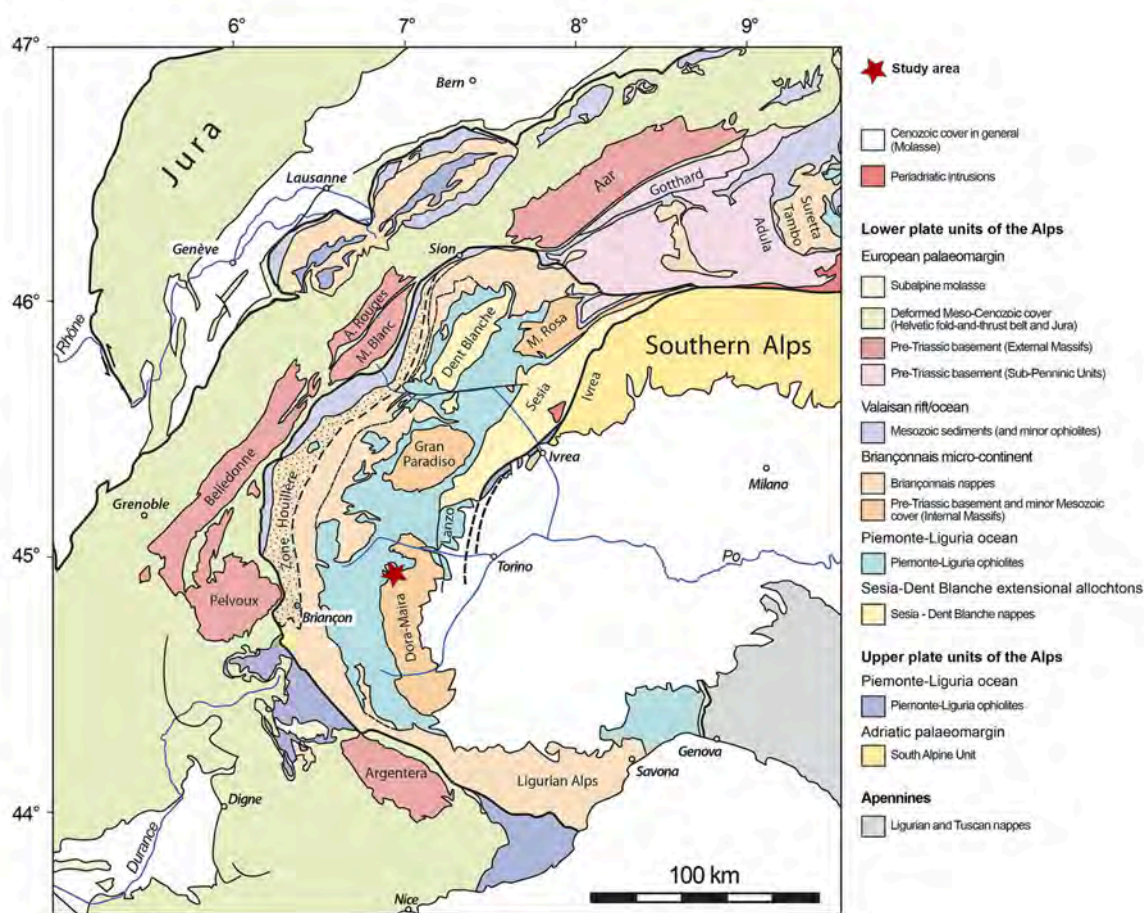


Figure 1: Geological map of the Western Alps, modified from Ballèvre et al. (2018). The studied area (red star) is located in the northernmost sector of the Dora-Maira Massif.

2 Geological setting

2.1 The formation of the Western Alps

The Alpine mountain belt extends across central Europe and stretches through eight countries. It is considered to have formed by nappe stacking, where sheets are thrust on top of the continental shelf during collision. The area now exposed in the Alpine belt was previously involved in the Variscan orogeny (370-290 Ma) which affected most of central and south-western Europe. During the Variscan orogeny, the collision between Gondwana and Laurasia, caused by the closing of the Rheic Ocean, formed the supercontinent Pangea. Additionally, the Variscan orogeny involved several microcontinents which drifted from the Gondwana paleo-margin during the opening of the Rheic Ocean and were caught up in the orogeny at a later stage (Franke et al., 2021). Many units now exposed in the Alpine belt are considered to derive from these drifted microcontinents which are sometimes referred to as the European Hun Superterrane (von Raumer et al., 2003). In Alpine terminology, the deformation within the Palaeozoic basement is referred to as pre-Alpine, because in most cases its exact age cannot be established.

The Alpine belt results from the collision between the Eurasian and Adriatic plate which is still active today, where Adria constitutes the overriding plate. The Adriatic plate consists of both continental and oceanic parts and lies in between the European and African plate (Handy et al., 2010). Following the Variscan orogeny, the opening of the Piemonte-Liguria Ocean during mid-Jurassic lead to breakup of the continental crust of Pangea (Ballèvre et al., 2018). The Piemonte-Liguria basin was located south of the European paleo-margin and separated the Eurasian and Adriatic plate. During the Early Cretaceous, a microcontinent called the Briançonnais plate drifted from the European paleo-margin, caused by the opening of the Valaisan basin during the Cretaceous (Fig. 2) (Rosenbaum and Lister, 2005). The Piemonte-Ligurian and Valaisan basins are often termed the Alpine Tethys in classic Alpine nomenclature. The Alpine orogeny was initiated in Late Cretaceous with the closing of the Alpine Tethys Ocean which subducted underneath the Adriatic plate (Piaz et al., 2003). The closure of the Alpine Tethys Ocean occurred in stages. The Piemonte-Liguria basin, the Briançonnais microcontinent and the Valaisan basin were successively subducted which ultimately lead to the onset of collision during the Eocene (Handy et al., 2010). Following subduction, parts of the consumed crust was metamorphosed at HP or UHP conditions before resurfacing.

The Alps is traditionally subdivided in three geological domains, from East to West, these are; i) the Austroalpine nappes, ii) the Penninic domain (detailed below) and iii) the Helvetic zone. The Austroalpine nappes derive from the distal part of the Adriatic passive margin (Schmid et al., 2004). The Penninic domain is a metamorphic nappe system deriving from the subducting plate on the European distal margin. The Helvetic zone represents the former European proximal margin (Ballèvre et al., 2018). In classic Alpine nomenclature, the Penninic domain denotes the various units in the internal Western Alps. From top to bottom these are i) the Upper Penninic domain which is made of ophiolites deriving from the Piemonte-Liguria Ocean, ii) the Middle Penninic domain constitutes units from the Briançonnais microcontinent, iii) the Lower Penninic domain that mainly consists of Mesozoic sediments derived from the Valaisan basin and iv) the Subpenninic domain which consists of units from the distal European margin (Handy et al., 2010; Piaz et al., 2003). The units of the Upper Penninic domain were thrust over the Briançonnais units, but the Internal Crystalline Massifs (Dora-Maira, Gran Paradiso and Monte Rosa), crop out as windows in the oceanic units deriving from the Piemonte-Liguria basin (Manzotti et al., 2014).

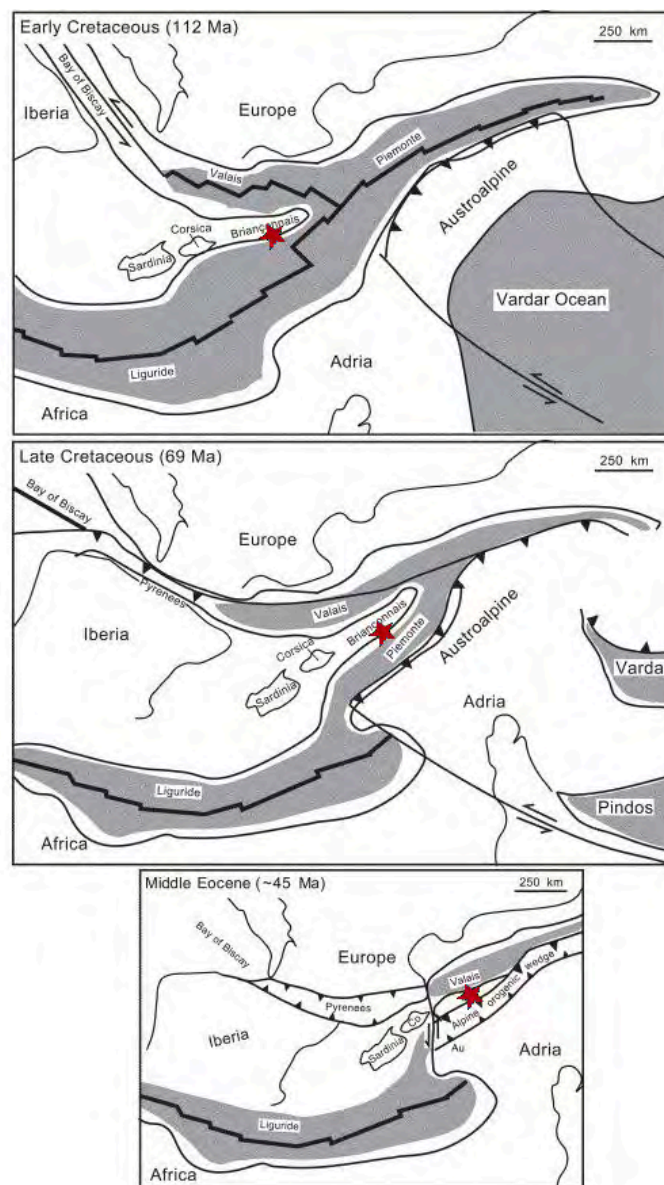


Figure 2: A reconstruction of the evolution of the Western Alps from the Early Cretaceous to Middle Eocene. The approximate location of the Dora-Maira Massif is indicated. Modified from Rosenbaum and Lister (2005).

2.2 The Dora-Maira Massif

The Dora-Maira Massif is located in the Western Alps and is geographically defined by the Dora Riparia River in the north and the Maira river in the south. The Dora-Maira Massif belongs to the Internal Crystalline Massifs, which is thought to derive from the Briançonnais microcontinent (Fig. 1). The approximate location of the Dora-Maira Massif during the Alpine orogeny is indicated in Figure 2. Hence, it belongs to the Middle Penninic domain, together with the other Internal Massifs; the Monte Rosa and Gran Paradiso Massifs (Fig. 1) (Schmid et al., 2004). Essentially, the Dora-Maira Massif consists of a Palaeozoic basement with remnants of a Mesozoic cover (Fig. 3) (Sandrone et al., 1993). The lowermost unit in the Dora-Maira nappe stack is the Pinerolo Unit, a monocyclic basement mainly consisting of graphite-rich conglomeratic schists which is intruded by Permian granites and granodiorites (Henry et al., 1993; Schmid et al., 2004). These meta-conglomerates interlayered with graphite is a typical lithology for Carboniferous basins (Opluštil et al., 2013), and the youngest detrital zircon in the Pinerolo Unit is indeed Carboniferous (330 Ma) in age (Manzotti et al., 2016).

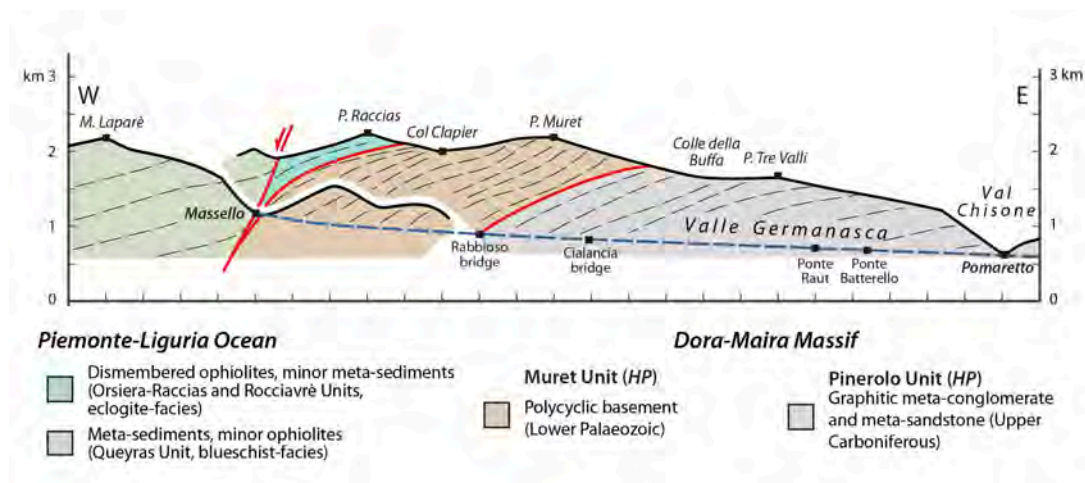


Figure 3: Cross-section of the nappe stack as exposed in the Germanasca valley prior to the discovery of the the UHP Chasteiran Unit. The figure is modified from Manzotti et al. (2022).

In the southern Dora-Maira, several units that lie structurally on top of the Pinerolo Unit are defined. These include the San Chiaffredo, Brossasco-Isasca, Rocca Solei and Dronero-Sampeyre Units. They are separated by sheared calcschists and metaophiolite slivers (Bonnet et al., 2022, and references therein). Amongst these, the Brossasco-Isasca Unit equilibrated at UHP conditions during the Alpine orogeny (Chopin, 1984). Recently, Groppo et al. (2019) revised the previously calculated P-T conditions for all units in the southern Dora-Maira. It was found that San Chiaffredo, Rocca Solei and Pinerolo have experienced eclogite-facies metamorphism at peak P-T conditions of 500-520 °C and 20-24 kbar whereas the Dronero-Sampeyre experienced blueschist facies at peak P-T conditions of 450-420 °C and 17-18 kbar (e.g. Avigad et al., 2003; Chopin et al., 1991). The UHP Brossaco-Isasca Unit displays peak P-T conditions of 35-40 kbar and 700-750 °C (Bonnet et al., 2022).

Contrary to the southern sector of the Dora-Maira Massif, the geometry of the nappe stack in the northern sector is less well defined. Here, one unit (i.e. the Muret Unit, Nosenzo et al., 2022) has been described so far which lies structurally on top of the Pinerolo Unit (Fig. 3). The Muret Unit is generally considered to correlate to the Rocca Solei or Dronero-Sampeyre Units in the southern part of the Massif (Bonnet et al., 2022). The polycyclic orthogneiss of the Muret Unit has been dated to 457 Ma (Bussy and Cadoppi, 1996) and 442 Ma (Nosenzo et al., 2022). The difference in ages is likely related to the difference in methodology, where the first authors

2022). Thermodynamic modelling of the polycyclic micaschist in the Muret Unit indicated Variscan metamorphism at 6-7 kbar and 650 °C which equates amphibolite facies (Nosenzo et al., 2022).

There are numerous inherited magmatic ages obtained in the Dora-Maira Massif, most commonly being Ordovician to Devonian or Permian (Bonnet et al., 2022, and references therein). However, in the Internal Massifs the most commonly occurring magmatism is Permian (e.g. Gran Paradiso: Ring et al., 2005, Dora-Maira: Chen et al., 2017) whereas reports of Ordovician magmatism are scarce. By contrast, Ordovician magmatism is widespread in the Alpine belt (von Raumer et al., 2002) which is thought to relate to the drifting of continental blocks from the northern Gondwana paleo-margin associated with the opening of the Rheic Ocean in the Early Ordovician and the Paleo-Tethys Ocean in the Late Ordovician.

A new UHP unit was recently discovered, namely the Chasteiran Unit which is exposed in the hanging wall of the Pinerolo Unit (Manzotti et al., 2022), structurally below the Muret Unit. The Chasteiran Unit is a 5-10 m thick sliver and occurs above the contact with the Pinerolo Unit (Fig. 4b). It consists of garnet-chloritoid graphite-rich micaschists. In the garnet, small (less than 20 μm long) pristine coesite crystals were found as well as quartz inclusions with radial cracks, indicating relict coesite. The UHP Chasteiran Unit records peak metamorphism at 27-28 kbar and 510-530 °C, which is around 200 °C colder compared to Brossasco-Isasca Unit in the south (Manzotti et al., 2022). There is currently no age constraint for the Chasteiran Unit. Finally, a fourth unit, namely the Serre Unit (Manzotti et al., 2022), consists of dolomite, marble, calcschists and ankerite-micaschists and is structurally located on top of the Muret Unit. To sum up, recent investigation proposed a new architecture for the northern Dora-Maira Massif that from bottom to top comprises the Pinerolo, Chasteiran, Muret, and Serre Units. Specifically, the rocks outcropping between Cialancia and Rabbioso bridges belong to the Pinerolo Unit in a first hypothesis (Fig. 3) and to the Muret Unit in a second hypothesis (Fig. 4).

3 Theoretical background

3.1 U-Pb geochronology

Uranium-lead (U-Pb) dating is based on three decay series whereby different uranium and/or thorium (Th) isotopes evolve into their respective daughter isotopes with several interstitial decay products (Table 1). The strength of the U-Pb system is that it can provide three different age constraints. By measuring the isotope ratios, ages can be obtained from ^{238}U - ^{206}Pb , ^{235}U - ^{207}Pb and ^{232}Th - ^{208}Pb . The age is calculated by an isochron, which gives a line which only depends of time (t). The isochron is based on two assumptions; 1) the system was at equilibrium at $t=0$ and 2) the system remained closed between t_0 and t (White, 2015). The general equation for an isochron (eq. 1) requires knowledge of the original ratio (R_0), the ratio of parent to daughter ($R_{P/D}$) and the decay constant (λ). Hence, by measuring the amount of daughter isotopes compared to the amount of parent isotope and with knowledge of the half-lives, the time that have passed since the start of the decay can be calculated. The age determination is based on secular equilibrium; that the production rate of the daughter and decay rate of the parent remains equal.

$$R = R_0 + R_{P/D}(e^{\lambda t}-1) \quad (1)$$

A robust age can be obtained when combining two of the decay series, namely $^{206}\text{Pb}/^{238}\text{U}$ and $^{207}\text{Pb}/^{235}\text{U}$, with a so-called concordia diagram (Tera and Wasserburg, 1972; Wetherhill, 1956). In a concordia diagram, the concordia curve represents points where the ages for $^{206}\text{Pb}/^{238}\text{U}$

Table 1: The U-Pb system consists of three decay series. The half-lives are derived from Jaffey et al. (1971) and the λ constant is from White (2015). Note that the half-life is derived from $T_{1/2} = \frac{\ln(2)}{\lambda}$.

Parent	λ	Half-life	Daughter
^{232}Th	$4.948 * 10^{-11} \text{y}^{-1}$	14.01Ga	^{208}Pb
^{235}U	$9.8571 * 10^{-10} \text{y}^{-1}$	0.70Ga	^{207}Pb
^{238}U	$1.55125 * 10^{-10} \text{y}^{-1}$	4.47Ga	^{206}Pb

and $^{207}\text{Pb}/^{235}\text{U}$ are equal. Thus, if both systems yield the same age, the point will plot on the concordia curve and the age is concordant (White, 2015). If the age plots on the concordia curve the decay evolved in a closed system, however if the age plots above or below the curve it is indicative of open system behaviour (i.e discordance). There are many causes of discordance in the U-Pb system which includes mixed analysis, Pb loss, disequilibrium and initial Pb (Reiners et al., 2017). During geological history, a system might behave openly during for example alteration which may lead to a change in the U-Pb ratio. These processes may result in loss of either lead or uranium. As a consequence, the geochronological clock of the decay series is reset and gives an apparent age which may be older or younger than the true age depending on if the system lost lead or uranium. If the system has lost lead, it will give a younger apparent age and if it has lost uranium it will give an older apparent age. Pb-loss or inherited Pb is usually corrected for using the stable lead isotope ^{204}Pb . The respective calculations for the ages (t), assuming that correction for common lead has already been done are given in eq. 2. Pb* refers to radiogenic lead, which is the only lead of interest for dating purposes. λ is the respective decay constant for each uranium parent isotope.

$$\begin{aligned}
 ^{206}\text{Pb}^* &= ^{238}\text{U} \times (e^{\lambda_{238}t} - 1) \\
 ^{207}\text{Pb}^* &= ^{235}\text{U} \times (e^{\lambda_{235}t} - 1) \\
 ^{208}\text{Pb}^* &= ^{232}\text{Th} \times (e^{\lambda_{232}t} - 1)
 \end{aligned} \tag{2}$$

The effect of Pb loss on dating can be reduced by using a Pb-Pb isochron, which combines the ages for $^{206}\text{Pb}/^{238}\text{U}$ and $^{207}\text{Pb}/^{235}\text{U}$ (Faure and Mensing, 2003). It is useful, because the ratio between $^{235}\text{U}/^{238}\text{U}$ for terrestrial rocks on Earth is constant. The exact value is reported differently in the literature, varying from at 137.82 (Hiess et al., 2012) to 137.88 (White, 2015), with the latter being the recommended value. To visualize these ages, Tera and Wasserburg (1972) developed a new type of concordia diagram due to the difficulties in using the Wetherhill concordia on their lunar samples. The Tera-Wasserburg diagram requires no knowledge of the initial $^{206}\text{Pb}/^{204}\text{Pb}$ and $^{207}\text{Pb}/^{204}\text{Pb}$ ratios, meaning that it is useful when the error of common lead is large.

3.2 Zircon: a geochronometer

Zircon (ZrSiO_4) occurs naturally in igneous, sedimentary and metamorphic rocks. Although it is a minor constituent in most rocks, it contains useful information as a tracer of geological history and provenance (Cawood et al., 2012). It is a highly variable mineral in terms of its chemical composition and complex textures, but it is also extremely resistant to both chemical and mechanical weathering. Due to its persistence both on and in the Earth's crust, it is one of the most useful geochronometers in geology. It has been shown that it can withstand processes such as partial melting and regional metamorphism without completely losing its geological age signature making it one of the best recorders of Earth's history (Mezger and Krogstad, 1997).

Zircon incorporates uranium while excluding lead, meaning that it contains almost no common lead in its crystal structure. Since zircon does not incorporate Pb during crystallisation, there is commonly no need for a correction for common Pb when analysing zircon. In this case it can be assumed that $Pb \approx Pb^*$. However, if very high-precision is needed, the common Pb is corrected for using the stable isotope ^{204}Pb , as previously mentioned.

In an igneous system, crystallisation of zircon reflects the saturation of zirconium (Zr) in the melt and the occurrence of multiple dissolution fronts in the crystal indicates periods of super- and under-saturation of Zr (Hoskin and Schaltegger, 2003). During growth of zircon in an igneous system, several types of internal textures can develop (detailed in sec. 3.2.1). Magmatic processes active during crystallisation may also affect the composition of zircon. For example, there is a complete solid solution between zircon and hafnium ($HfSiO_4$), and the inclusion of hafnium in zircon increases with magmatic differentiation (Hoskin and Schaltegger, 2003). In addition, the trace elements obtained from igneous zircon or inherited cores can give an indication of the source rock (Belousova et al., 2002). A negative europium (Eu) anomaly is common in magmatic zircons in felsic rocks and is thought to be caused by the coexistence of feldspar which acts as a sink for Eu (Rubatto, 2002). Moreover, it has been shown that zircon can have lower rare earth element (REE) composition than expected due to the presence of another REE-enriched mineral, such as garnet (Schaltegger et al., 1999). One way of characterizing zircons is based on the Th/U ratio, which for magmatic zircons usually is >0.5 , however generally 0.3 is an accepted lower limit (Kirkland et al., 2015; Teipel et al., 2004). Zircons with a Th/U ratio <0.01 are viewed as metamorphic (Teipel et al., 2004). However, it has been suggested that the interpretation of the Th/U ratio requires careful consideration and that zircons cannot be solely classified as metamorphic based on the Th/U ratio (Möller et al., 2003). Möller et al. (2003) proposed other factors which during metamorphism could potentially influence the Th/U ratio in zircon, for example that the presence of other Th-concentrating minerals (e.g. monazite) may result in a low Th/U ratio in zircon. In addition, the authors discussed that higher Th/U ratios may reflect open system behavior or breakdown of other high Th/U minerals. Therefore, the textures in the analysed zircon must also be taken into consideration.

In a sedimentary rock, zircons are derived from erosion and transport from pre-existing rocks (Fedo et al., 2003). Hence, zircons are referred to as detrital since they have been deposited in the sediment prior to lithification. There is usually a large variation in the various zircons in a sedimentary unit since they could have formed during different periods and settings in geological history. There are various applications of detrital zircon geochronology such as constraining the age of the host sediment, reconstruct the origin of sediments (provenance) and the geological history of the rock from which the zircon was extracted (Gehrels, 2014). By definition, a sedimentary unit can be no older than the youngest zircon, meaning that it is often used to constrain the maximum depositional age. The shape of detrital age distributions has been shown to reflect the tectonic setting in which the sediment was deposited (Cawood et al., 2012). However, age patterns are heavily dependent on preservation potential which introduces a bias in the sedimentary record where collisional settings has the most favourable combination of magma generation and preservation potential (Hawkesworth et al., 2009). In sedimentary basins, older zircon grains represent the early history and there are often numerous zircon populations which reflect episodic accumulation of sediment (Cawood et al., 2012).

Finally, in metamorphic rocks zircon is often inherited from an igneous system but new growth can occur during metamorphism. In a meta-igneous rock or an igneous xenocrystic core, the inherited zircons reflect the age of the protolith and should correlate to periods of magmatic activity. During metamorphism, zircon can often persist and preserve its chemical composition for the most part but a metamorphic rim can form. It has been suggested that zircon partially dissolves during prograde metamorphism and re-precipitates during the retrograde path (Kohn et al., 2015). Meaning that the re-precipitated zircon produces a rim surrounding the preserved

magmatic core. Theoretically, this rim can be used to date the metamorphic event.

3.2.1 Textures of zircon

There are various textures which could form in zircons depending on what processes have affected it. The identification of textures is crucial because it can reveal different age domains that will yield a mixed age during analysis. These textures can be imaged using a cathodoluminescence (CL) detector in a Secondary Electron Microscopy (SEM). There is a negative correlation between U content and CL emission, meaning that U-rich domains will appear dark on the image. The following section is a description of the different textures that could occur in zircon. Most commonly, magmatic zircons display oscillatory zoning (Fig. 5a) and a homogeneous population whereas detrital zircons have larger differences between each grain due to the variation in source of the sediments (Rubatto and Gebauer, 2000). The oscillatory zoning results from variation in chemical composition during growth. The various layers reflect zones where the composition approaches pure Zr as opposed to zones with enrichment in trace elements (Corfu et al., 2003). The formation of growth zoning is thought to depend on several processes such as diffusion rates, the degree of supersaturation of the melt and state of oxidation (Mattinson et al., 1996). It is common with textural discontinuities along the growth zoning due to resorption of the original zoning (Fig. 5b) due to Zr undersaturation of the magma (Corfu et al., 2003). Another type of zoning common in magmatic zircons is sector zoning (Fig. 5c), where the prismatic and pyramidal sector of the crystal have different concentrations of U which is thought to be controlled by variation in growth rate (e.g. Krogh, 1982).

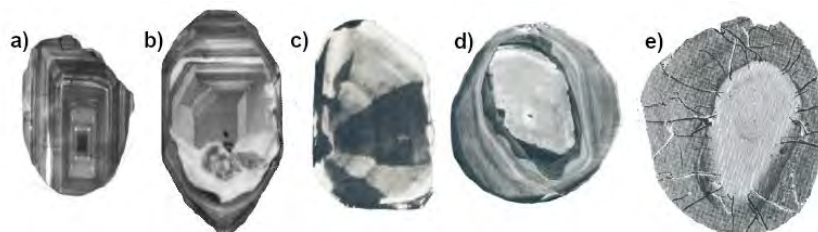


Figure 5: (a) Oscillatory zoning. (b) Re-homogenization along edges of a magmatic zircon. (c) Sector zoning. (d) Detrital core. (e) Radially fractured. The images are from Corfu et al. (2003) (and references therein).

Metamorphic zircons tend to be more rounded in shape and have weaker oscillatory zoning (Zheng et al., 2022). They can display a variety of internal textures caused by alteration, re-crystallization (e.g. dissolution-precipitation) and overgrowth (Rubatto, 2017). In poly-metamorphic terranes, detrital zircons may exhibit complex internal structures (Rubatto and Gebauer, 2000). The textures commonly observed in metamorphic zircons include convolute zoning, weak oscillatory zoning, dissolution fronts and transgressional features (Corfu et al., 2003). Often, they record several periods of growth which may result in the development of a detrital core surrounded by new growth (Fig. 5d). Fracturing commonly occurs due to volume expansion of the U-rich domains during differential metamictization (Fig. 5e). The fractured domains may serve as fluid pathways and promote alteration, which usually forms rounded textures that propagate along fractured or weak fronts. When zircons display fuzzy zones with varying CL emission, it is termed mosaic texture which develops due to metasomatic replacement of U-low domains by zircons richer in U (Corfu et al., 2003; Zheng et al., 2022). Zircons that have been altered by fluids have been reset and can be used to date the timing of fluid infiltration, but not to obtain the true age (Wu and Zheng, 2004). These zircons tend to show no, spongy or weak zoning. In summary, zircon in metamorphosed rocks can show a wide variety of textures which reflect the processes which have affected it during the metamorphic cycle.

4 Methods

The preparation of the samples for geochronology and bulk rock geochemistry consisted of several different steps. The details of each part will be described below. The instruments used for the sample preparation and analysis are shown in Figure 6.

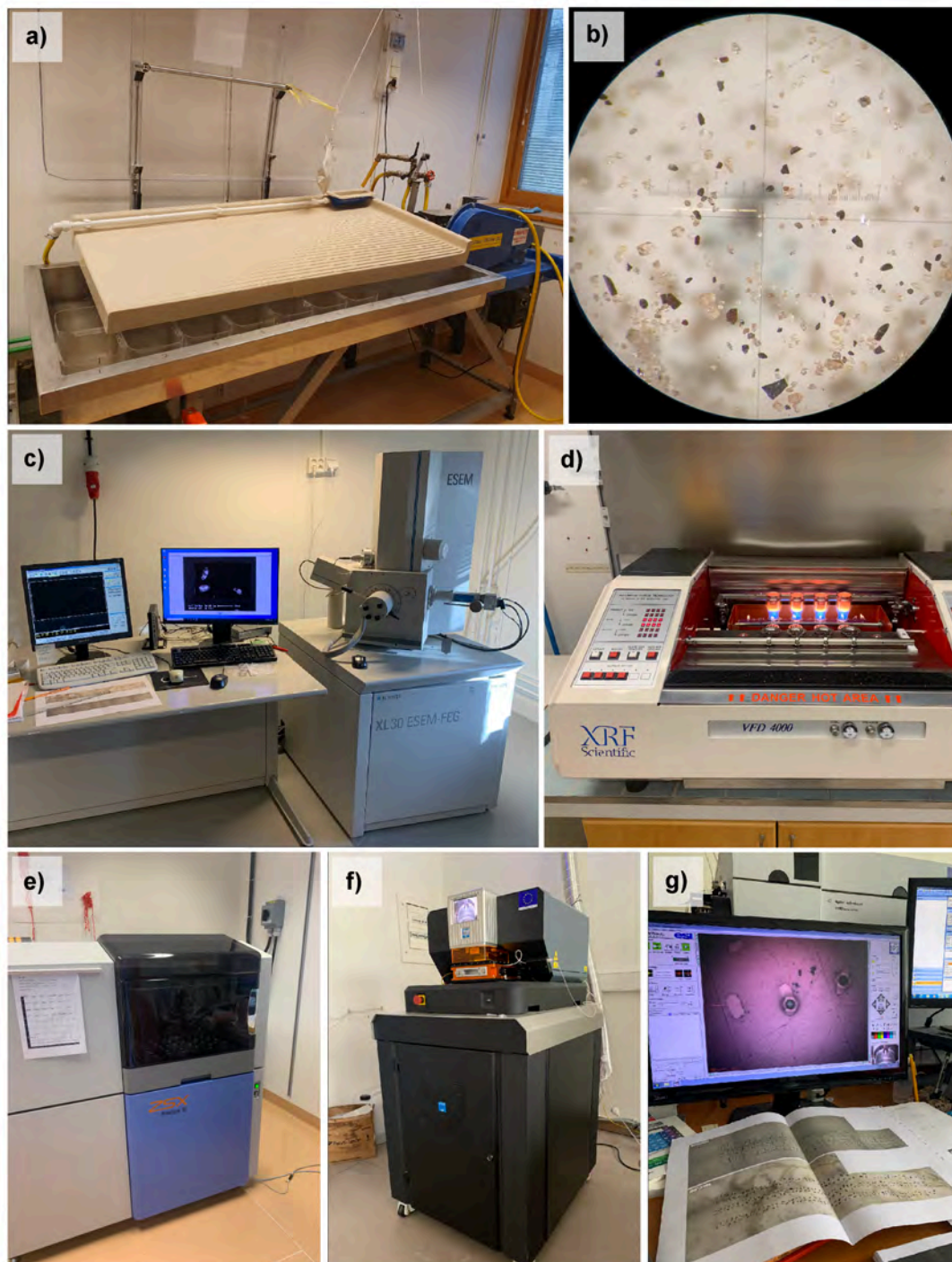


Figure 6: A compilation of the various instruments and methods used during the study. a) A Wilfley table. b) Hand-picking zircons in a binocular microscope. c) The SEM equipped with a CL detector used for CL imaging. d) The XRF fuser. e) The Rigaku XRF. f) The LA-ICP-MS in Geosciencés Rennes. g) The laser ablation computer program.

Samples GM213, GM214, CH2240, CH2241 and CH2249 were prepared for zircon extraction whereas samples GM213, GM214, CH2231, CH2232, CH2233, CH2240 and CH2249 were prepared for whole-rock geochemistry analysis. The samples were crushed in a Retsch BB200 stainless grinder and milled with a Retsch RS200 tungsten steel mortar at Stockholm University. When necessary, the samples were sawed or hammered down to a size appropriate for the grinder. The intensity (revolutions per minute, rpm) and duration of the milling varied from sample to sample depending on the rock type as well as the desired grain size for the respective analyses. For the samples intended for X-ray fluorescence (XRF) analysis, the desired grain size is a fine silty powder whereas for the samples later used for mineral separation, the desired grain size is a fine-grained sand. The rpm and time used for the milling procedure is reported in Appendix A Tables A1 and A2. To avoid cross-contamination, all used material was thoroughly cleaned between each crushing and milling. First, the grinder and mortar were vacuum-cleaned while brushing with a steel brush to remove loose particles. Secondly, they were cleaned using ethanol.

4.1 Whole-rock geochemistry

Loss on ignition (LOI) was conducted at Stockholm University using a Carbolite ELF 11/14b furnace. To ensure that correct weights were obtained, a scale which is precise to the fifth decimal place was used. To begin with, the ceramic crucible was weighed empty and its weight was recorded. Then, 10 g of sample was extracted and poured into the crucible. Finally, the weight of the sample and the crucible was recorded. The samples were put in the furnace overnight and collected the following morning. The oven heats 3 °C per minute and thus takes 6 hours to reach the desired 1000 °C. Then, the sample was set to be dehydrated at 1000°C for 2 hours before the oven turns off and starts to cool. The samples were collected before cooling below 40-50 °C. The morning after, the samples were weighed again when they were around 40-50 °C. It was then left in the room for an hour to cool down to room temperature and re-absorb the moisture in the air. After an hour, the sample was weighed again. The second weighing was used to calculate the amount of reticular water. The crucibles were cleaned using sonic ultrasound for 15 minutes. The calculation of the water content in the samples (LOI) was conducted using Microsoft Excel.

X-ray fluorescence (XRF) analysis is commonly used to determine the bulk rock chemistry of a sample giving the major, trace and/or REE concentration of the sample. The XRF instrument emits an X-ray beam which excites the inner shell of the elements. In turn, the elements emit energy as the outer electrons are released. The magnitude of the energy release is dependent on the atomic number of the element and can thus be used by the analyser to calculate which element was hit by the beam. Using this technique, accurate measurements of the bulk rock chemistry can be obtained. The XRF analysis was conducted using a Rigaku Primus II X-ray fluorescence (Fig. 6e) spectrometer and the fusion was conducted using a Phoenix Autofuser (Fig. 6d), all available in the Petrotectonics Analytical Facility at Stockholm University. The XRF instrument measures the major elements to a high precision. To prepare the fused glass disks, a 5:2 ratio of lithiumborate flux and rock powder was used (see Appendix A, Table A5), which lowers the melting temperature of the sample to about 1100 °C. The flux is a mixture of 67% lithiumtetraborate and 34% lithiummetaborate. The flux and sample was weighed and poured into a platinum crucible for the fusion process. For accurate measurements, a precision of 0.0002 is required for the XRF analysis. Prior to fusing, the flux and sample was mixed thoroughly to ensure that the melting temperature is homogeneous throughout the mixture. The fuser melts and swirls the sample for a set program which ensures homogeneous melting and mixing of the sample. Prior to pouring out the melt into the platinum mould, the mould was pre-heated to avoid cracking of the glass sample due to the temperature difference. The fused glass disks were removed carefully so that the surface to be used for XRF analysis was not contaminated.

The platinum crucible and the moulds were cleaned using an ultrasound bath with de-ionized water for about 15-30 minutes. The glass stuck onto the platinum was gently removed with a wooden tool to avoid scratching the crucible. Then, they were put in warm, around 110 °C, 10% HCl for 20-30 minutes to dissolve potential glass leftovers. The crucibles and moulds were then air-dried. Later, the XRF analysis was carried out overnight. The standards used for the XRF measurements were a basalt (BCR-2), an andesite (AGV-2) and a rhyolite (RGM-1) (Flanagan, 1969, 1976, 1967).

4.2 Mineral separation

To separate the zircons from the sediment, a Wilfley table was used (Fig. 6a). It is a water table which separates heavy grains from lighter grains using water flow. The table is connected to two different water taps, one in the top right corner of the table and a water hose oriented parallel to the table with holes at even distances from each other so that water is distributed across the table. To optimize the sorting, the table was also shaken in the horizontal direction. Finally, the table was slightly tilted to promote efficient sorting. The sample was poured onto the table from the top right corner of the table. In theory, the lighter grains will quickly run down the table and collect directly below the release point, whereas heavier grains will be transported along the table and collect at a distance from the release point. The sediment was collected in numbered buckets along the edges of the water table. When the whole sample has been poured onto the table, the sorting was continued until the sediment remaining on the water table was homogeneous. This material was collected in a glass jar at the end of the table and poured over to a petri dish. The first bucket (fraction 1) was also collected and poured onto a petri dish. The rest of the fractions (2-7) were put together in two appropriate groups. All of the sediment was dried at 50 °C overnight.

When the petri dishes containing the zircons and the first fractions were dry, magnetic material were removed using a magnet pen. Then, the samples were transferred to plastic-lined paper bags. The other fractions were transferred to plastic bags and put aside. Between each sample that was separated, the petri dishes were cleaned using soap and ethanol. All buckets used for the water table were washed with soap and water. The zircons were hand-picked in a binocular microscope and extra care was taken to not introduce bias in the zircon population (Sláma and Košler, 2012) (Fig. 6b). Thus, in the detrital zircon samples (GM213, GM214, CH2241), it is important to pick zircons that are variable in size, color and shape. The zircons were mounted on pucks and then sealed in epoxy. Finally, the mounts were polished at the Natural History Museum (NRM) to expose the equatorial section of zircon. The Wilfley table fractions as well as details on the polishing procedure are reported in Appendix A Table A3 and A4, respectively.

4.3 CL imaging

A scanning electron microscope (SEM) is used to obtain a high-resolution image of a sample by using a focused electron beam instead of light (Reed, 2005). The theory behind the SEM to obtain the chemistry of a point is the same as for XRF, but a beam of electrons is used instead of X-rays. Similarly, the beam of electrons excite the outer shell of electrons causing them to advance to an inner shell. Since it is unstable, it will quickly fall back to its shell and the energy released is specific to the element. Thus, the SEM records the energy and calculates to which element it belongs. Cathodoluminescence (CL) can be used to image the internal textures of zircon (Corfu et al., 2003). Normally, light is produced by irradiation of a material which releases photons in the visible light spectrum. CL is produced when an element is bombarded with electrons which causes emission of photons. In an SEM equipped with a CL detector, an electron beam is emitted onto the sample and the resulting photons produces an image of the sample. The colors on the image range from black to white and the darker colors reflect higher

U-Th content. The zircons were imaged at NRM using a XL30 ESEM-FEG equipped with a Centaurus detector (Fig. 6c). The accelerating voltage was 15 kV and the zircons were imaged at 200X or 250X magnification. The contrast and brightness was the same for all samples (41 and 49, respectively).

4.4 U-Pb dating of zircons

The analysis of zircon for U-Pb dating was conducted using laser ablation inductively coupled plasma mass spectrometry (LA-ICP-MS) (Fig. 6f-g). The following description of the technical aspect of an LA-ICP-MS is summarized from Košler and Sylvester (2003) as well as Košler (2007). The LA-ICP-MS system is made up of three main components, the Laser Ablation (LA) and the Inductively Coupled Plasma (ICP) and a Mass Spectrometer (MS) (Fig. 7). The laser ablation system produces a concentrated beam of photons, i.e. a laser (Light Amplification by Stimulated Emission of Radiation) which is used to irradiate the sample. It is connected to a laser beam delivery system which adjust the wavelength, the size of the beam and steers it onto the sample. The spot where the laser interacts with the sample is surrounded by the ablation cell. The ablation results in a series of particles released from the sample, which is carried to the ICP using various carrier gases, most commonly a controlled mixture of helium, argon and nitrogen. The inductively coupled plasma is essentially a hot gas, usually made of argon, which is ionized using circulation of free electrons which collide with the Ar atoms. Thus, the Ar plasma is heated and eventually reaches temperature up to 8000-10000 K. The plasma can ionize nearly any elements, but is more efficient for lithophile and siderophile elements compared to chalcophile. Finally, the sample is transferred to the mass spectrometer using a skimmer cone which allows the analysed material to enter the vacuum (mass spectrometer) from atmospheric pressure (plasma). The sample enters the detector which records the ions as individual counts. Mass fractionation is one of the most important errors of the LA-ICP-MS that needs to be corrected for. In particular, it is the difference of the ionization potential of different elements that introduces mass bias in the ICP-MS, which can lead to large errors (Košler, 2007).

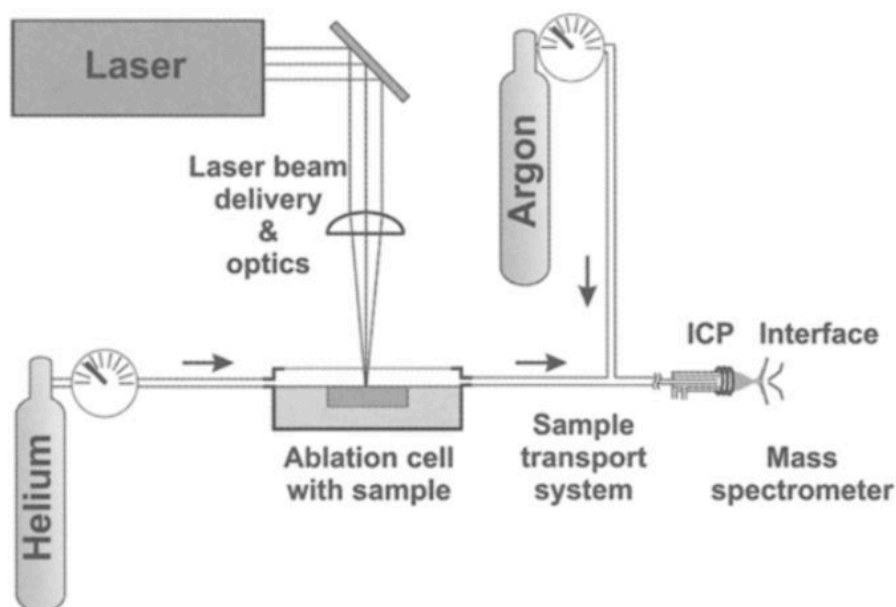


Figure 7: A schematic image of the constituents in the LA-ICP-MS system, including the laser delivery system, the carrier gas connections and the transportation to the spectrometer. Figure by Košler (2007).

The analysis was carried out at the GeOHeLiS platform at Géosciences Rennes, France with an

ESI NWR193UC Excimer laser coupled to an Agilent quadrupole 7700x ICP-MS. The diameter of the laser was 25 μ m and the repetition rate was 4Hz with a fluency of 6.65 J/cm². The complete set of working conditions for the instrument is reported in Appendix D Tables D1 and D2. The standard used for U-Pb dating was zircon GJ-1 (Jackson et al., 2004) whereas Plešovice was used as quality control (Sláma et al., 2008). The analysis of Plešovice resulted within the accepted range, meaning that the quality control was passed (Fig. D1). The standard for the trace element analysis was the glass NIST 612, and zircon 91500 (Wiedenbeck et al., 1995, 2004) was used for quality control. The session is set up in batches of 11 analyses. First, two standards are analysed which are used to correct for instrumental drift and mass fractionation during the session. Then, one quality control zircon is analysed. Finally, 8 'unknowns', i.e. zircon from the sample, is analysed. This session is repeated until a desirable amount of analyses have been reached. The software Iolite 4 (Paton et al., 2010) was used for the re-calculation and extraction of the ages and trace elements at Géosciences Rennes.

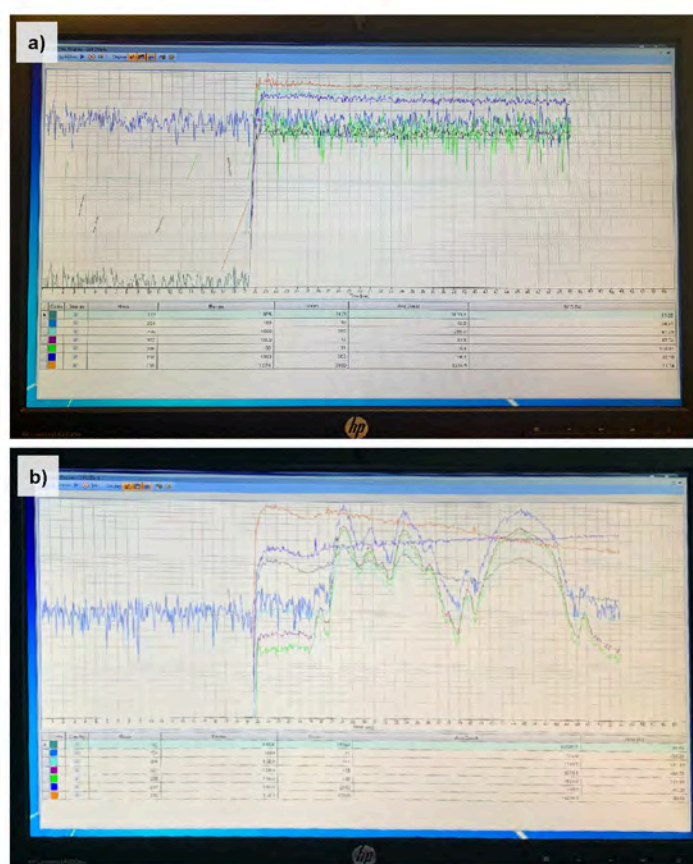


Figure 8: The spectrum obtained from the LA-ICP-MS can be very different depending on the quality of the analysis. (a) An analysis of a standard showing a constant and steady signal throughout the ablation. (b) An analysis with various spikes, most likely resulting from micro-inclusions in zircon which were too small to be observed or are situated below the surface.

The interference between mercury (²⁰⁴Hg) and lead (²⁰⁴Pb) was corrected for by analysing the background signal before introducing the sample, following the methodology described in Gilbert and Glorie (2020). Furthermore, no common Pb correction was applied since the uncertainties of the analysis in an LA-ICP-MS system generally is higher than the common Pb content of zircons. The concordance was calculated as: if $\text{Age}^{206\text{Pb}/238\text{U}} > 1000$: $\text{Age}^{206\text{Pb}/238\text{U}} / (\text{Age}^{207\text{Pb}/235\text{U}}) * 100$; else $\text{concordance}\% = \text{Age}^{207\text{Pb}/235\text{U}} / \text{Age}^{207\text{Pb}/206\text{Pb}} * 100$. The values were accepted as concordant between 90-105%. In the system, the

^{235}U is not measured directly, but calculated from the measured ^{238}U and the ratio $^{238}\text{U}/^{235}\text{U}$ which is considered constant at 137.8 in crustal rocks (Hiess et al., 2012). Hence, dates are given in $^{206}\text{Pb}/^{238}\text{U}$ to represent the actual measured values. Finally, the mean squared weighted deviation (MSWD) is reported in concordance + equivalence. If a date is concordant, the two U-Pb dates are equal within a 95% confidence interval. The equivalence vary with the spread of the scatter, where 1 equals no scatter of the dates whereas high and low numbers indicates high scatter. Hence, the age is more robust if concordance and equivalence is close to 1, which means that the dates agree and there is little spread of the ages. The nature of the spectrum will also determine if the analysis contain useful information or not. For example, a standard analysis of zircon will yield a spectrum as observed in Figure 8a whereas a zircon with abundant inclusions will yield a spectrum as observed in Figure 8b. The more stable signal will give a more robust estimation of the chemical content of the analysed zircon.

In order to calculate the age of the protolith (for the orthogneiss and felsic layer) and visualize zircon populations, the online version of IsoplotR (Vermeesch, 2018) was used. The visualization and statistical analyses of the detrital zircon data was also conducted using IsoplotR (Vermeesch, 2012). To visualize detrital zircon dates, a Kernel Density Estimation (KDE) was used which is a function (the Kernel function) that estimates a line from the data points by only visualizing the data a window at a time. The amplitude and bandwidth of the Kernel function will affect the roughness of the line. The treatment of the trace element data was conducted using Microsoft Excel (v.16.71) and the data was normalized to chondrite (McDonough and Sun, 1995).

5 Results

5.1 Sample description

The Germanasca valley exposes rocks belonging to the Pinerolo, Chasteiran, Muret, and Serre Units (Fig. 4a). The structurally lowest unit is the Pinerolo Unit. It is exposed in the east of the Germanasca valley and comprises Carboniferous graphitic-rich metaconglomerates and metasediments. The Chasteiran Unit is a discontinuous unit, located structurally above the Pinerolo Unit. The Muret Unit lies on top of the Pinerolo Unit. The main lithologies of the Muret Unit exposed in the Germanasca valley are garnet-bearing micaschists, paragneiss and orthogneiss. Orthogneisses are quite rare. They occur as a strongly deformed km-long slice at the contact with the Pinerolo Unit and as an undeformed km-scale orthogneiss body in the Punta Muret area. The strongly deformed body is the focus of this study whereas the undeformed body has been investigated in detail by Nosenzo et al. (2022).

The samples investigated in this study were collected in northwestern Italy, in the Germanasca valley (Fig. 9) during four field campaigns conducted between 2022 and 2023 by Paola Manzotti, Michel Ballèvre, Francesco Nosenzo and William Westin. In this study, petrographic observations were conducted on 32 samples. Five samples out of 32 were selected for geochemistry and geochronology (Table. 2). The samples selected for geochemistry and geochronology are three micaschists (GM213, GM214 and CH2241), an orthogneiss (CH2249) and a felsic layer (CH2240) (Fig. 10 and Table 2). Sample CH2249 is a medium-grained orthogneiss, light-grey in color, collected in the southern part of the Germanasca valley (Fig. 10 and 14). It constitutes the km-long strongly deformed body at the contact with the UHP Chasteiran Unit. It is strongly deformed and displays a top-to-the-W lineation. Samples CH2231, CH2232, CH2233 and CH2241 are garnet-bearing micaschists collected in the same outcrop close to the Cialancia bridge (Fig. 12). The main difference between these samples is the grain size, with samples CH2231, CH2232 and CH2241 being coarser-grained compared to sample CH2233. Sample CH2241 is a coarse-grained sample and it was specifically collected for geochronology. Sample CH2240 is a felsic layer which occurs in the coarse-grained micaschist (samples CH2231,

CH2232, CH2241). The orientation of the layer is parallel to the main foliation displayed by the micaschist. Samples GM213 and GM214 were collected in outcrops adjacent to each other close to the Rabbioso bridge, further west in the valley (Fig. 10 and 11).

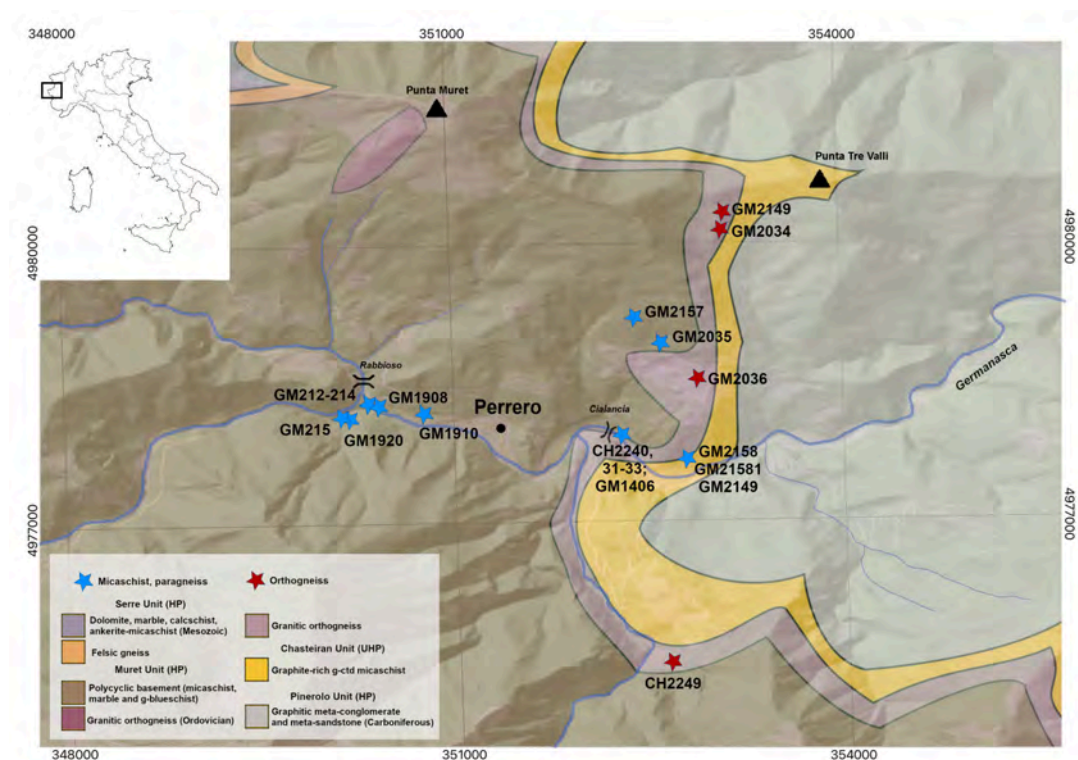


Figure 9: Map displaying the location of the investigated samples. The bridges Rabbioso and Cialancia are shown. The color of the star indicates the rock type (i.e. blue: micaschist and paragneiss; red: orthogneiss). To produce the map, the DEM TINITALY was used (Tarquini et al., 2007) and the coordinate system is ED50/UTM zone 32N.

Table 2: Summary of the samples selected for detailed investigation and their approximate location. Note that samples marked with * are all from the same outcrop. For exact location in the valley see Figure 10.

Sample	Rock type	Analyses			Location
		Petrography	Geochronology	XRF	
GM213	g-micaschist	X	X	X	Rabbioso bridge
GM214	g-ab-micaschist	X	(X)	X	"
CH2249	Orthogneiss	X	X	X	South Germanasca
CH2240	Felsic layer	X	X	X	Cialancia bridge
CH2241*	g-ab-micaschist		X		"
CH2231*	g-ab-micaschist	X		X	"
CH2232*	g-ab-micaschist	X		X	"
CH2233	g-ab-micaschist	X		X	"

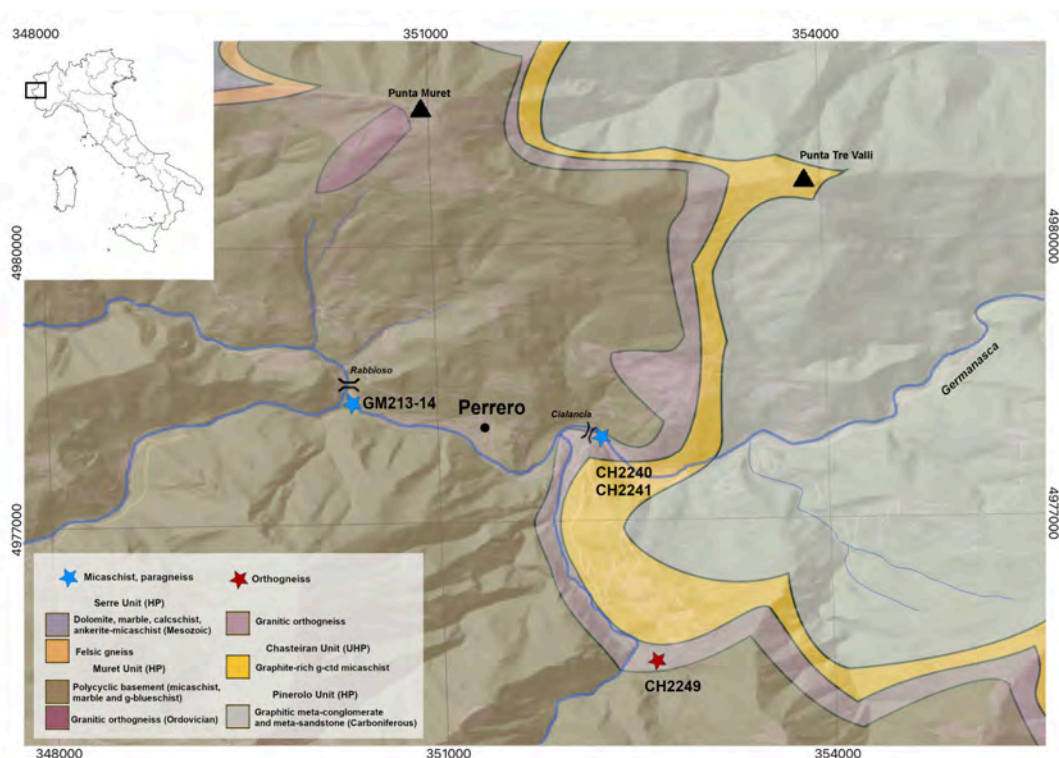


Figure 10: Map showing the location of the samples selected for detailed petrography and geochronology in the Germanasca valley. To produce the map, the DEM TINITALY was used (Tarquini et al., 2007) and the coordinate system is ED50/UTM zone 32N.

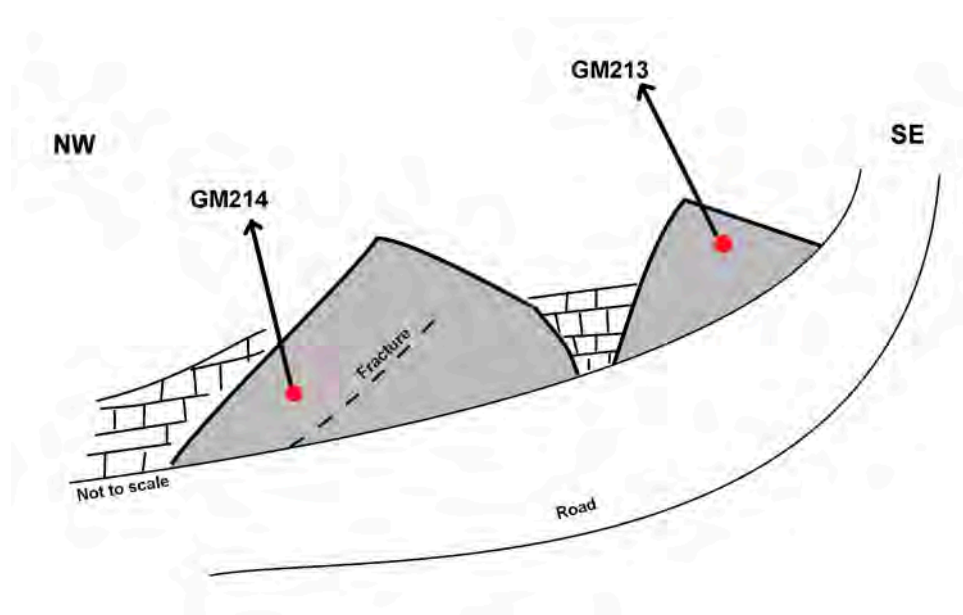


Figure 11: Sketch of the outcrops from which samples GM213 and GM214 were collected. Note that the image is not to scale. The right-hand outcrop is about 2 m high whereas the left-hand outcrop is about 5 m high.

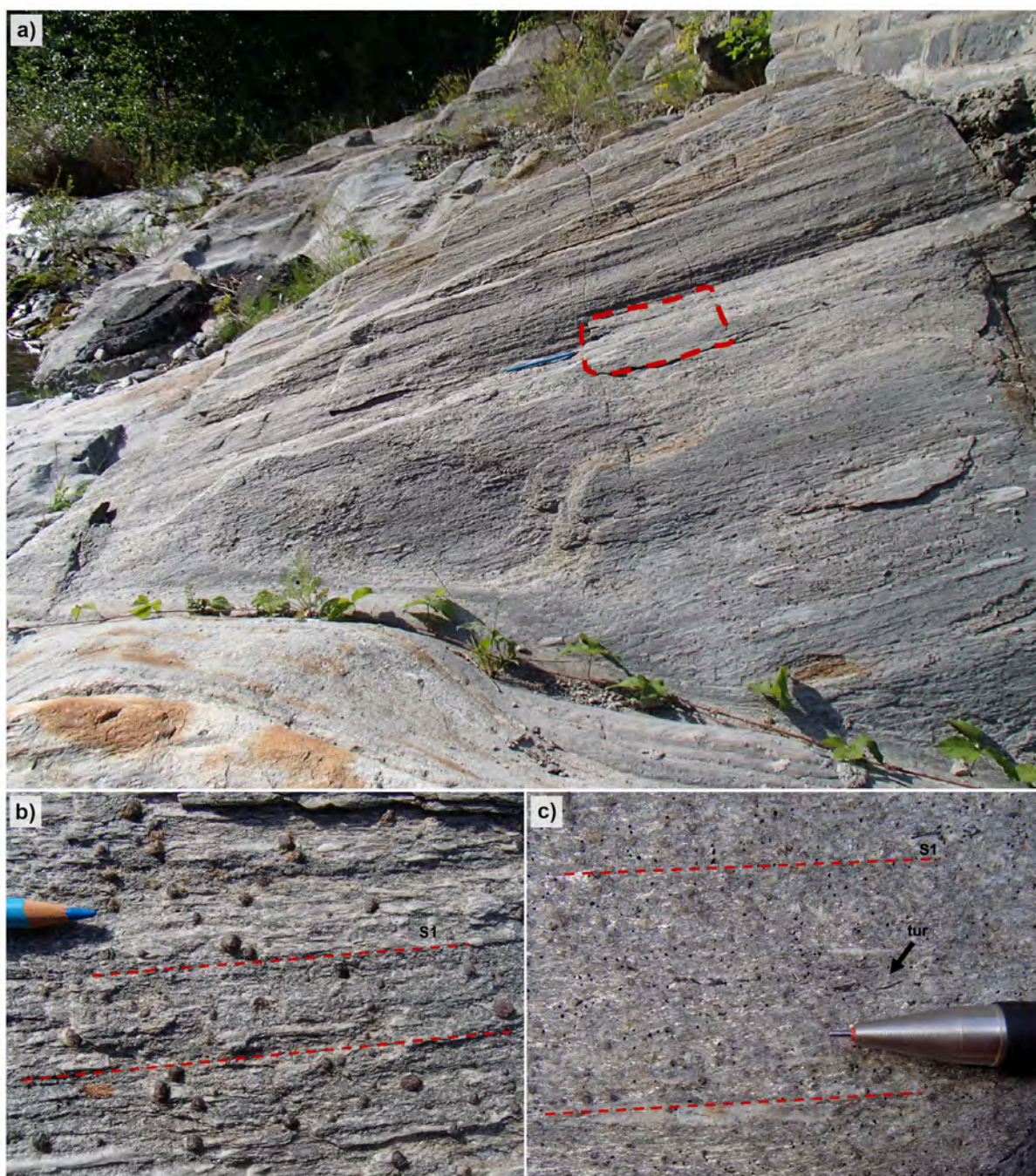


Figure 12: a) The outcrop from which samples CH2231, CH2232 and CH2233 were collected. The dashed red line indicates the exact location for the collected samples. Pen for scale. b) Samples CH2231 and CH2232 display a foliation and abundant, euhedral cm-sized garnet porphyroblasts. c) Sample CH2233 is fine-grained with mm-sized garnet porphyroblasts and elongated tourmaline (black arrow).



Figure 13: The felsic layer occurs within the g-micaschist (samples CH2231, CH2232 and CH2233 outcrop). It is oriented parallel to the main foliation.

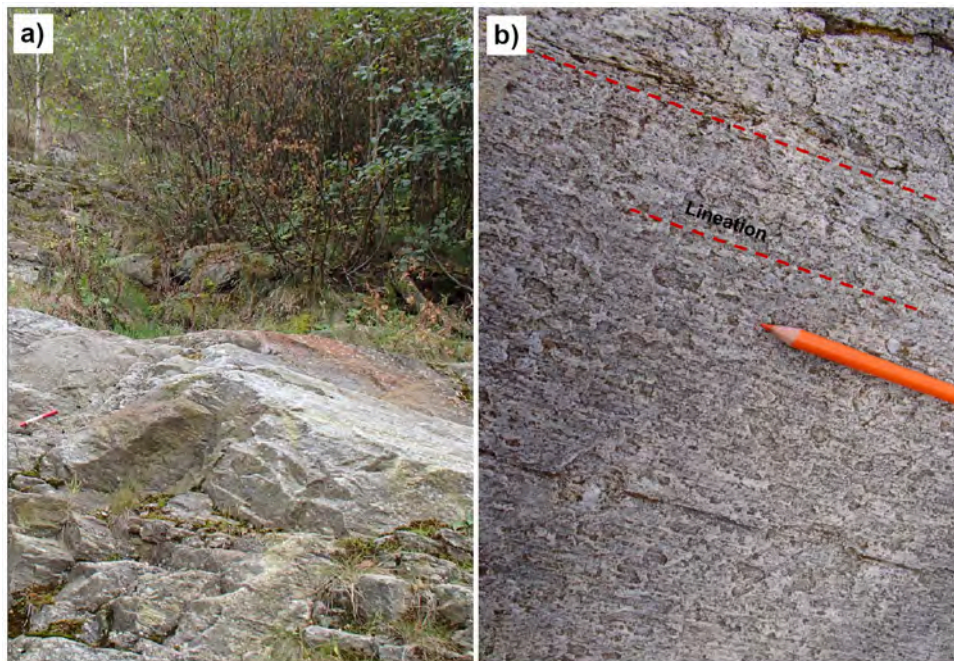


Figure 14: a) The orthogneiss CH2249 is light grey in color and crops out in the forest. b) On closer inspection, it displays a top-to-the-W lineation.

5.2 Petrography

The following descriptions involve the thin sections of the samples selected for geochronology. For the descriptions of the other samples, see appendix B (Fig. B1-B10).

5.2.1 GM213

Rock type: g-micaschist

Macroscopic aspect

The hand sample is grey, fine- to medium-grained. The sample displays a weak foliation defined by discontinuous quartz layers.

Deformation

At the micro-scale, a foliation is defined by the shape-preferred orientation of white mica and it is weakly folded (Fig. 15a).

Mineral composition

The main minerals are white mica (50%), quartz (20%), garnet (10%) and chlorite (10%) with accessory phases rutile (< 5%), ilmenite (< 5%), clino/zoisite (< 5%), plagioclase (< 5%), titanite (< 5%) and chloritoid (< 5%).

Timing of mineral growth with respect to deformation

The main foliation is defined by the shape-preferred orientation of white mica and chlorite and by discontinuous quartz layers. Garnet porphyroblasts, up to 500 μm , are idioblastic and wrapped by the main foliation. They display inclusions of rutile, chloritoid, white mica, clino/zoisite, quartz, ilmenite and quartz (Fig. 15b). Chloritoid mainly occurs in the core, whereas rutile is present both in the core and in the rim. Quartz is mainly observed in the rim. Inclusions mark an internal fabric (i.e. a foliation) which is different in the core and rim. In the core they are oriented at an angle to the main foliation and in the rim they are concentric. Garnet crystals are locally fractured and partially replaced by chlorite along the fractures. White mica is locally included in quartz. Lozenge-shaped pseudomorphs (interpreted to be after glaucophane) are elongated at an angle to the main foliation and consist of a fine-grained aggregate of albite and chlorite (Fig. 15a). Titanite is dispersed in the matrix, mainly oriented parallel to the main foliation and it is frequently found close to garnet.

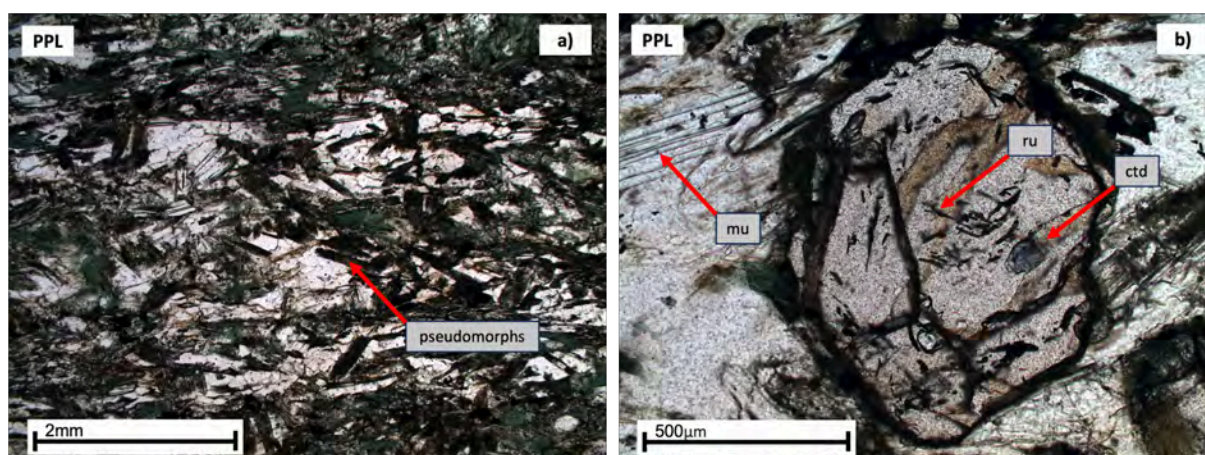


Figure 15: a) The main foliation is defined by the orientation of white mica. Pseudomorphs of glaucophane are dispersed in the matrix. b) Garnet with rutile and chloritoid inclusions with a different orientation in the core compared to the rim. Note that the thin section is thick, up to 40 μm .

5.2.2 GM214

Rock type: g-micaschist

Macroscopic aspect

The hand sample is light to dark grey, medium-grained and shows foliation. The foliation is defined by whitish bands.

Deformation

At the micro-scale, a main foliation is defined by various layers which are either rich in mica or in plagioclase. This foliation is microfolded.

Mineral composition

The main minerals are white mica (30%), quartz (25%), plagioclase (20%), chlorite (10%) and garnet (5%) with accessory phases epidote (< 5%), rutile (< 5%), clino/zoisite (< 5%) and opaques (< 5%).

Timing of mineral growth with respect to deformation

The main foliation is defined by alternating layers of white mica and plagioclase. Garnet porphyroblasts are up to 500 μm , idioblastic and wrapped by the main foliation. The larger porphyroblasts show an optical discontinuity between core and rim, that separates a pink core from a paler rim (Fig. 16). They display inclusions of quartz, white mica, opaques, epidote and rutile which do not vary in abundance throughout the crystal. In the core, the inclusions do not mark an internal fabric but in the rim they are often parallel to the main foliation.

Plagioclase is abundant in the matrix and defines the foliation together with white mica. It contains inclusions of white mica, chlorite and quartz which are oriented parallel to the main foliation. Epidote and clino/zoisite occur as rounded or elongated crystals in the matrix. Lozenge-shaped pseudomorphs (interpreted to be after glaucophane) consist of a fine-grained aggregate of chlorite, albite and quartz. These occur dispersed in the matrix and sometimes display a corona of albite.

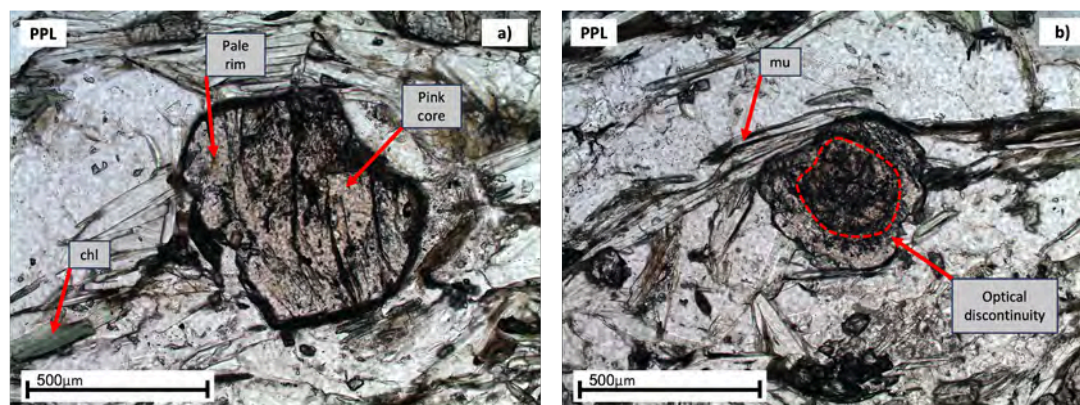


Figure 16: a) Garnet showing two generations of growth, with a more pinkish core and a paler rim. b) These are separated by a clear optical discontinuity.

5.2.3 CH2231A-B

Rock type: g-ab-micaschist (coarse grained)

Macroscopic aspect

The hand samples are grey to dark grey and coarse-grained. Both hand samples display a well-developed foliation which is slightly wavy. Garnet porphyroblasts (1-2 mm in size) are well-observable at the hand sample scale.

Deformation

At the micro-scale, the main foliation is defined by shape-preferred orientation of white mica and chlorite. Veins of quartz and plagioclase are oriented parallel to the foliation (Fig. 17a). The foliation is slightly folded.

Mineral composition

The main minerals are quartz (20%), white mica (20%), plagioclase (20%), chlorite (15%), garnet (10%) and titanite (5%) with accessory phases biotite (< 5%), epidote (< 5%), carbonate (< 5%), tourmaline (< 5%) and rutile (< 5%).

Timing of mineral growth with respect to deformation

The main foliation is defined by the shape-preferred orientation of white mica and chlorite as well as the alternation of quartz and plagioclase-rich layers (up to 1 mm each). There are abundant garnet porphyroblasts, 1-2 mm in size, which are wrapped by the main foliation. However, there are two different type of garnets, one which is more pristine and one which is more skeletal. Both types of garnet contain inclusions of quartz, epidote, white mica, titanite and rutile. The skeletal garnet contains more abundant quartz inclusions than the pristine variant. The inclusions do not mark an internal fabric. Epidote and rutile are concentrated in the core whereas titanite and white mica occur in the rim. Garnet crystals are locally fractured and partially replaced by chlorite and biotite along fractures. The strain shadows mainly consist of white mica, biotite and quartz.

Plagioclase, up to 1 mm in size, are abundant in the matrix and are wrapped by the main foliation. Plagioclase contains inclusions of titanite, white mica, quartz and epidote which mark an internal fabric parallel to the main foliation. Quartz is a major component in the matrix but also occurs as veins which occasionally cross-cut the foliation. Biotite is dispersed in the matrix as elongated sheets which are chloritized to varying degrees. In addition, rutile occurs in the matrix with a corona of titanite (Fig. 17b).

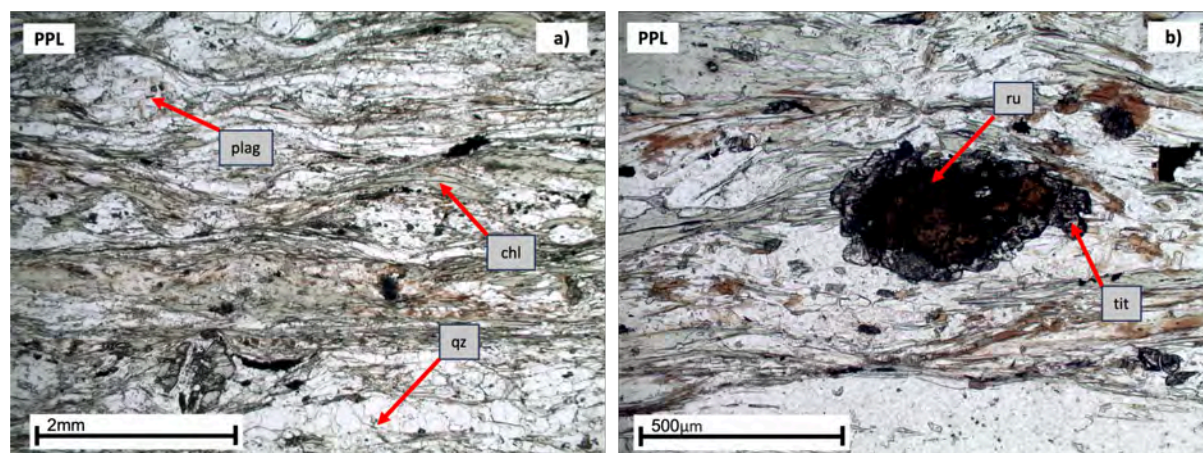


Figure 17: a) Main foliation wrapping plagioclase. b) Rutile with a corona of titanite.

5.2.4 CH2232A-B

Rock type: g-ab-micaschist (coarse-grained)

Macroscopic aspect

The hand samples are light to dark grey and coarse-grained. The samples display a foliation. Garnet porphyroblasts, 3-4 mm in size, are well observable at the hand sample scale.

Deformation

At the micro-scale, a main foliation is defined by shape-preferred orientation of white mica and deformed plagioclase. The foliation is strongly folded (Fig. 18a).

Mineral composition

The main minerals are quartz (30%), white mica (30%), plagioclase (15%), garnet (10%), titanite (5%) and chlorite (5%) with accessory phases rutile (< 5%), epidote (< 5%), biotite (< 5%) and opaques (< 5%).

Timing of mineral growth with respect to deformation

The main foliation is defined by the shape-preferred orientation of white mica and deformed plagioclase. There are garnet porphyroblasts, 3-4 mm in size, which are idioblastic and wrapped by the main foliation. Garnet contains inclusions of quartz, white mica, epidote, opaques and rutile. Rutile inclusions are preserved in the core whereas they are replaced by titanite at the rim. The inclusions generally do not mark an internal fabric, but quartz is sometimes slightly elongated at an angle to the main foliation (Fig. 18b). In sample CH2232A, an atoll garnet is observed, whose central portion is partially filled by opaques, titanite, white mica, chlorite and quartz. Garnet is locally fractured and is replaced by chlorite, quartz and biotite along the fractures.

In the matrix, there is abundant titanite which occurs as coronas surrounding rutile. There are remnants of biotite in the matrix, which is more or less chloritized. Plagioclase, up to 0.5 mm, is strongly deformed and contain abundant inclusions of titanite, quartz and white mica which are parallel to the main foliation.

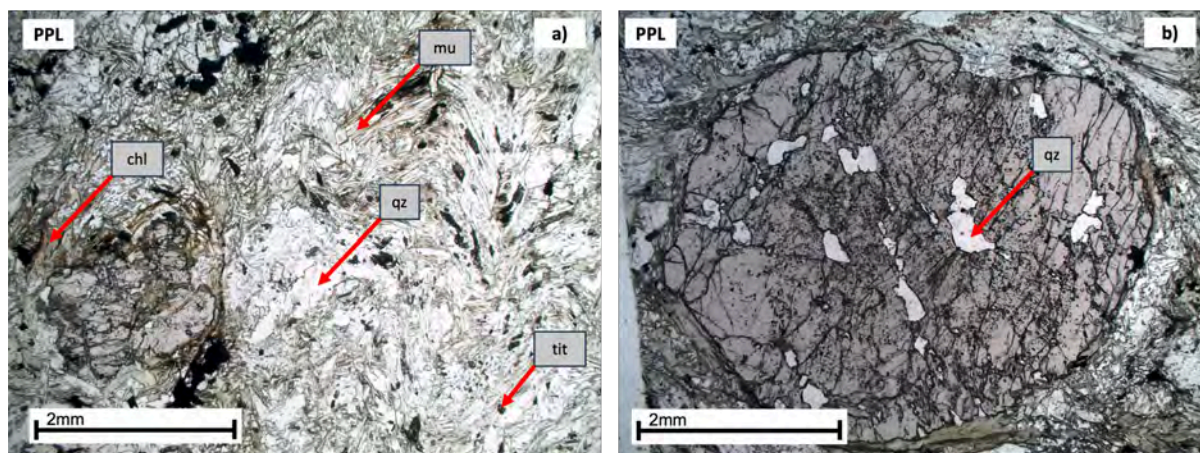


Figure 18: a) Main foliation is wrapped around the garnet porphyroblasts. b) Garnet contains abundant quartz inclusions which seem to show some elongation in the core of the garnet.

5.2.5 CH2233A-B

Rock type: g-ab-micaschist (fine-grained)

Macroscopic aspect

The hand samples are grey and foliated. Both samples are fine-grained and contains garnet porphyroblasts (< 1 mm in size).

Deformation

At the micro-scale, a main foliation is defined by the shape-preferred orientation of white mica and chlorite. The foliation is slightly wavy and wraps the garnet porphyroblasts (Fig. 19a).

Mineral composition

The main minerals are quartz (20%) white mica (30%), plagioclase (20%), chlorite (15%), garnet (5%) and titanite (5%) with accessory phases rutile (< 5%), biotite (< 5%), opaque (< 5%), and tourmaline (< 5%).

Timing of mineral growth with respect to deformation

The main foliation is defined by the shape-preferred orientation of white mica and chlorite. Garnet porphyroblasts are small (up to 500 μ m), eu- to subhedral and wrapped by the foliation. They contain inclusions of quartz, titanite and white mica where titanite tends to occur in the rim. The inclusions are slightly more concentrated in the core compared to the rim but they do not define an internal fabric. The strain shadow mainly consist of chlorite and biotite. Garnet is locally fractured and replaced by chlorite and biotite along the fractures. (Fig. 19b).

Zoned tourmaline is locally observed in the matrix which is parallel to the main foliation. The tourmaline has a blue core and a green to brown rim and has inclusions of titanite, white mica and opaques. Rutile occurs in the matrix and has corona of titanite. In addition, idioblastic titanite is dispersed in the matrix. There are strongly deformed plagioclase crystals which are wrapped by the foliation, and they contain inclusions of white mica, titanite and quartz.

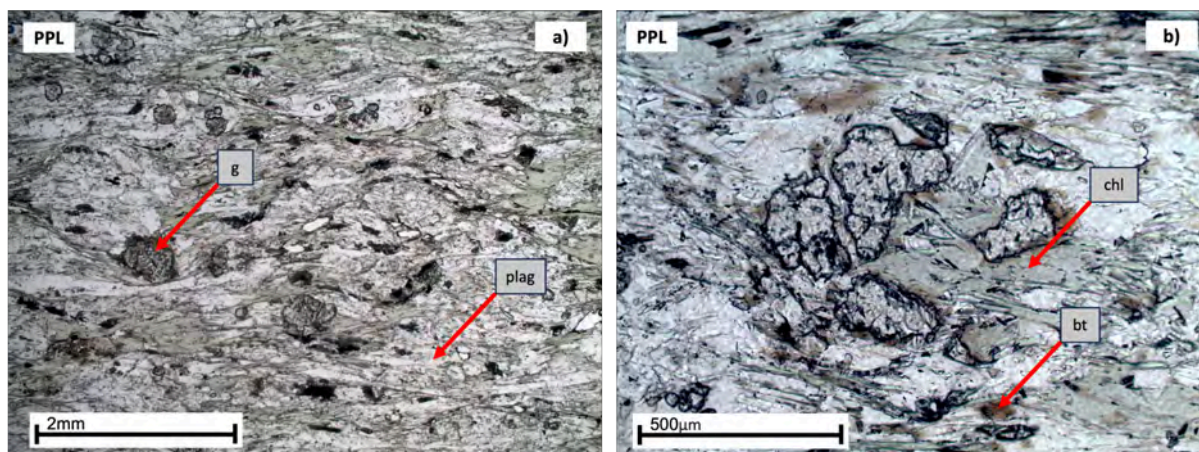


Figure 19: a) Main foliation wraps around the garnet porphyroblasts. b) Garnet is partially replaced by chlorite and biotite.

5.2.6 CH2240(1-2)

Rock type: Felsic layer

Macroscopic aspect

The sample consists of a quartz- and feldspar-rich gneiss occurring as a decimeter-thick layer sandwiched between garnet micaschists. The layer is hypothesized to be an original felsic dyke. Sample CH2240-1 was collected in the middle portion of the layer whereas CH2240-2 was collected close to the contact with the surrounding g-micaschist (samples CH2231, CH2232 and CH2233). The hand samples are white to light grey and medium-grained. They display a foliation which is defined by shape-preferred orientation of mica.

Deformation

At the micro-scale, a weak main foliation is defined by the shape-preferred orientation of white mica (Fig. 20a). The foliation is slightly folded and bends around the feldspar porphyroclasts. Sample CH2240-2 shows a more intense deformation than sample CH2240-1.

Mineral composition

The main minerals are quartz (40%), feldspar (30%), white mica (15%) and chlorite (5%) with accessory phases biotite (< 5%), epidote (< 5%), apatite (< 5%), opaques (< 5%) and titanite (< 5%).

Timing of mineral growth with respect to deformation

The weak main foliation is defined by the shape-preferred orientation of white mica. There are millimeter sized feldspar porphyroclasts, up to 1 mm in size. Plagioclase is sometimes zoned, with a distinct boundary between core and rim (observed as variation in the extinction angle in XPL), although sometimes shows no zoning or twinning. It contains inclusions of white mica and epidote. The inclusions generally do not mark an internal fabric but sometimes are parallel or at a low angle to the main foliation. The feldspars show evidence of sericitization.

Quartz is heavily deformed and displays undulose extinction. Epidote and titanite are dispersed in the matrix and occur as anhedral crystals. Most commonly epidote occurs in association with chlorite and titanite tend to occur in association with white mica. In addition, there is apatite dispersed in the matrix. Approaching the contact to the micaschist, the white mica content drastically increases while the amount of plagioclase and quartz decreases (Fig. 20b). Also, the intensity of the folding greatly increases.

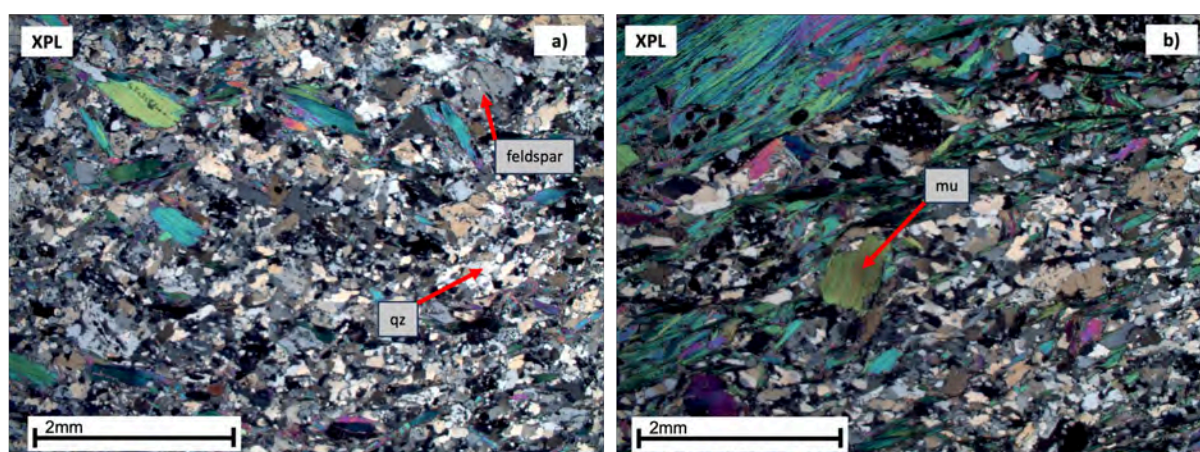


Figure 20: a) Main foliation defined by the shape-preferred orientation of white mica. b) The white mica content increases when approaching the contact to the micaschist.

5.2.7 CH2249(1-2)

Rock type: Augengneiss

Macroscopic aspect

The hand samples are fine-grained and light grey. They display a foliation which is defined by the fine-grained matrix. Feldspar porphyroclasts, up to 1.3 cm, are well observable in hand sample.

Deformation

At the micro-scale, a main foliation is defined by quartz-rich layers which are interlayered with white mica (Fig. 21a). The foliation is wrapped around the feldspar porphyroclasts. The foliation is more pervasive in sample CH2249-1 compared to CH2249-2 where the foliation is more deformed.

Mineral composition

The main minerals are quartz (50%), albite (20%), microcline (15%) and white mica (10%) which accessory phases chlorite (< 5%), opaques (< 5%), calcite (< 5%) and biotite (< 5%).

Timing of mineral growth with respect to deformation

The main foliation is defined by alternating layers of quartz, albite and white mica (up to 0.5 mm thick each). There are millimeter sized, up to 1 mm, subhedral feldspar porphyroclasts in the matrix which are wrapped by the foliation. These consist of albite and microcline, where the albite shows perthitic texture. The feldspar is heavily sericitized (Fig. 21b) and albite is partially replaced by microcline along the edges of the crystal. Additionally, larger feldspar porphyroclasts are present, up to 4 mm in size, which consist of plagioclase. They are wrapped by the main foliation.

White mica is abundant in the matrix and occurs both as idioblastic and anhedral crystals. The idioblastic crystals are parallel to the main foliation. In sample CH2249-1, there are no larger porphyroclasts but only small plagioclase clasts dispersed in the matrix. The plagioclase contain abundant inclusions of quartz which do not mark an internal fabric. In both samples, the white mica is partly recrystallised at the edges to a fine-grained aggregate. Biotite occurs dispersed in the matrix but is almost fully chloritized.

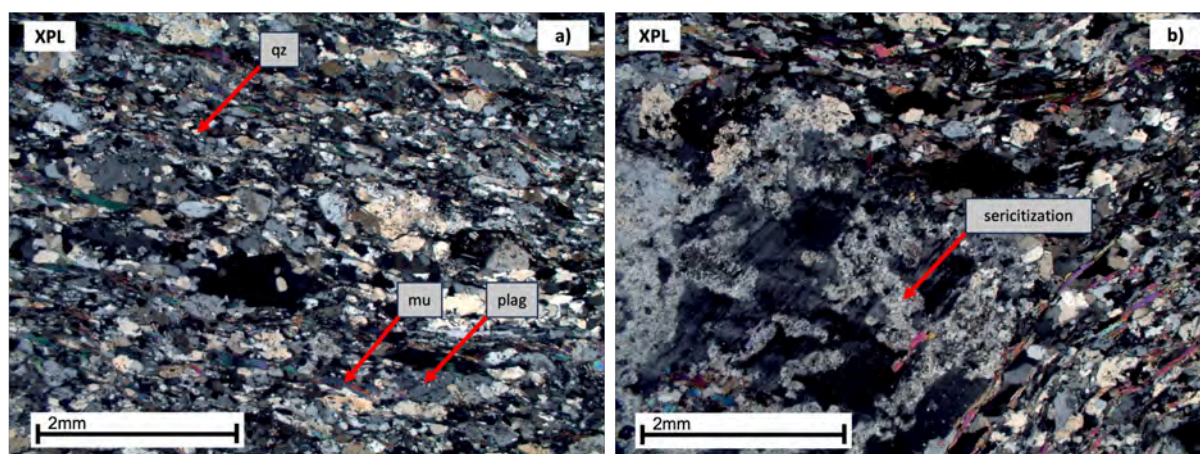


Figure 21: a) Main foliation is defined by the shape-preferred orientation of white mica. b) Feldspars display evidence of sericitization.

5.3 Whole-rock geochemistry

The whole-rock geochemistry of sample CH2249 (orthogneiss) and sample CH2240 (felsic layer) indicates that they are granitic/rhyolitic in composition (Fig. 22). Sample CH2240 plots on the edge of the diagram whereas sample CH2249 plots in the granitic field. By comparison, two orthogneisses from the undeformed domain in the Muret Unit (OG27, (Nosenzo et al., 2022) and PAG, (Bussy and Cadoppi, 1996)) are plotted (see Fig. 9). Samples OG27 and PAG are richer in FeO, CaO and MgO compared to samples CH2249 and CH2240. On the other hand, samples CH2249 and CH2240 are richer in SiO₂. Both the Muret orthogneiss and the mylonitic orthogneiss CH2249 as well as the felsic layer CH2240 are peraluminous in composition, meaning that $Al > Ca + Na + K$ (Fig. 23). Additionally, all four samples are calc-alkaline (Fig. 24), although CH2249 and CH2240 are richer in Na₂O and K₂O whereas OG27 and PAG are richer in FeO and MgO. Nonetheless, it should be noted that the bulk-rock chemistry may have been altered during metamorphism.

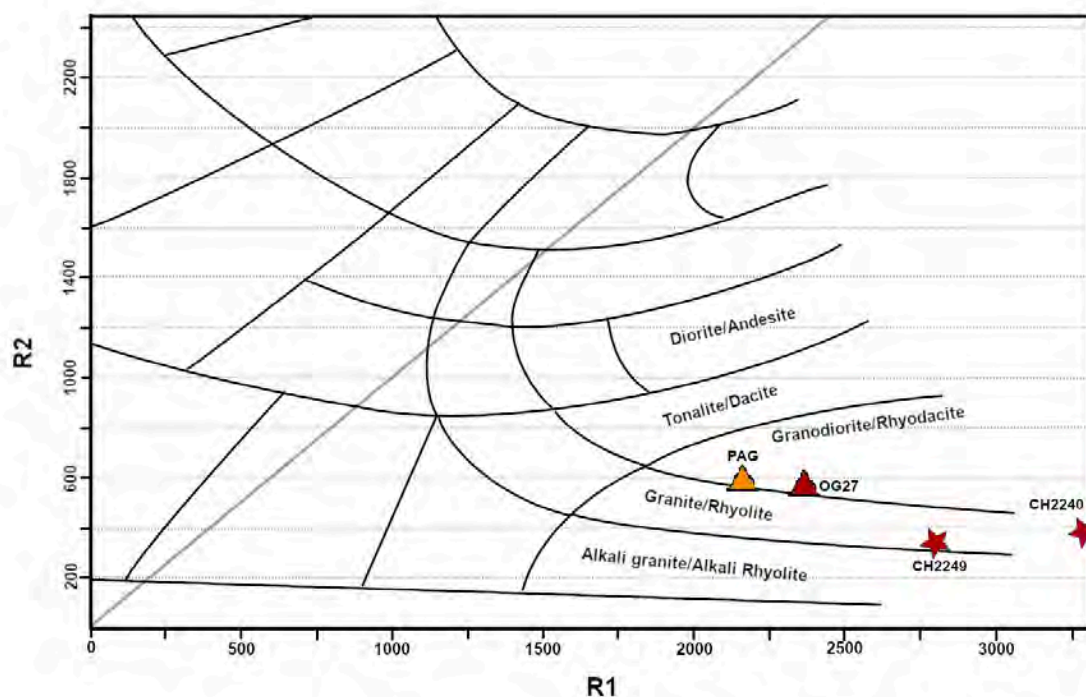


Figure 22: An R1-R2 plutonic chemical variation diagram (De La Roche et al., 1980) for the orthogneiss samples. The whole-rock chemistry indicates that samples CH2249 and CH2240 have a granitic/rhyolitic composition. By comparison, the Muret orthogneiss (OG27: Nosenzo et al. (2022) and PAG: Bussy and Cadoppi (1996)) has a granodioritic composition. $R1=4Si-11(Na+K)-2(Fe+Ti)$ and $R2=6Ca+2Mg+Al$.

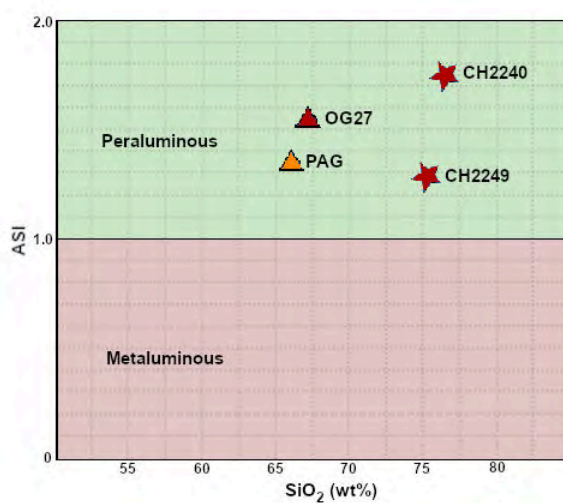


Figure 23: A plot of the aluminum saturation index and SiO_2 , as proposed by Frost and Frost (2008). $\text{ASI} = \text{Al}/((\text{Ca} - 3.33 * \text{P}) + \text{Na} + \text{K})$. The chemical classification indicates that the orthogneiss (CH2249) and the felsic layer (CH2240) are peraluminous. Similarly, the Muret orthogneiss (OG27 (Nosenzo et al., 2022) and PAG (Muret) (Bussy and Cadoppi, 1996)) are peraluminous.

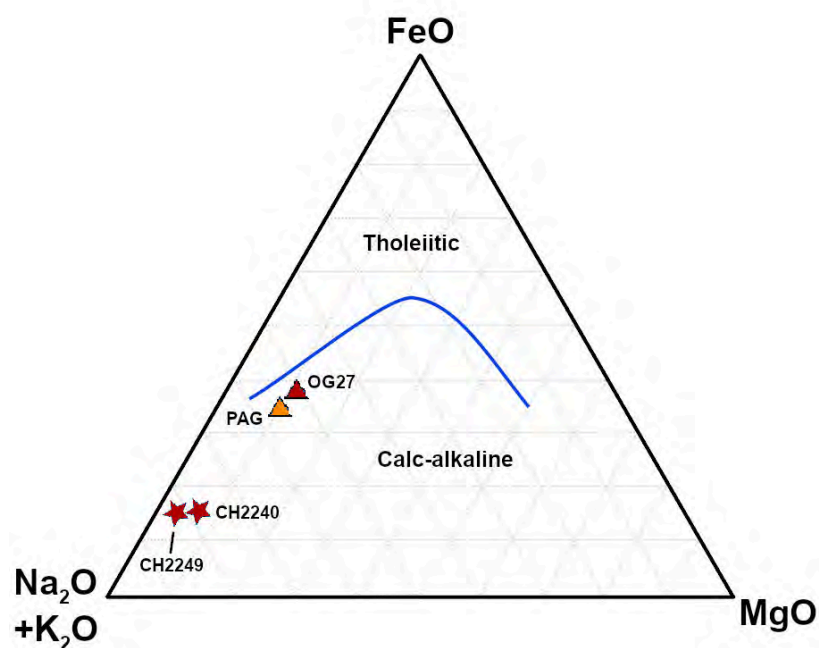


Figure 24: A total FeO ternary diagram indicating whether the igneous rock is tholeiitic or calc-alkaline (Irvine and Baragar, 1971). Samples CH2249 and CH2240 as well as the Muret orthogneiss (OG27: Nosenzo et al., 2022 and PAG: Bussy and Cadoppi, 1996) are calc-alkaline.

In an AFM diagram, the micaschists plot in or in close relation to the chlorite field (Fig. 25). For comparison, the micaschist samples from the Muret unit studied by Nosenzo et al. (2022) (GM1 and GM13) are plotted as well as the micaschist sample from the Chasteiran Unit (CH11) (Manzotti et al., 2022) and one sample (GM1914) from the Pinerolo Unit (Larsson, 2022). Of all samples, CH2233 has the highest alumina content whereas GM13 and GM214 has the lowest. Sample CH2233 also has a higher alumina content compared to CH2231 and CH2232. Samples GM213 and GM214 are richer in MgO compared to GM1 and GM13. The sample from the Chasteiran Unit (CH11), are chemically similar to GM1 and GM13. GM1, GM13 and CH11 are richer in FeO than the other samples. Sample GM1914 has much less alumina compared to the other samples.

The results from the loss on ignition (LOI) showed that the micaschists generally have higher water content than the orthogneiss and felsic layer (Fig. 26). Sample GM213 has the highest LOI at 3.28% whereas the orthogneiss (CH2249) have the lowest LOI of 0.82%. Between samples CH2231, CH2232 and CH2233, the LOI successively increases from 2.29% to 2.14%. Generally, the samples from the east of the valley, closer to the contact to the orthogneiss, has a lower LOI than the samples further to the west. The felsic layer has a water content of 1.25%. A table of the raw data from the LOI is given in Appendix C Table C1.

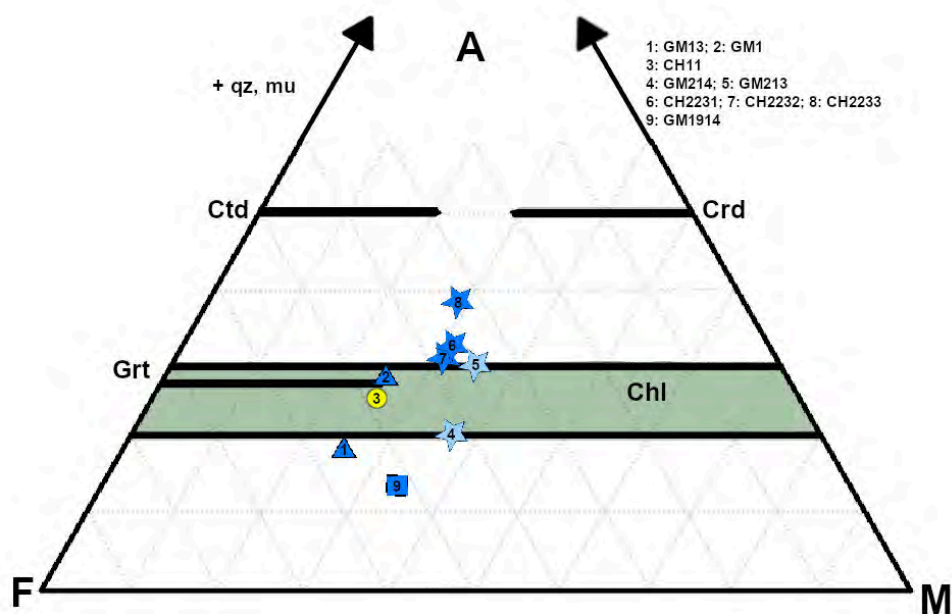


Figure 25: Samples CH2231, CH2232, CH2233, GM213 and GM214 plot in the chlorite field. The Muret micaschists have a slightly more iron-rich composition. The Chasteiran micaschist is more similar to the Muret micaschists. Data for GM1 and GM13 are from Nosenzo et al. (2022). Data for CH11 is from Manzotti et al. (2022). Data for GM1914 is from Larsson (2022). A = $\text{Al}_2\text{O}_3 - 3\text{K}_2\text{O}$, F = FeO, M = MgO. Quartz and muscovite are considered in excess.

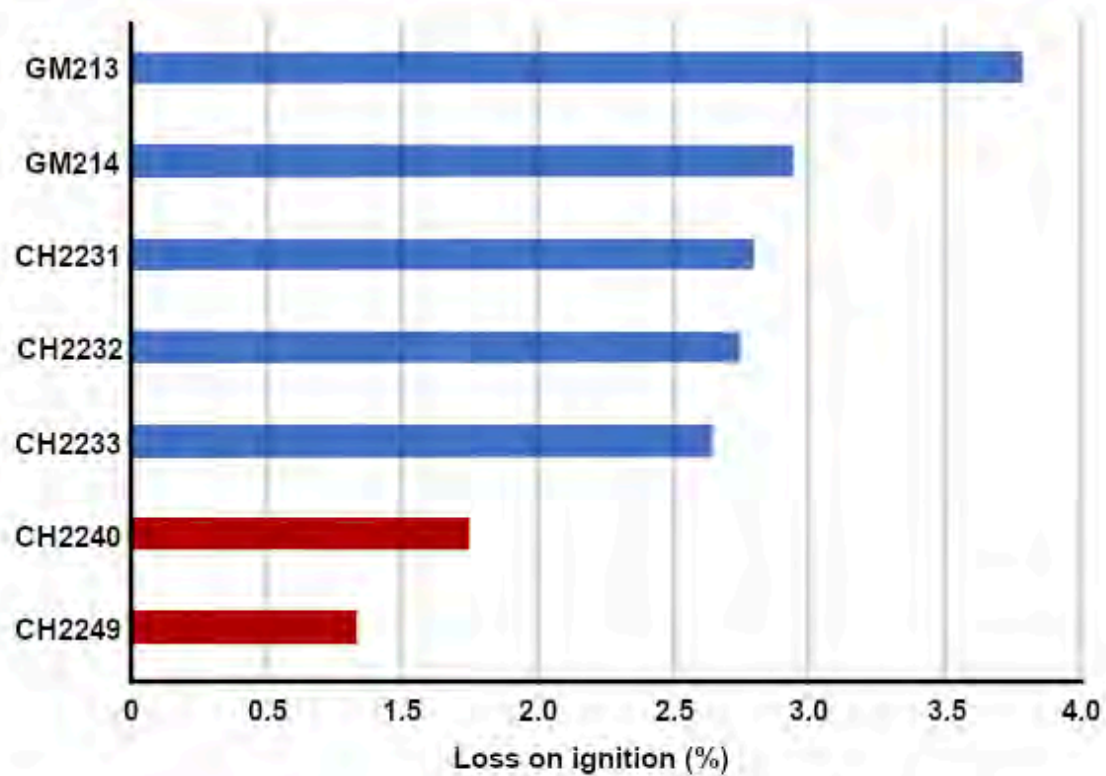


Figure 26: The results of the loss on ignition show that there is a difference between GM213 and GM214 whereas micaschists CH2231-33 are similar. The felsic layer yielded higher numbers than the orthogneiss.

5.4 Zircon textures and geochronology

5.4.1 GM213

Zircons are euhedral to sub-rounded with a grayish-pinkish color. They are generally small, up to 100 μm long. CL imaging shows that most zircons display a grey luminescent rim, up to 10 μm thick. The interface between core and rim is marked by a dark luminescent border. Zircons display various textures, including oscillatory and sector zoning along with fractures filled with a grey luminescent material. Additionally, many zircons are homogeneous. Overall, the majority of zircon shows oscillatory zoning or are homogeneous in texture. A representative selection of analysed zircons are given in Figure 27a, including the oldest and youngest obtained age. The Th/U ratio of the analysed zircons is highly variable, from 0.0-1.0, with the largest cluster around 0.0-0.4. (Fig. 27b). In total, 132 zircons were analysed of which 124 are concordant. Rims were not analysed because they are too small. The dates obtained from the detrital zircons range from 511 to 2836 Ma (Fig. 27c & d). The main population clusters around 600-750 Ma, whereas smaller populations are comprised between 650-1000 Ma. A few dates are comprised between 1550-3000 Ma.

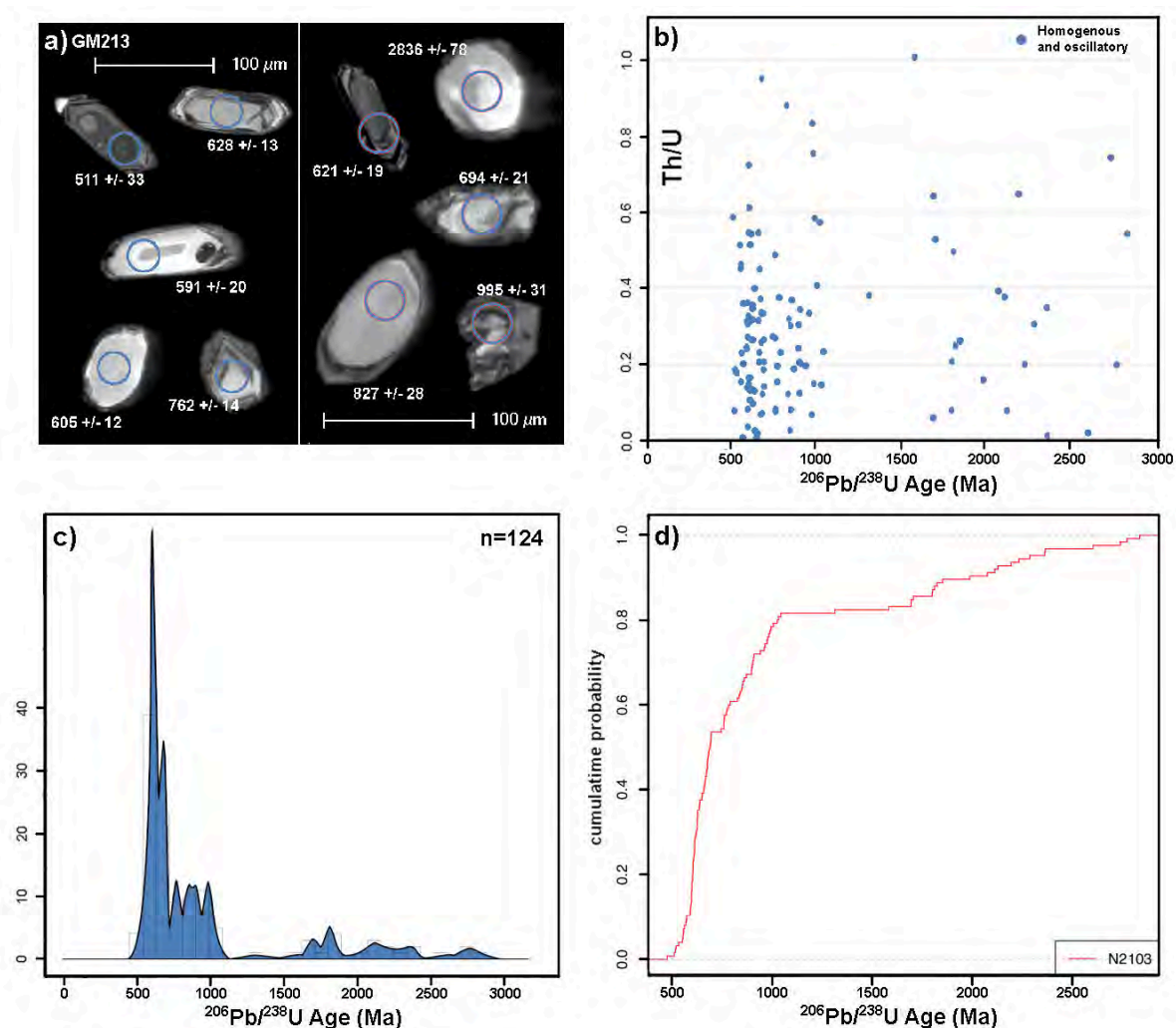


Figure 27: a) A representative selection of zircons used for dating. The blue circles indicate the ablation spot. The age of the analysed zircon is indicated adjacent to it. b) Th/U plot for sample GM213. c) A Kernel Density plot showing the distribution of dates. d) Cumulative probability plot for GM213.

5.4.2 GM214

Zircons are prismatic to sub-rounded and vary from gray-pinkish to colorless. They display a large size variation, with the largest crystals up to 120 μm long. Most zircons show complex internal textures with fractures healed with a grey luminescent material. Additionally, they exhibit oscillatory zoning which can be either narrow or broad. Many zircons have inherited cores which has been partially resorbed at the edges. Most zircons have a thin rim (up to 10 μm). A representative selection of zircons are given in Figure 28. In this sample, there were not enough zircon to achieve statistical significance of detrital ages. Therefore, it was decided to not conduct U-Pb dating on the sample.

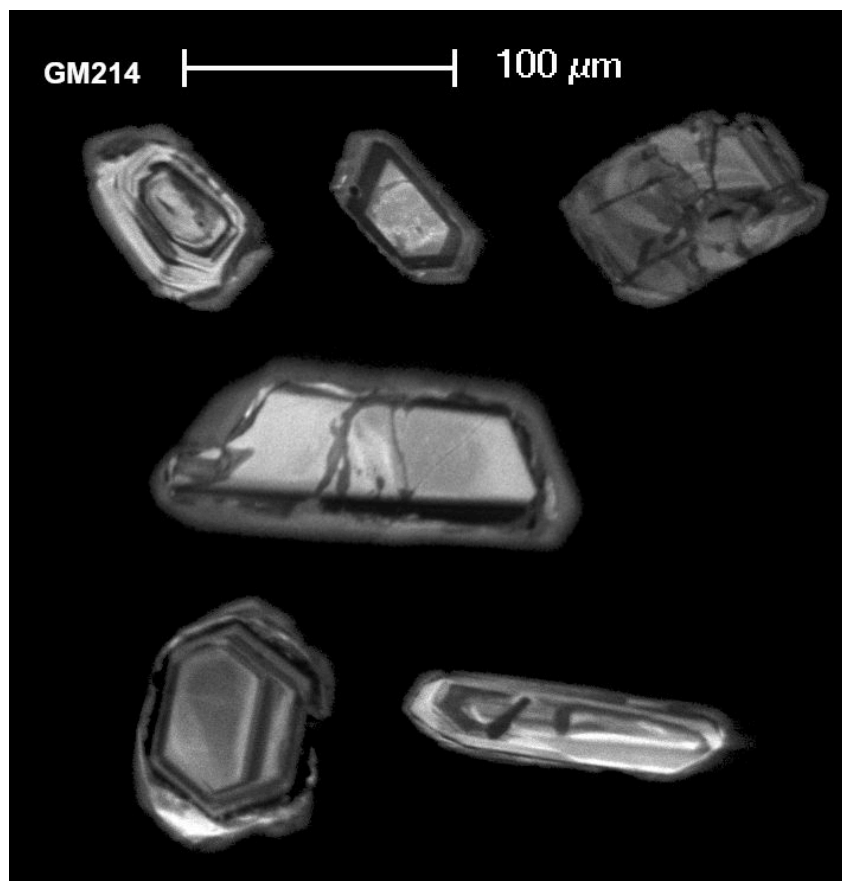


Figure 28: A representative selection of zircons from sample GM214.

5.4.3 CH2241

The shape of the zircons varies from prismatic euhedral to rounded and grains are pink to colorless. The CL imaging reveals that some crystals display weak oscillatory zoning and others are more homogeneous with a gray to white color. Only a few grains display inherited cores. The prismatic zircons are up to 100 μm long whereas the rounded are slightly smaller, up to 80 μm long. Commonly, zircons display a thin grey rim, no more than 10 μm thick. Many zircons are intensely fractured where the fractures are filled with a grey luminescent material. Some have inherited cores which are up to 30 μm in size and are characterized by oscillatory zoning, either broad or narrow. A representative selection of analysed zircons are given in Figure 29a, including the youngest and oldest obtained age. The Th/U ratio is highly variable, from 0.0-1.0 with the main cluster around 0.0-0.4 (Fig. 29b). In this diagram, zircons are classified in three groups; inherited cores, homogeneous and oscillatory crystals as well as rims and overgrowths. While the Th/U ratio of the first two groups are highly variable, rims and

overgrowths constantly display low Th/U ratio (<0.1). In total 120 zircons were analysed and 114 out of 120 are concordant. The ages obtained from the detrital zircons range from 316 to 2614 Ma (Fig. 29c & d). Dates younger than 400 Ma have been obtained solely on rims of zircon (Fig. 29a). The majority of dates define a main population around 600-750 Ma, whereas a second cluster comprises dates between 900 and 1000 Ma.

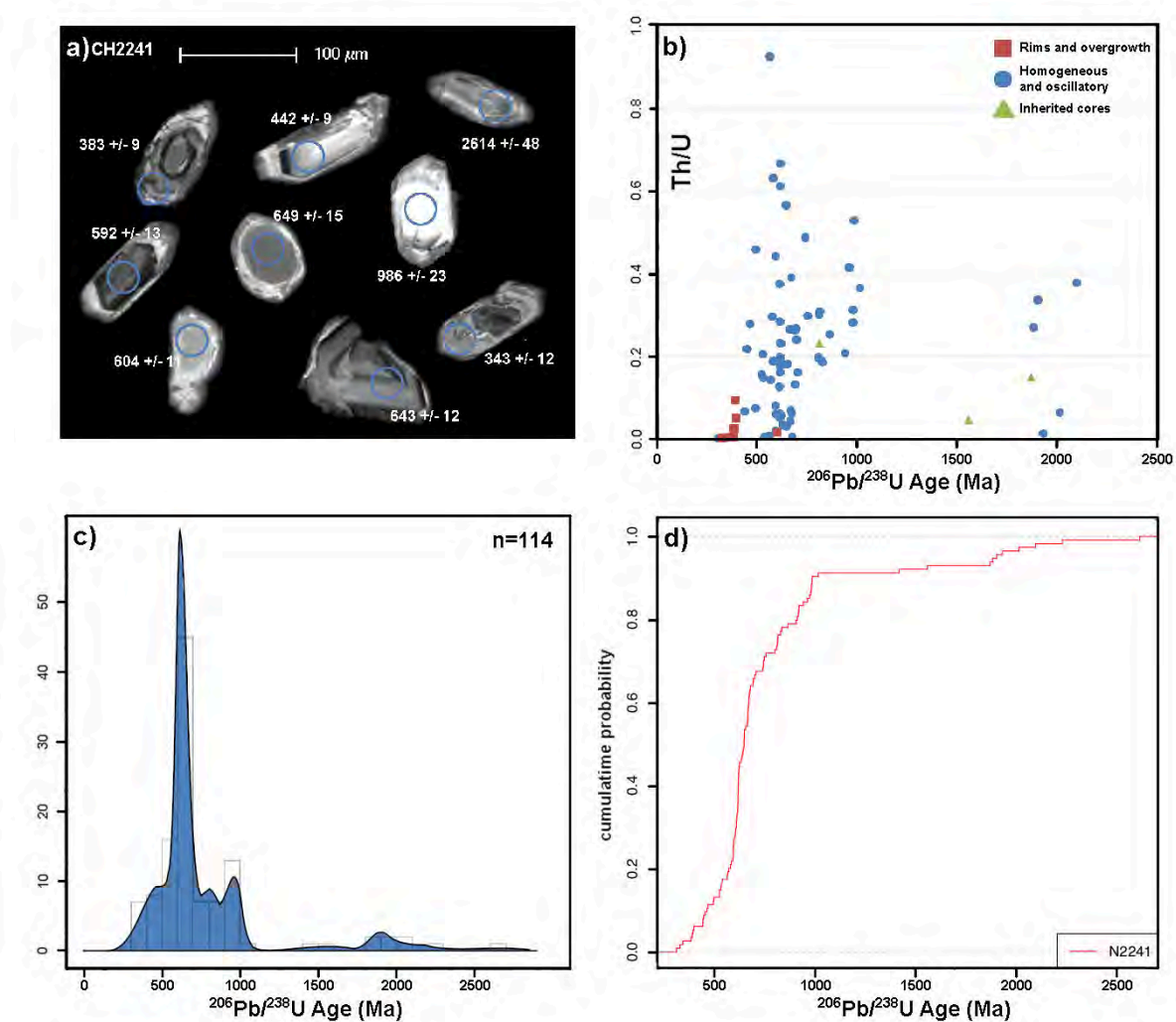


Figure 29: a) A representative selection of zircons used for dating. The blue circles indicate the ablation spot. The age of the analysed zircon is indicated adjacent to it. b) Th/U plot for sample CH2241. c) A Kernel Density plot showing the distribution of dates. d) Cumulative probability plot for CH2241.

5.4.4 CH2240

Zircons vary from prismatic to sub-rounded and are cloudy due to the presence of many tiny inclusions. Zircon size varies from around 60 μm to 200 μm long. The CL imaging reveals that most zircons have a dark outer rim, up to 15 μm thick. The majority of zircons has an inherited core with oscillatory zoning. Other grains lack zoning and appear homogeneous. The inherited cores are often partially resorbed. The outermost dark rim sometimes shows radial fracturing emanating from the inherited core. The fractures are filled by the same material which forms the dark outer rim. A representative selection of the analysed zircon is shown in Figure 30a. The Th/U ratio of the analysed zircon is variable, but generally medium to high (0.1-0.5), with the lowest being 0.01 and the highest 0.9 (Fig. 30b). In total, 48 analyses were performed of which 5 analyses on the black rim. 15 analyses out of 48 are discordant. The discordant analyses include all the ones done on the black rims. The zircons from sample CH2240 yield a concordant age at 532 \pm 2.5 Ma (n=32, MSWD=590) (Fig. 30c). However, the weighted mean average gives a mean of 597 \pm 3 Ma (n=21, MSWD=22) with a large spread around the mean value (Fig. 30d). Therefore, this age has no geological meaning.

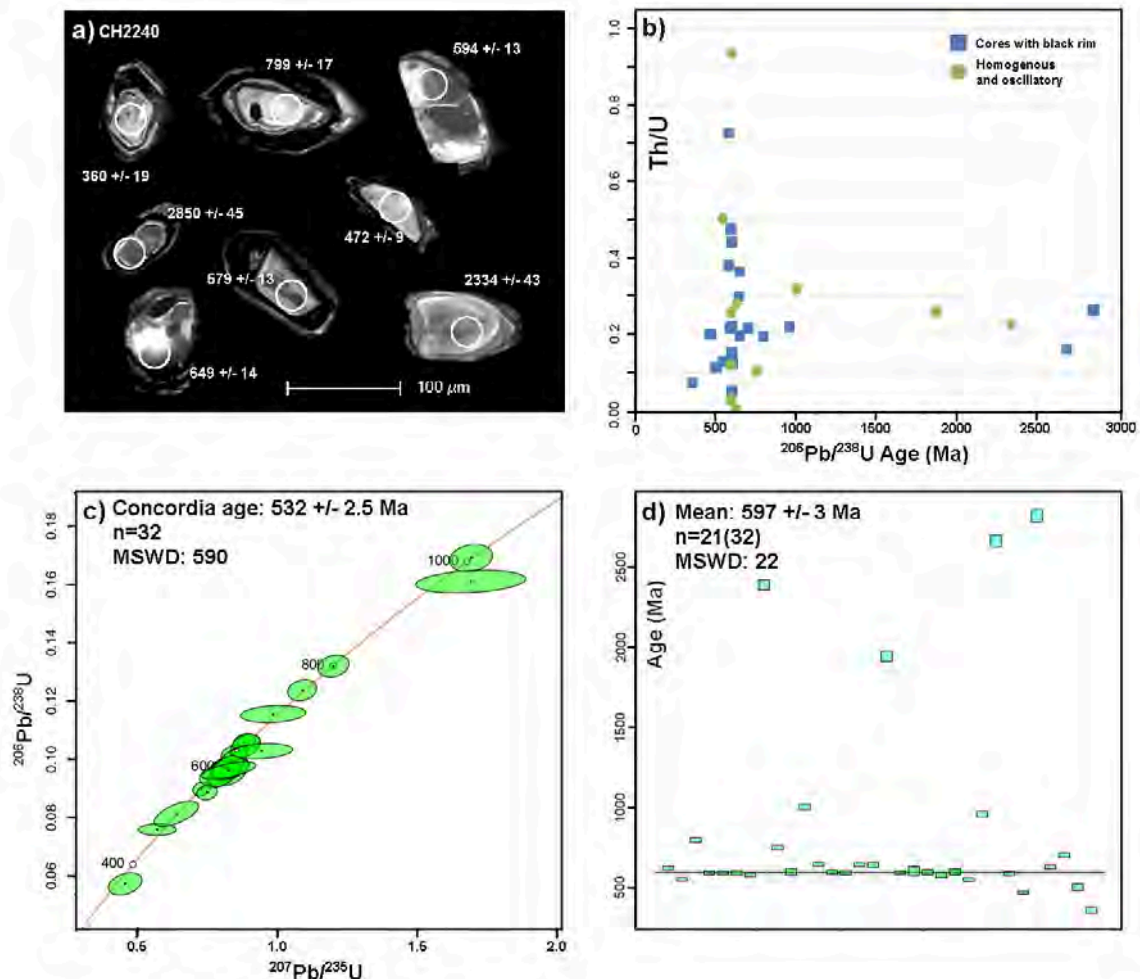


Figure 30: a) A representative selection of zircons used for dating. The white circles indicate the ablation spot. The age of the analysed zircon is indicated adjacent to it. b) Th/U plot for sample CH2240. c) Concordia plot for the felsic layer. MSWD is given in concordance+equivalence. d) Weighted mean plot for the felsic layer. MSWD is given in concordance+equivalence.

5.4.5 CH2249

The zircons are pinkish to colorless, dominantly euhedral and fairly large (up to 150 μm in size). Most of the zircons exhibit oscillatory zoning which is either narrow or broad. A representative selection of zircons is shown in Figure 31a. Most of the zircon display a low Th/U ratio, ranging between 0.03-0.40 (Fig. 31b). This low ratio also characterises the four older outliers. In total, 104 zircons were mounted. 28 analyses were done and 27 out of 28 provide concordant dates. The oldest concordant date is at 489 \pm 12 Ma whereas the youngest one is at 432 \pm 13 Ma. Four analyses are considered outliers with respect to the main population. 23 analyses define a concordant age at 440 \pm 2 Ma ($n=23$, MSWD=0.87) (Fig. 31c). The weighted mean of the analyses is 440 \pm 2 Ma ($n=23$, MSWD=0.93) (Fig. 31d). All zircons display similar trace element patterns characterised by a slight positive Cerium (Ce) anomaly, and a strong negative Europium (Eu) anomaly (Fig. 32). The trace element pattern for the four outliers are similar to the main population, but showing lower concentration.

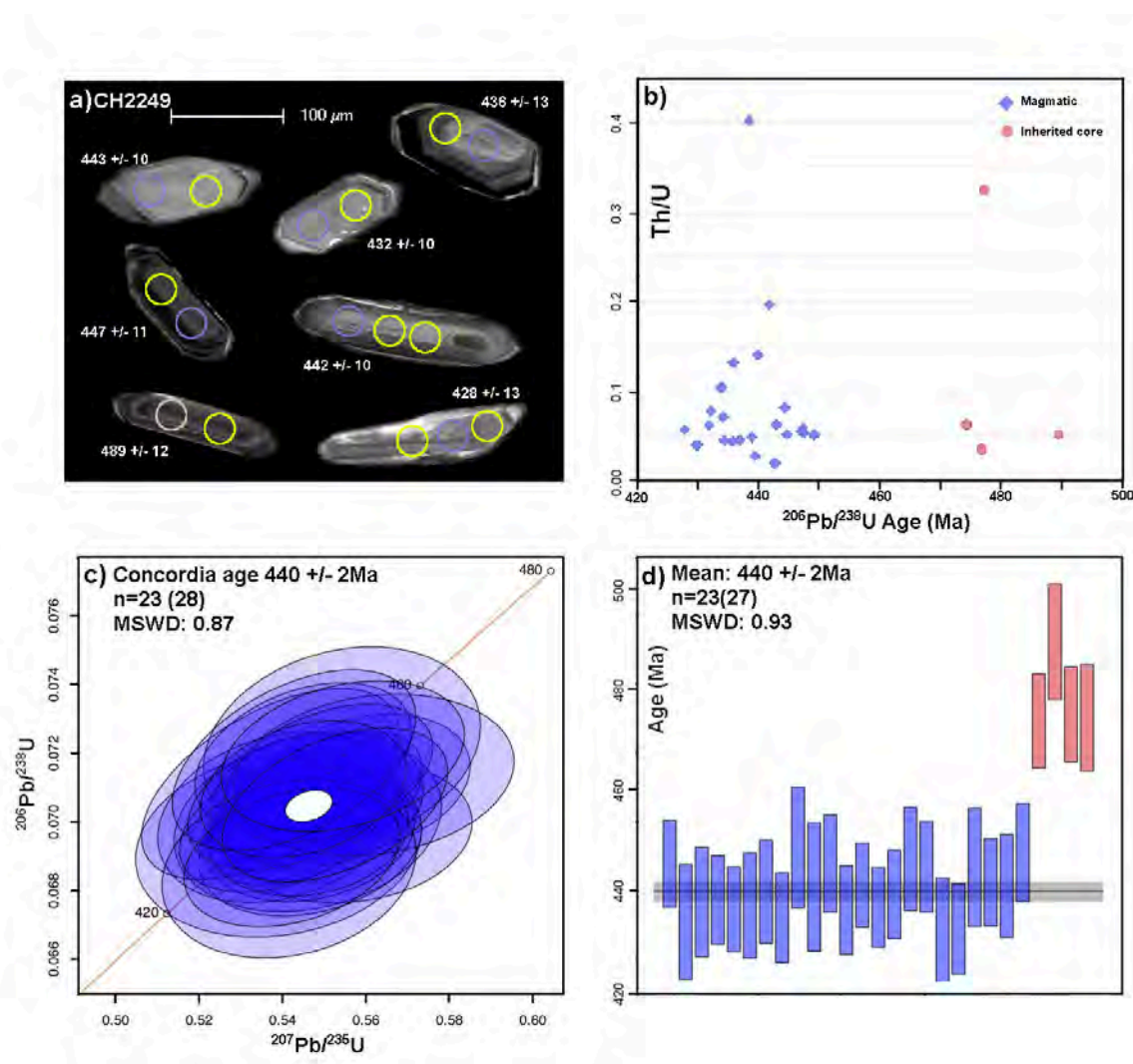


Figure 31: a) A representative selection of zircons used for dating. The blue and red circles indicate the ablation spot and the yellow circles indicate the spot for trace element analysis. The age of the analysed zircon is indicated adjacent to it. b) Th/U plot for sample CH2249. c) Concordia plot for the deformed orthogneiss. MSWD is given in concordance+equivalence. d) Weighted mean plot for sample CH2249. MSWD is given in concordance+equivalence.

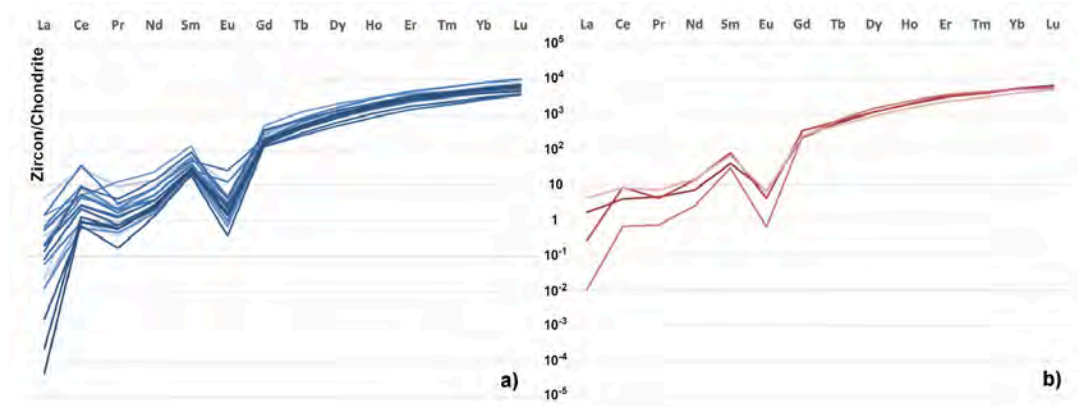


Figure 32: a) The trace element pattern for the zircons used for the concordia age. Zircons display a strong negative Eu anomaly, and a positive Ce anomaly. b) The trace element pattern of the four outliers (see Fig. 30d) are similar to the main population. The trace elements were normalized to chondrite (McDonough and Sun, 1995).

6 Discussion

6.1 Nature and timing of magmatism in the northern Dora-Maira Massif

While interpreting zircon ages, it is vital to consider the assumptions necessary for the U-Pb system. As previously introduced, these include the assumption that the system remained closed from the moment of zircon crystallisation up until today and that at the time of crystallisation the system was at equilibrium. In addition, the textures of the zircon population(s) should be taken into consideration since zircons may be inherited or altered during metamorphism or interaction with fluids. The orthogneiss (sample CH2249) yields a robust concordia age at 440 ± 2 Ma (MSWD=0.87) based on 23 out of 27 concordant dates. The four older zircons re interpreted to be inherited from a previous source (Fig. 31b). Since zircon is most commonly crystallising in silica-saturated magmas, they are generally a common constituent in felsic igneous rocks (Hoskin and Schaltegger, 2003). However, zircon inheritance is thought to be dependent on temperature in the magma, thus increasing inheritance reflect colder magmas (< 800 C) (Bea et al., 2021; Miller et al., 2003). The Th/U ratio of the zircons from the orthogneiss is generally low (median=0.06) (Fig. 31d), but still above the lower limit to be indicative for metamorphic zircon (0.01). Instead, it could reflect the presence of another Th-concentrating mineral such as monazite. The REE pattern for the orthogneiss, with the negative Europium anomaly is indicative of zircons crystallised in a granitic melt in which feldspar, which is the main sink for Europium, has already formed (Rubatto, 2002). In addition, the progressive enrichment in HREE and positive Cerium anomaly is typical of magmatic zircon (Hoskin and Schaltegger, 2003). Therefore, on the basis of all these considerations, the age at 440 ± 2 Ma (MSWD=0.87) can be interpreted to represent the time of the emplacement of the magmatic (granitic) protolith.

Although Ordovician magmatism is rare in the Internal Crystalline Massifs, it is widespread in the Alpine belt (von Raumer et al., 2002). In the internal western Alps, it has for example been recognized in the Ruitor Massif which belongs to the basement of the Briançonnais, but they record older magmatic events between 450-480 Ma (Guillot et al., 2002). The breakup of Gondwana, from which many Alpine units are thought to derive, initiated by the rifting associated with the opening of the Rheic Ocean was related to intense felsic magmatism. Although the this event is considered to have occurred during the Middle-Lower Ordovician (Ballèvre et al., 2012), the emplacement of the orthogneiss might be related to this rifting. It would indicate a

similar timing as the intrusion of the Muret orthogneiss (Nosenzo et al., 2022).

The interpretation of the felsic layer is fairly ambiguous due to the large spread of dates obtained from zircon. Despite defining a concordia age of 532 ± 2.5 Ma (MSWD=590), the variation of the obtained dates is large and the MSWD indicates that the age has no geological meaning. The youngest zircon yielded a date of 360 ± 19 Ma whereas the oldest zircon gave a date of 2334 ± 43 Ma. It should be noted that all the dates are obtained from zircon cores. During analysis several attempts were made to date the black rims which surround the cores (see Fig. 30a). However, the rims are rich in inclusions and no analysis yielded a concordant date. The Th/U ratio of analysed zircon is generally high compared to the ones of the zircon from the orthogneiss (median=0.22) (Fig. 30b). Based on these data, two main hypotheses can be advanced to explain the spread of dates displayed by the zircon analysed in the felsic layer: i) the felsic layer is in fact a quartz-rich layer interbedded with the sedimentary protolith of the micaschist, or ii) the felsic layer is indeed a deformed aplitic or granitic dyke, and it displays a large number of inherited crystals ($> 95\%$) from the country rocks meaning that no new growth of zircon occurred during crystallization of the magma. In the literature, there are studies that report dykes with no primary zircon (e.g. Pochon et al., 2016). Pochon et al. (2016) aimed to date the emplacement of mafic dykes in the Armorican Massif but due to the large inheritance of zircon from the country rocks, the authors resorted to date apatite to pinpoint the emplacement age. Following this second interpretation, it is possible that the black rims displayed by the zircon from the felsic dyke can have grown during the emplacement of the dyke whereas the cores are crystals inherited from the surrounding country rocks. This hypothesis seems quite plausible and thus the timing of the emplacement of the felsic dyke cannot be assessed based on the data obtained in this study.

6.2 Timing of sedimentation

The interpretation of detrital zircon populations and the youngest depositional age of a sediment is heavily dependent on statistics. Bias of the dates obtained is already potentially introduced during the mounting, when it is possible to unconsciously pick a preferred shape, size or color of zircon. However, with knowledge of the potential of bias and by analysing a large number of crystals, this risk can be minimized. Considering the large number of zircons analysed in this study, the dates and their distribution can be considered representative of the sediments. Hence, the youngest zircon obtained can be interpreted as the youngest depositional age.

In sample GM213, the youngest zircon date is at 511 ± 33 Ma whereas the oldest zircon date is at 2836 ± 78 Ma. These dates suggest that the youngest depositional age for micaschist GM213 was Cambrian. In sample CH2241, the youngest date is at 383 ± 9 Ma, which is obtained on a rim surrounding an inherited core (see Fig. 29c). A few dates range between 380-400 Ma and they are systematically obtained on rims and overgrowths. Furthermore, these data display low Th/U ratio (median=0.02) indicating a metamorphic origin and thus they do not represent the depositional age. The youngest date obtained on a crystal core is at 442 ± 9 Ma and the oldest age is 2614 ± 48 Ma, suggesting that the maximum age of deposition is Silurian. The distribution of zircon populations between both studied micaschist are similar (cf. 27c & 29c). Both samples have a main population of zircons recording a main Neoproterozoic population (600-750 Ma) and show several smaller populations which are even older (> 1000 Ma). Based on these distributions, it is likely that the detrital material of the two investigated metasediments may derive from the same sources.

6.3 Sediment provenance

Based on the detrital age pattern and the large number of zircon grains analysed in this study, it is possible to consider the provenance of the sediments constituting the investigated metasedimentary rocks. An episodic detrital zircon record as observed in micaschists GM213 and CH2241 is often observed in sedimentary basins which are draining the internal part of an orogenic belt (Cawood et al., 2012). Hence, the observed distribution of dates is a common feature of sediments deriving from a back-arc basin in a collisional setting or from a passive margin in an extensional setting. Given the depositional age of Cambro-Silurian, the estimated palaeogeographic position of the sediments should be considered. In the Western Alps, the Internal Crystalline Massifs belong to the Briançonnais microcontinent, which drifted from the European paleo-margin in the Cretaceous. In turn, it is hypothesized that many of the Alpine Units belonged to the European Hun Superterrane which was a set of microcontinents that drifted from the northern paleo-margin of Gondwana during the opening of the Rheic Ocean in the Ordovician (Franke et al., 2021; von Raumer et al., 2003). Early Ordovician to Silurian ages have been obtained in the Pre-Alpine basement of the Briançonnais domain in the Ligurian Alps which has been correlated to the evolution of an arc system related to the rifting associated with the Rheic Ocean (Maino et al., 2019)

Although there are very few detrital studies in the internal massifs, Bertrand et al. (2000) conducted a detrital study of the Belladonne Massif (external massif, see Fig. 1) and U-Pb dating of xenocrysts in orthogneisses in the Internal Massifs which showed that there is a large Pan-African component (590-630 Ma) in both the External and Internal Massifs. It shows that despite that the geological history of the External and Internal Massifs differ during the Variscan and Alpine orogeny, they share a similar older history. In a geochronological study in the Central Alps, Scheiber et al. (2014) reported detrital dates from the Neoproterozoic (2.7-2.5 Ga), Paleoproterozoic (2.2-1.9 Ga) and Neoproterozoic (800-550 Ma) and linked these populations to three main crustal growth episodes. The sediments record a maximum age of deposition at the Cambrian-Ordovician boundary. The authors interpreted the Neoproterozoic crustal events to be associated with the Pan-African orogenic cycle. The Cambro-Ordovician sandstones of North Africa are also thought to have belonged to Peri-Gondwana, and a recent study of detrital geochronology revealed a main zircon population at 550-650 Ma (Avigad et al., 2005). Hence, these sediments were interpreted as first-cycle detritus from the Pan-African basement. In comparison to other metasedimentary rocks thought to derive from the northern Peri-Gondwana, the presently studied micaschists display striking similarities in the detrital zircon population patterns. Therefore, it is likely that they record a similar history as the above mentioned units in terms of sedimentation.

In a recent study, Stephan et al. (2019a) compiled detrital zircon age patterns from across Europe with the aim of reconstructing the northern paleo-margin of Gondwana. Based on zircon provenance, Peri-Gondwana can be divided in two main zircon provinces, namely the West African and East Africa-Arabia (Stephan et al., 2019b). Sediments belonging to the West African zircon province show predominantly old (> 2000 Ma) whereas those stemming from the East Africa-Arabia province show a significant Grenvillian peak (≈ 1000 Ma) (Stephan et al., 2019a). Previously, it has been shown that the Grenvillian (assembly of Rodinia) and Pan-African (assembly of Gondwana) orogens had high sediment flux and preservation potential and generated large amounts of sediment dispersed in vast river systems which can now be found in several sedimentary units across the globe (Rainbird et al., 2011). Additionally, it has been recognized that erosion of the Pan-African belt likely resulted in a large sediment influx to the Gondwana paleo-margin leading to the formation of graywackes and pelites (Zurbruggen, 2015). Based on the distribution of zircon populations, it is likely that the sediments now constituting the metasedimentary rocks in the Germanasca valley, belong to the East Africa-Arabian zircon province of northern Peri-Gondwana.

6.4 Refining the geometry of the nappe stack

The samples investigated in this study have been collected in the Germanasca valley, in the northern Dora-Maira Massif. According to previous studies (e.g. Vialon, 1966), the tectonic boundary between the Pinerolo and Muret Units is oriented north-south and is approximately located in correspondence of the Rabbioso bridge (Fig. 33a). However, no tectonic boundary between these two units can be observed in this area during fieldwork. Recent investigations in the area also reveals the presence of a new UHP unit (the Chasteiran Unit, Manzotti et al., 2022) made of micaschists and located structurally above the Pinerolo Unit (Fig. 33b). The discovery of a new UHP unit, located structurally above the Pinerolo Unit challenges the geometry of the nappe stack in the northern Dora-Maira Massif. While the Pinerolo Unit is made of metaconglomerates and metasediments which are Upper Carboniferous in age (Manzotti et al., 2016), the characteristic conglomerates are absent in the Chasteiran Unit and this unit only consists of micaschists that may derive from black shales of Silurian age (Manzotti et al., 2022).

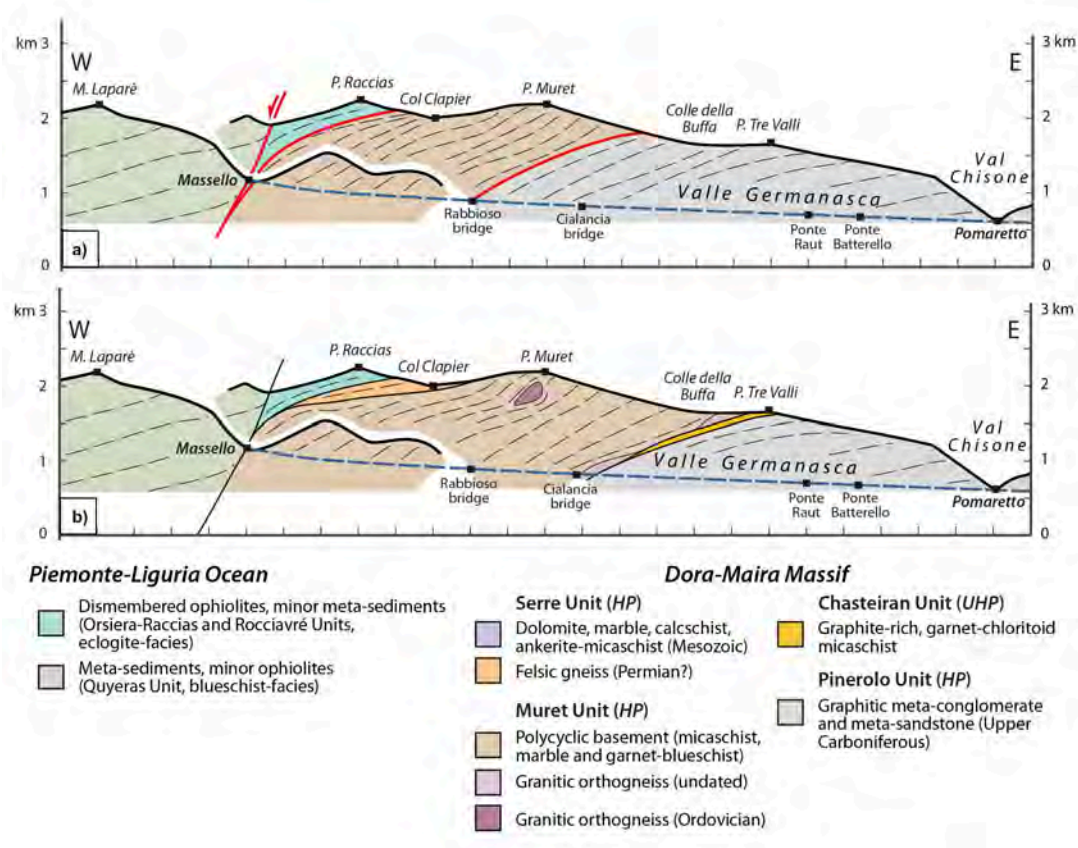


Figure 33: a) Cross-section of the Germanasca valley as proposed in previous studies (e.g. Vialon, 1966). b) Cross-section of the Germanasca valley as proposed following the discovery of the Chasteiran Unit (Manzotti et al., 2022).

In this study, geochronology, geochemistry and petrography were applied on selected samples in order to refine the architecture of the northern Dora-Maira Massif. In particular, the investigation aims to assess if the section between the Chasteiran Unit and the Rabbioso bridge belongs to the Muret Unit or not. The mylonitic orthogneiss sample (CH2249) dated in this study was collected just above the contact with the Chasteiran Unit in the southern Germanasca valley. It yields an Ordovician concordia age (440 ± 2 Ma) for the magmatic protolith. This age is very similar to the one of the undeformed Muret orthogneiss (Fig. 34) in the Muret Unit (442 ± 2 Ma, Bussy and Cadoppi, 1996; Nosenzo et al., 2022). These two bodies are geochemi-

cally slightly different, being granitic and granodioritic, respectively (Fig. 22) although both being peraluminous and calc-alkaline (Fig. 23 and 24). Geochronological data indicate that the mylonitic orthogneiss situated structurally above the Chasteiran Unit cannot be part of the Pinerolo Unit because it is Ordovician in age; instead it is part of the basement unit, i.e. the Muret Unit. In the East Africa-Arabia zircon province to which the studied micaschists are interpreted to source from, Ordovician magmatism is recognized and it is reported as peraluminous and calc-alkaline (Stephan et al., 2019b). The findings of the present study is in agreement with these observations.

Detrital zircon geochronology was performed on two metasediments collected close to the Cialancia (sample CH2241) and Rabbioso (sample GM213) bridges (Fig. 10). In this area, located west of the Chasteiran Unit and the mylonitic orthogneiss, conglomerates, a typical lithology found in the Pinerolo Unit and more generally in Carboniferous basins, are not present (Opluštil et al., 2013). In the Pinerolo Unit, two main stages of zircon accumulation have been identified (Fig. 34 and 35). Differently from the Pinerolo Unit (Manzotti et al., 2016), no Upper Carboniferous zircons have been found in samples CH2241 or GM213, and their maximum age of deposition is Silurian and Cambrian, respectively. Interestingly, the youngest detrital zircons in the two micaschist samples from the Muret Unit investigated by Nosenzo et al. (2022) are Ordovician and Silurian (Fig. 34), suggesting that sedimentation occurred in this period. Lastly, the major element compositions of the investigated micaschists is more similar to the ones of the Muret and Chasteiran Units (Manzotti et al., 2022; Nosenzo et al., 2022) as opposed to the Pinerolo Unit (Larsson, 2022) (Fig. 25).

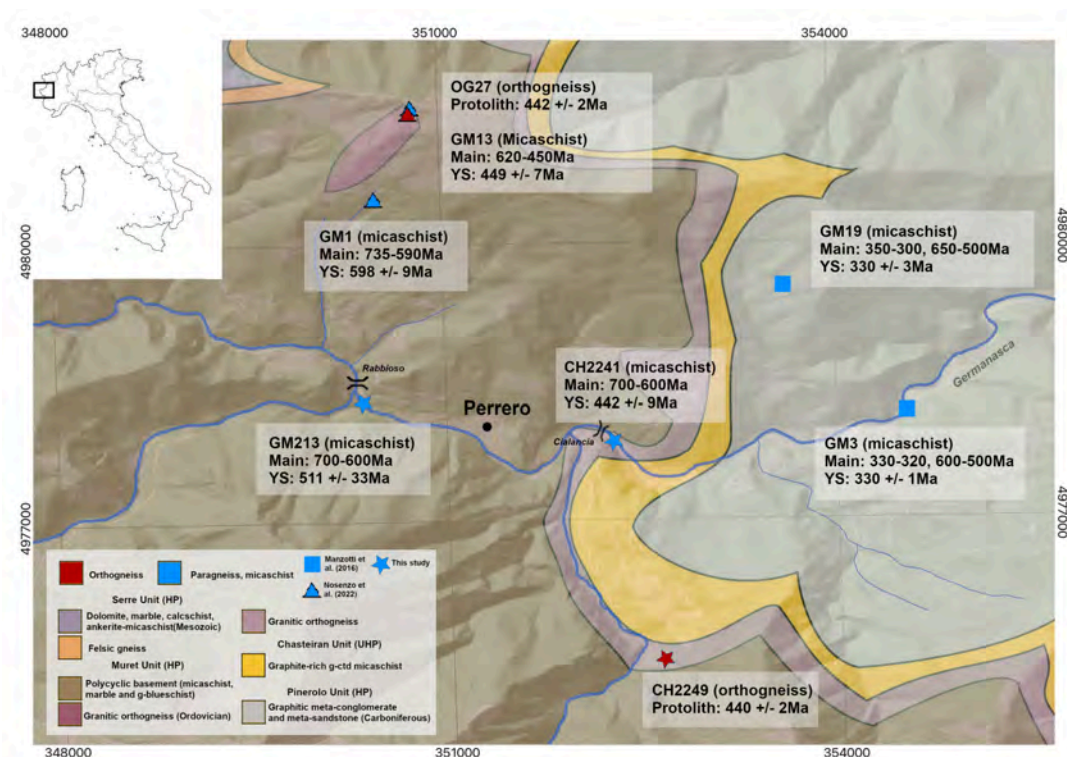


Figure 34: A map showing results from previous geochronological studies in the Germanasca valley. The data from samples OG27, GM1 and GM13 was retrieved from Nosenzo et al. (2022) whereas the data from GM19 and GM3 was from Manzotti et al. (2016). The DEM was retrieved from Tarquini et al. (2007). Main=Main population of zircon. YS=Interpreted youngest sedimentation. The coordinate system used is ED50/UTM zone 32N.

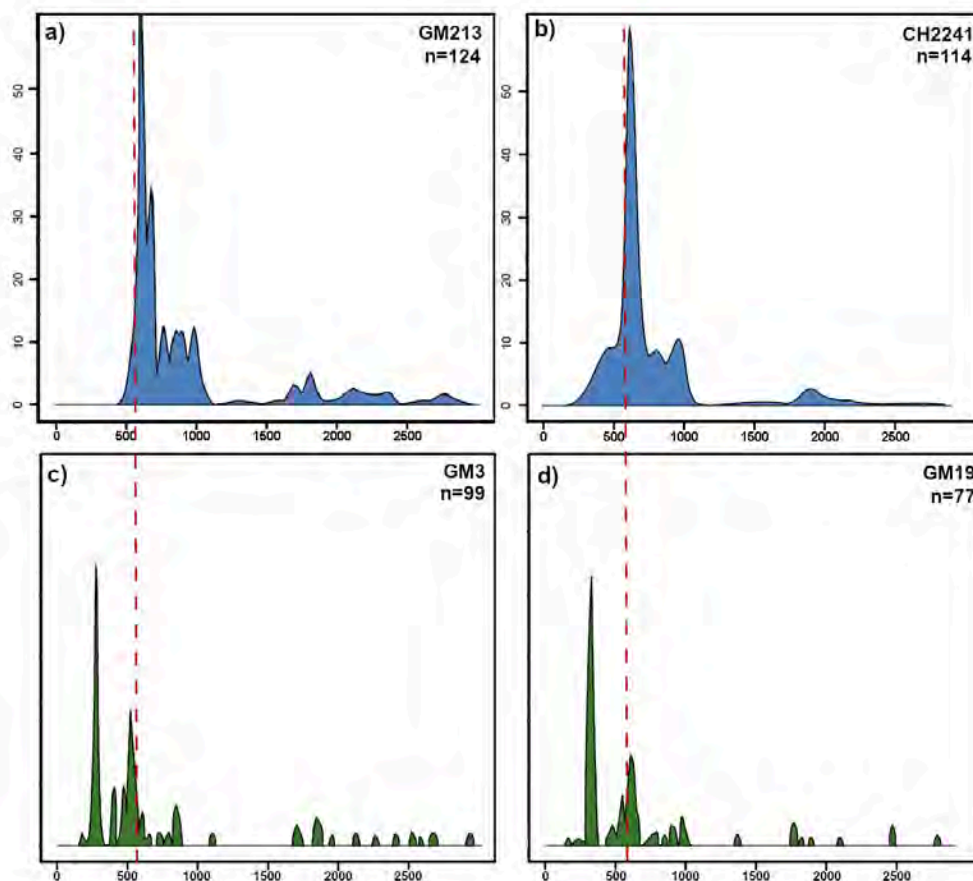


Figure 35: A comparison of the Kernel Density plots of the two micaschists dated in this study (GM213 and CH2241) and the two micaschists from the Pinerolo Unit (GM3 and GM19) studied by Manzotti et al. (2016). Note that the scale for GM3 and GM19 is relative. The dashed red line indicates 600 Ma on the timeline.

On the basis of these data, it is strongly suggested that the area comprised between the Chasteiran Unit and the Rabbioso bridge is made of a Palaeozoic basement and thus belongs to the Muret Unit, as proposed by Manzotti et al. (2022). This conclusion is enforced primarily by two findings. Firstly, the age distributions in the investigated metasediments do not display a Carboniferous population as the Pinerolo samples and they are very similar to the ones of the Muret micaschists with regards to depositional age. Secondly, the Ordovician age of the mylonitic orthogneiss structurally above the Chasteiran Unit indicates that the sediments which this body intruded or was deposited on must be older than 440 Ma, hence they cannot belong to the Carboniferous Pinerolo Unit.

In a larger context, the geometry of the Alpine nappe stack has important implications for the tectonic model of continental subduction and its subsequent exhumation. The structure of the Western Alps suggests that it consists of cover nappes which were detached from its basement and they outcrop in different areas (Ballèvre et al., 2020). Most likely, the external Briançonnais domain represents a sequence of detached cover nappes to which the tectonic units of the Dora-Maira Massif is the basement (Ballèvre et al., 2020). The discovery of the UHP Chasteiran Unit prompted a re-evaluation of the internal structure of the northern Dora-Maira Massif. This UHP sliver is sandwiched between the HP Pinerolo Unit and the HP Muret Unit, which is similar to the assembly in the southern Dora-Maira Massif where the UHP Brossasco-Isasca Unit is sandwiched between two HP units (the San Chiaffredo Unit and the Rocca Solei Unit)

(Groppo et al., 2019). Hence, these two UHP units occupy the same structural position and indicate the UHP rocks are thrust over HP rocks. By moving the tectonic boundary between the Muret and Pinerolo Units to the east, and placing the Chasteiran Unit in the middle it is inferred that slices of the continental crust were detached during subduction and reached different peak P-T conditions at different times.

7 Conclusion and future perspectives

This study applies geochronology, geochemistry and petrography on selected samples in order to refine the architecture of the northern Dora-Maira Massif. In the Germanasca valley, the area comprised between the Cialancia and Rabbioso bridges belongs to the Muret Unit and not to the Pinerolo Unit, as previously suggested. This new interpretation is supported by (i) the Ordovician age (440 +/- 2 Ma) of the magmatic protolith of the mylonitic orthogneiss located structurally above the Chasteiran Unit and by (ii) the Cambro-Silurian depositional age of the metasediments in this area. From a palaeogeographic point of view, the source of these metasediments can be identified in the East Africa-Arabia province of Peri-Gondwana.

In summary, the following conclusions have been made in this study.

- The emplacement age of the felsic layer could not be constrained, which might indicate that it is a dyke with large zircon inheritance or that it is a quartz-rich metasedimentary layer within the micaschist.
- The age of the magmatic protolith for the orthogneiss is 440 Ma and likely associated with felsic magmatism in the Ordovician at the northern paleo-margin of Gondwana.
- The depositional age of the metasediments is Cambro-Silurian and the most prominent zircon population is 600-750 Ma. They could source from the East Africa-Arabia zircon province of Peri-Gondwana with detritus deriving mainly from the Pan-African belt.
- On the basis of petrological and geochronological data, the present study concludes that the metasediments previously ascribed to the Pinerolo Unit instead belong to the Muret Unit.

In this study, it was not possible to determine the crystallisation age of the felsic layer or provide undisputable evidence that it is a magmatic dyke and not a felsic layer in the metasediments. However, a future study could conduct further investigation of this sample using the following approaches. Apatite, which is less likely inherited, can be dated and thus can provide the age of the dyke emplacement. In addition, further investigations can be conducted on the white mica present in the layer. In particular, the identification of a chemical zoning by SEM imaging can be used to determine if this mineral is igneous or metamorphic.

Recent efforts have expanded the knowledge of the northern region, which the present study has built upon. However, there are many ideas for future perspectives in this area. Now that the age of the metasedimentary rocks is well constrained, one could direct further research in determining its P-T history using detailed investigation of its mineralogy and related chemistry through SEM and Electron Microprobe. Additionally, the P-T path could be explored by utilizing thermodynamic modelling. To further constrain the geometry of the nappe stack, a next step would be to conduct geochronology of the UHP sliver, the Chasteiran Unit, in order to classify the unit further.

References

- Avigad D, Chopin C, and Le Bayon R. Thrusting and Extension in the Southern Dora-Maira Ultra-High-Pressure Massif (Western Alps): View from Below the Coesite-Bearing Unit. *The Journal of Geology*, 111(1):57–70, 2003. doi: 10.1086/344664. Publisher: The University of Chicago Press.
- Avigad D, Sandler A, Kolodner K, Stern RJ, McWilliams M, Miller N, and Beyth M. Mass-production of Cambro–Ordovician quartz-rich sandstone as a consequence of chemical weathering of Pan-African terranes: Environmental implications. *Earth and Planetary Science Letters*, 240(3):818–826, 2005. doi: 10.1016/j.epsl.2005.09.021.
- Ballèvre M, Fourcade S, Capdevila R, Peucat JJ, Cocherie A, and Fanning CM. Geochronology and geochemistry of Ordovician felsic volcanism in the Southern Armorican Massif (Variscan belt, France): Implications for the breakup of Gondwana. *Gondwana Research*, 21(4):1019–1036, 2012. doi: 10.1016/j.gr.2011.07.030.
- Ballèvre M, Manzotti P, and Dal Piaz GV. Pre-Alpine (Variscan) Inheritance: A Key for the Location of the Future Valaisan Basin (Western Alps). *Tectonics*, 37(3):786–817, 2018. doi: 10.1002/2017TC004633.
- Ballèvre M, Camonin A, Manzotti P, and Poujol M. A step towards unraveling the paleogeographic attribution of pre-Mesozoic basement complexes in the Western Alps based on U–Pb geochronology of Permian magmatism. *Swiss Journal of Geosciences*, 113(1):12, 2020. doi: 10.1186/s00015-020-00367-1.
- Bea F, Morales I, Molina JF, Montero P, and Cambeses A. Zircon stability grids in crustal partial melts: implications for zircon inheritance. *Contributions to Mineralogy and Petrology*, 176(3):18, 2021. doi: 10.1007/s00410-021-01772-x.
- Belousova E, Griffin W, O’Reilly SY, and Fisher N. Igneous zircon: trace element composition as an indicator of source rock type. *Contributions to Mineralogy and Petrology*, 143(5):602–622, 2002. doi: 10.1007/s00410-002-0364-7.
- Bertrand J, Pidgeon R, Leterrier J, Guillot F, Gasquet D, and Gattiglio M. SHRIMP and IDTIMS U–Pb zircon ages of the pre-Alpine basement in the Internal Western Alps (Savoy and Piemonte). *Schweizerische Mineralogische und Petrographische Mitteilungen*, 80:225–248, 2000.
- Bonnet G, Chopin C, Locatelli M, Kylander-Clark ARC, and Hacker BR. Protracted Subduction of the European Hyperextended Margin Revealed by Rutile U–Pb Geochronology Across the Dora-Maira Massif (Western Alps). *Tectonics*, 41(4):e2021TC007170, 2022. doi: 10.1029/2021TC007170. eprint: <https://onlinelibrary.wiley.com/doi/pdf/10.1029/2021TC007170>.
- Bowring SA and Schmitz MD. High-Precision U–Pb Zircon Geochronology and the Stratigraphic Record. *Reviews in Mineralogy and Geochemistry*, 53(1):305–326, 2003. doi: 10.2113/0530305.
- Bussy F and Cadoppi P. U–Pb zircon dating of granitoids from the Dora-Maira massif (western Italian Alps). *Schweizerische Mineralogische und Petrographische Mitteilungen*, 76:217–233, 1996.
- Cawood P, Hawkesworth C, and Dhuime B. Detrital zircon record and tectonic setting. *Geology*, 40(10):875–878, 2012. doi: 10.1130/G32945.1.
- Chen YX, Zhou K, Zheng YF, and Schertl HP. Zircon geochemical constraints on the protolith nature and metasomatic process of the Mg-rich whiteschist from the Western Alps. *Chemical Geology*, 467:177–195, 2017. doi: 10.1016/j.chemgeo.2017.08.013.

- Chopin C. Coesite and pure pyrope in high-grade blueschists of the Western Alps: a first record and some consequences. *Contributions to Mineralogy and Petrology*, 86(2):107–118, 1984. doi: 10.1007/BF00381838.
- Chopin C, Henry C, and Michard A. Geology and petrology of the coesite-bearing terrain, Dora Maira massif, Western Alps. *European Journal of Mineralogy*, pages 263–292, 1991. doi: 10.1127/ejm/3/2/0263. Publisher: Schweizerbart'sche Verlagsbuchhandlung.
- Corfu F, Hanchar JM, Hoskin PW, and Kinny P. Atlas of Zircon Textures. *Reviews in Mineralogy and Geochemistry*, 53(1):469–500, 2003. doi: 10.2113/0530469.
- De La Roche H, Leterrier J, Grandclaude P, and Marchal M. A classification of volcanic and plutonic rocks using R 1 R 2 -diagram and major-element analyses — Its relationships with current nomenclature. *Chemical Geology*, 29(1-4):183–210, 1980. doi: 10.1016/0009-2541(80)90020-0.
- Faure G and Mensing T. *Isotopes: Principles and Applications*. John Wiley & Sons, 3rd edition, 2003. ISBN 978-0-471-38437-3.
- Fedo CM, Sircombe KN, and Rainbird RH. Detrital Zircon Analysis of the Sedimentary Record. *Reviews in Mineralogy and Geochemistry*, 53(1):277–303, 2003. doi: 10.2113/0530277.
- Flanagan FJ. U.S. Geological Survey standards—II. First compilation of data for the new U.S.G.S. rocks. *Geochimica et Cosmochimica Acta*, 33(1):81–120, 1969. doi: 10.1016/0016-7037(69)90094-5.
- Flanagan FJ. *Descriptions and Analyses of Eight New USGS Rock Standards*, volume Geological Survey Professional Paper 840. 1976.
- Flanagan FJ. U.S. Geological Survey silicate rock standards. *Geochimica et Cosmochimica Acta*, 31(3):289–308, 1967. doi: 10.1016/0016-7037(67)90043-9.
- Franke W, Ballèvre M, Cocks LRM, Torsvik TH, and Żelaźniewicz A. Variscan Orogeny. page 338, 2021. doi: 10.1016/B978-0-08-102908-4.00022-9. Publisher: Elsevier.
- Frost BR and Frost CD. A Geochemical Classification for Feldspathic Igneous Rocks. *Journal of Petrology*, 49(11):1955–1969, 2008. doi: 10.1093/petrology/egn054.
- Gehrels G. Detrital zircon U-Pb geochronology applied to tectonics. *Annual Review of Earth and Planetary Sciences*, 42:127–149, 2014. doi: 10.1146/annurev-earth-050212-124012.
- Gilbert S and Glorie S. Removal of Hg interferences for common Pb correction when dating apatite and titanite by LA-ICP-MS/MS. *Journal of Analytical Atomic Spectrometry*, 35(7): 1472–1481, 2020. doi: 10.1039/D0JA00224K. Publisher: Royal Society of Chemistry.
- Groppo C, Ferrando S, Gilio M, Botta S, Nosenzo F, Balestro G, Festa A, and Rolfo F. What's in the sandwich? New P–T constraints for the (U)HP nappe stack of southern Dora-Maira Massif (Western Alps). *European Journal of Mineralogy*, 31(4):665–683, 2019. doi: 10.1127/ejm/2019/0031-2860.
- Guillot F, Schaltegger U, Bertrand JM, Deloule and Baudin T. Zircon U–Pb geochronology of Ordovician magmatism in the polycyclic Ruitor Massif (Internal W Alps). *International Journal of Earth Sciences*, 91(6):964–978, 2002. doi: 10.1007/s00531-002-0280-0.
- Handy MR, M. Schmid S, Bousquet R, Kissling E, and Bernoulli D. Reconciling plate-tectonic reconstructions of Alpine Tethys with the geological–geophysical record of spreading and subduction in the Alps. *Earth-Science Reviews*, 102(3):121–158, 2010. doi: 10.1016/j.earscirev.2010.06.002.

- Hawkesworth C, Cawood P, Kemp T, Storey C, and Dhuime B. A Matter of Preservation. *Science*, 323(5910):49–50, 2009. doi: 10.1126/science.1168549. Publisher: American Association for the Advancement of Science.
- Henry C, Michard A, and Chopin C. Geometry and structural evolution of ultra-high-pressure and high-pressure rocks from the Dora-Maira massif, Western Alps, Italy. *Journal of Structural Geology*, 15(8):965–981, 1993. doi: 10.1016/0191-8141(93)90170-F.
- Hiess J, Condon DJ, McLean N, and Noble SR. 238U/235U Systematics in Terrestrial Uranium-Bearing Minerals. *Science*, 335(6076):1610–1614, 2012. doi: 10.1126/science.1215507. Publisher: American Association for the Advancement of Science.
- Horstwood MSA, Košler J, Gehrels G, Jackson SE, McLean NM, Paton C, Pearson NJ, Sircombe K, Sylvester P, Vermeesch P, Bowring JF, Condon DJ, and Schoene B. Community-Derived Standards for LA-ICP-MS U-(Th-)Pb Geochronology – Uncertainty Propagation, Age Interpretation and Data Reporting. *Geostandards and Geoanalytical Research*, 40(3):311–332, 2016. doi: 10.1111/j.1751-908X.2016.00379.x. eprint: <https://onlinelibrary.wiley.com/doi/pdf/10.1111/j.1751-908X.2016.00379.x>.
- Hoskin PWO and Schaltegger U. The Composition of Zircon and Igneous and Metamorphic Petrogenesis. *Reviews in Mineralogy and Geochemistry*, 53(1):27–62, 2003. doi: 10.2113/0530027.
- Ingalls M, Rowley DB, Currie B, and Colman AS. Large-scale subduction of continental crust implied by India–Asia mass-balance calculation. *Nature Geoscience*, 9(11):848–853, 2016. doi: 10.1038/ngeo2806. Number: 11 Publisher: Nature Publishing Group.
- Irvine TN and Baragar WRA. A Guide to the Chemical Classification of the Common Volcanic Rocks. *Canadian Journal of Earth Sciences*, 8(5):523–548, 1971. doi: 10.1139/e71-055.
- Jackson SE, Pearson NJ, Griffin WL, and Belousova EA. The application of laser ablation-inductively coupled plasma-mass spectrometry to in situ U–Pb zircon geochronology. *Chemical Geology*, 211(1):47–69, 2004. doi: 10.1016/j.chemgeo.2004.06.017.
- Jaffey AH, Flynn KF, Glendenin LE, Bentley WC, and Essling AM. Precision Measurement of Half-Lives and Specific Activities of ^{235}U and ^{238}U . *Physical Review C*, 4(5):1889–1906, 1971. doi: 10.1103/PhysRevC.4.1889. Publisher: American Physical Society.
- Kirkland CL, Smithies RH, Taylor RJM, Evans N, and McDonald B. Zircon Th/U ratios in magmatic environs. *Lithos*, 212-215:397–414, 2015. doi: 10.1016/j.lithos.2014.11.021.
- Kohn MJ, Corrie SL, and Markley C. The fall and rise of metamorphic zircon. *American Mineralogist*, 100(4):897–908, 2015. doi: 10.2138/am-2015-5064. Publisher: De Gruyter.
- Košler J. Laser ablation ICP—MS — a new dating tool in Earth science. *Proceedings of the Geologists’ Association*, 118(1):19–24, 2007. doi: 10.1016/S0016-7878(07)80043-5.
- Košler J and Sylvester PJ. Present Trends and the Future of Zircon in Geochronology: Laser Ablation ICPMS. *Reviews in Mineralogy and Geochemistry*, 53(1):243–275, 2003. doi: 10.2113/0530243.
- Krogh TE. Improved accuracy of U-Pb zircon ages by the creation of more concordant systems using an air abrasion technique. *Geochimica et Cosmochimica Acta*, 46(4):637–649, 1982. doi: 10.1016/0016-7037(82)90165-X.
- Larsson G. *Blueschist- or eclogite-facies? Re-assessing the peak P-T conditions of the Pinerolo Unit (Western Alps)*. BSc Thesis, Stockholm University, 2022.

- Maino M, Gaggero L, Langone A, Seno S, and Fanning M. Cambro-Silurian magmatisms at the northern Gondwana margin (Penninic basement of the Ligurian Alps). *Geoscience Frontiers*, 10(1):315–330, 2019. doi: 10.1016/j.gsf.2018.01.003.
- Manzotti P, Ballèvre M, Zucali M, Robyr M, and Engi M. The tectonometamorphic evolution of the Sesia–Dent Blanche nappes (internal Western Alps): review and synthesis. *Swiss Journal of Geosciences*, 107(2):309–336, 2014. doi: 10.1007/s00015-014-0172-x. Number: 2 Publisher: SpringerOpen.
- Manzotti P, Ballèvre M, and Poujol M. Detrital zircon geochronology in the Dora-Maira and Zone Houillère: a record of sediment travel paths in the Carboniferous. *Terra Nova*, 28(4):279–288, 2016. doi: 10.1111/ter.12219. eprint: <https://onlinelibrary.wiley.com/doi/pdf/10.1111/ter.12219>.
- Manzotti P, Schiavi F, Nosenzo F, Pitra P, and Ballèvre M. A journey towards the forbidden zone: a new, cold, UHP unit in the Dora-Maira Massif (Western Alps). *Contributions to Mineralogy and Petrology*, 177(6):59, 2022. doi: 10.1007/s00410-022-01923-8.
- Mattinson JM, Graubard CM, Parkinson DL, and McClelland WC. U-Pb reverse discordance in zircons: The role of fine-scale oscillatory zoning and sub-micron transport of Pb. *Washington DC American Geophysical Union Geophysical Monograph Series*, 95:355–370, 1996. doi: 10.1029/GM095p0355. ADS Bibcode: 1996GMS....95..355M.
- McDonough WF and Sun Ss. The composition of the Earth. *Chemical Geology*, 120(3):223–253, 1995. doi: 10.1016/0009-2541(94)00140-4.
- Mezger K and Krogstad EJ. Interpretation of discordant U-Pb zircon ages: An evaluation. *Journal of Metamorphic Geology*, 15(1):127–140, 1997. doi: 10.1111/j.1525-1314.1997.00008.x. eprint: <https://onlinelibrary.wiley.com/doi/pdf/10.1111/j.1525-1314.1997.00008.x>.
- Miller CF, McDowell SM, and Mapes RW. Hot and cold granites? Implications of zircon saturation temperatures and preservation of inheritance. *Geology*, 31(6):529–532, 2003. doi: 10.1130/0091-7613(2003)031<0529:HACGIO>2.0.CO;2.
- Möller A, Ó'Brien PJ, Kennedy A, and Kröner A. The Use and Abuse of Th-U Ratios in the Interpretation of Zircon. page 12113, 2003. Conference Name: EGS - AGU - EUG Joint Assembly ADS Bibcode: 2003EAEJA....12113M.
- Nosenzo F, Manzotti P, Poujol M, Ballèvre M, and Langlade J. A window into an older orogenic cycle: P–T conditions and timing of the pre-Alpine history of the Dora-Maira Massif (Western Alps). *Journal of Metamorphic Geology*, 40(4):789–821, 2022. doi: 10.1111/jmg.12646. eprint: <https://onlinelibrary.wiley.com/doi/pdf/10.1111/jmg.12646>.
- Opluštil S, Šimůnek Z, Zajíč J, and Mencl V. Climatic and biotic changes around the Carboniferous/Permian boundary recorded in the continental basins of the Czech Republic. *International Journal of Coal Geology*, 119:114–151, 2013. doi: 10.1016/j.coal.2013.07.014.
- Paton C, Woodhead JD, Hellstrom JC, Hergt JM, Greig A, and Maas R. Improved laser ablation U-Pb zircon geochronology through robust downhole fractionation correction. *Geochemistry, Geophysics, Geosystems*, 11(3), 2010. doi: 10.1029/2009GC002618. eprint: <https://onlinelibrary.wiley.com/doi/pdf/10.1029/2009GC002618>.
- Piaz GVD, Bistacchi A, and Massironi M. Geological outline of the Alps. *Episodes Journal of International Geoscience*, 26(3):175–180, 2003. doi: 10.18814/epiugs/2003/v26i3/004. Publisher: International Union of Geological Sciences.
- Pochon A, Poujol M, Gloaguen E, Branquet Y, Cagnard F, Gumiaux C, and Gapais D. U-Pb LA-ICP-MS dating of apatite in mafic rocks: Evidence for a major magmatic event at the

- Devonian-Carboniferous boundary in the Armorican Massif (France). *American Mineralogist*, 101(11):2430–2442, 2016. doi: 10.2138/am-2016-5736.
- Rainbird R, Cawood P, and Gehrels G. The Great Grenvillian Sedimentation Episode: Record of Supercontinent Rodinia’s assembly. In *Tectonics of Sedimentary Basins*, pages 583–601. John Wiley & Sons, Ltd, 2011. ISBN 978-1-4443-4716-6. doi: 10.1002/9781444347166.ch29. Section: 29 _eprint: <https://onlinelibrary.wiley.com/doi/pdf/10.1002/9781444347166.ch29>.
- Reed SJB. *Electron Microprobe Analysis and Scanning Electron Microscopy in Geology*. Cambridge University Press, 2005. ISBN 978-1-139-44638-9.
- Reiners P, Carlson R, Renne P, Cooper K, Granger D, McLean N, and Schoene B. U–Th–Pb geochronology and thermochronology. In *Geochronology and Thermochronology*, pages 171–230. John Wiley & Sons, Ltd, 2017. ISBN 978-1-118-45587-6. doi: 10.1002/9781118455876.ch8. Section: 8 _eprint: <https://onlinelibrary.wiley.com/doi/pdf/10.1002/9781118455876.ch8>.
- Ring U, Collins AS, and Kassem OK. U–Pb SHRIMP data on the crystallization age of the Gran Paradiso augengneiss, Italian Western Alps: Further evidence for Permian magmatic activity in the Alps during break-up of Pangea. *Eclogae Geologicae Helvetiae*, 98(3):363–370, 2005. doi: 10.1007/s00015-005-1170-9.
- Rosenbaum G and Lister GS. The Western Alps from the Jurassic to Oligocene: spatio-temporal constraints and evolutionary reconstructions. *Earth-Science Reviews*, 69(3):281–306, 2005. doi: 10.1016/j.earscirev.2004.10.001.
- Rubatto D. Zircon trace element geochemistry: partitioning with garnet and the link between U–Pb ages and metamorphism. *Chemical Geology*, 184(1):123–138, 2002. doi: 10.1016/S0009-2541(01)00355-2.
- Rubatto D. Zircon: The Metamorphic Mineral. *Reviews in Mineralogy and Geochemistry*, 83(1):261–295, 2017. doi: 10.2138/rmg.2017.83.9.
- Rubatto D and Gebauer D. Use of Cathodoluminescence for U–Pb Zircon Dating by Ion Microprobe: Some Examples from the Western Alps. In Pagel M, Barbin V, Blanc P, and Ohnenstetter D, editors, *Cathodoluminescence in Geosciences*, pages 373–400. Springer, Berlin, Heidelberg, 2000. ISBN 978-3-662-04086-7. doi: 10.1007/978-3-662-04086-7_15.
- Sandrone R, Cadoppi P, Sacchi R, and Vialon P. The Dora-Maira Massif. In von Raumer JF and Neubauer F, editors, *Pre-Mesozoic Geology in the Alps*, pages 317–325. Springer, Berlin, Heidelberg, 1993. ISBN 978-3-642-84640-3. doi: 10.1007/978-3-642-84640-3_18.
- Schaltegger U, Fanning CM, Günther D, Maurin JC, Schulmann K, and Gebauer D. Growth, annealing and recrystallization of zircon and preservation of monazite in high-grade metamorphism: conventional and in-situ U–Pb isotope, cathodoluminescence and microchemical evidence. *Contributions to Mineralogy and Petrology*, 134(2):186–201, 1999. doi: 10.1007/s004100050478.
- Scheiber T, Berndt J, Mezger K, and Pfiffner OA. Precambrian to Paleozoic zircon record in the Siviez-Mischabel basement (western Swiss Alps). *Swiss Journal of Geosciences*, 107(1): 49–64, 2014. doi: 10.1007/s00015-013-0156-2.
- Schmid SM, Fügenschuh B, Kissling E, and Schuster R. Tectonic map and overall architecture of the Alpine orogen. *Eclogae Geologicae Helvetiae*, 97(1):93–117, 2004. doi: 10.1007/s00015-004-1113-x.
- Schneider FM, Yuan X, Schurr B, Mechie J, Sippl C, Haberland C, Minaev V, Oimahmadov I, Gadoev M, Radjabov N, Abdybachaev U, Orunbaev S, and Negmatullaev S. Seismic imaging

- of subducting continental lower crust beneath the Pamir. *Earth and Planetary Science Letters*, 375:101–112, 2013. doi: 10.1016/j.epsl.2013.05.015.
- Sláma J and Košler J. Effects of sampling and mineral separation on accuracy of detrital zircon studies. *Geochemistry, Geophysics, Geosystems*, 13(5), 2012. doi: 10.1029/2012GC004106. _eprint: <https://onlinelibrary.wiley.com/doi/pdf/10.1029/2012GC004106>.
- Sláma J, Košler J, Condon DJ, Crowley JL, Gerdes A, Hanchar JM, Horstwood MSA, Morris GA, Nasdala L, Norberg N, Schaltegger U, Schoene B, Tubrett MN, and Whitehouse MJ. Plešovice zircon — A new natural reference material for U–Pb and Hf isotopic microanalysis. *Chemical Geology*, 249(1):1–35, 2008. doi: 10.1016/j.chemgeo.2007.11.005.
- Smith DC. Coesite in clinopyroxene in the Caledonides and its implications for geodynamics. *Nature*, 310(5979):641–644, 1984. doi: 10.1038/310641a0. Number: 5979 Publisher: Nature Publishing Group.
- Stephan T, Kroner U, and Romer RL. The pre-orogenic detrital zircon record of the Peri-Gondwanan crust. *Geological Magazine*, 156(2):281–307, 2019a. doi: 10.1017/S0016756818000031. Publisher: Cambridge University Press.
- Stephan T, Kroner U, Romer RL, and Rösel D. From a bipartite Gondwanan shelf to an arcuate Variscan belt: The early Paleozoic evolution of northern Peri-Gondwana. *Earth-Science Reviews*, 192:491–512, 2019b. doi: 10.1016/j.earscirev.2019.03.012.
- Tarquini S, Isola I, Favalli M, and Battastini A. TINITALY, a digital elevation model of Italy with a 10 meters cell size (Version 1.0) [Data set]. *Istituto Nazionale di Geofisica e Vulcanologia (INGV)*, 2007. doi: <https://doi.org/10.13127/tinitaly/1.0>.
- Teipel U, Eichhorn R, Loth G, Rohrmüller J, Höll R, and Kennedy A. U–Pb SHRIMP and Nd isotopic data from the western Bohemian Massif (Bayerischer Wald, Germany): Implications for Upper Vendian and Lower Ordovician magmatism. *International Journal of Earth Sciences*, 93(5):782–801, 2004. doi: 10.1007/s00531-004-0419-2.
- Tera F and Wasserburg GJ. U–Th–Pb systematics in three Apollo 14 basalts and the problem of initial Pb in lunar rocks. *Earth and Planetary Science Letters*, 14(3):281–304, 1972. doi: 10.1016/0012-821X(72)90128-8.
- Vermeesch P. On the visualisation of detrital age distributions. *Chemical Geology*, 312-313: 190–194, 2012. doi: 10.1016/j.chemgeo.2012.04.021.
- Vermeesch P. IsoplotR: A free and open toolbox for geochronology. *Geoscience Frontiers*, 9(5): 1479–1493, 2018. doi: 10.1016/j.gsf.2018.04.001.
- Vialon P. *Etude géologique du massif cristallin Dora-Maira : Alpes cottiennes internes : Italie*. phdthesis, Université de Grenoble, 1966.
- von Raumer J, Stampfli G, Borel G, and Bussy F. Organization of pre-Variscan basement areas at the north-Gondwanan margin. *International Journal of Earth Sciences*, 91(1):35–52, 2002. doi: 10.1007/s005310100200.
- von Raumer JF, Stampfli GM, and Bussy F. Gondwana-derived microcontinents — the constituents of the Variscan and Alpine collisional orogens. *Tectonophysics*, 365(1):7–22, 2003. doi: 10.1016/S0040-1951(03)00015-5.
- Wetherhill GW. Discordant uranium-lead ages, I. *Eos, Transactions American Geophysical Union*, 37(3):320–326, 1956. doi: 10.1029/TR037i003p00320. _eprint: <https://onlinelibrary.wiley.com/doi/pdf/10.1029/TR037i003p00320>.

- White WM. *Isotope Geochemistry*. John Wiley & Sons, Incorporated, Newark, UNITED STATES, 2015. ISBN 978-1-118-90211-0.
- Wiedenbeck M, Allé P, Corfu F, Griffin W, Meier M, Oberli F, Quadt AV, Roddick J, and Spiegel W. Three Natural Zircon Standards for U-Th-Pb, Lu-Hf, Trace Element and Ree Analyses. *Geostandards Newsletter*, 19(1):1–23, 1995. doi: 10.1111/j.1751-908X.1995.tb00147.x. eprint: <https://onlinelibrary.wiley.com/doi/pdf/10.1111/j.1751-908X.1995.tb00147.x>.
- Wiedenbeck M, Hanchar JM, Peck WH, Sylvester P, Valley J, Whitehouse M, Kronz A, Morishita Y, Nasdala L, Fiebig J, Franchi I, Girard JP, Greenwood R, Hinton R, Kita N, Mason P, Norman M, Ogasawara M, Piccoli P, Rhede D, Satoh H, Schulz-Dobrick B, Skår O, Spicuzza M, Terada K, Tindle A, Togashi S, Vennemann T, Xie Q, and Zheng YF. Further Characterisation of the 91500 Zircon Crystal. *Geostandards and Geoanalytical Research*, 28(1):9–39, 2004. doi: 10.1111/j.1751-908X.2004.tb01041.x. eprint: <https://onlinelibrary.wiley.com/doi/pdf/10.1111/j.1751-908X.2004.tb01041.x>.
- Wu Y and Zheng Y. Genesis of zircon and its constraints on interpretation of U-Pb age. *Chinese Science Bulletin*, 49(15):1554–1569, 2004. doi: 10.1007/BF03184122.
- Zheng D, Wu S, Ma C, Xiang L, Hou L, Chen A, and Hou M. Zircon classification from cathodoluminescence images using deep learning. *Geoscience Frontiers*, 13(6):101436, 2022. doi: 10.1016/j.gsf.2022.101436.
- Zurbruggen R. Ordovician orogeny in the Alps: a reappraisal. *International Journal of Earth Sciences*, 104(2):335–350, 2015. doi: 10.1007/s00531-014-1090-x.

Appendix A: Sample preparation

Table A1: The revolutions per minute (rpm) and time for milling for the XRF sample preparation.

Sample	rpm	Time (s)
CH2249	800	40
CH2240	800	40+25
CH2231	800	40+15
CH2232	800	40+10
CH2233	800	40+15
GM213	800	40+40
GM214	800	30

Table A2: The revolutions per minute (rpm) and time for milling for sample preparation for zircon extraction. Each time slot represents one round of milling for a small amount of sample.

Sample	rpm	Time (s)		
CH2249	700	30+30		
		30+10		
		40		
		40		
		40+5		
		40		
		40		
		40		
		45		
		35+5		
		40		
		CH2240	700	30
				25
25				
20				
25				
30				
25				
25				
20				
25				
15				
CH2241	700			35
		35		
		35		
		35		
		35		
		35		
		35		
		35		
		35		
		35		
		35		
		35		
GM213	700	20		
		25		
		25		
		25		
		20		
		25		
GM214	700	20+10		
		30		
		30		
		30		
		25		

Table A3: The settings and fractions used for the zircon separation. The speed refers to the intensity of the shaking of the Wilfley table.

Sample	CH2241
Speed	80%
Fractions:	"Zircon" "1" "2+3" "4+5+6+7"
Sample	CH2240
Speed	80%
Fractions:	"Zircon" "1" "2+3+4" "4+5+6"
Sample	CH2249
Speed	60%
Fractions:	"Zircon" "1" "2+3+4" "5+6+7"
Sample	GM213
Speed	80%
Fractions:	"Zircon" "Gr/Ap" "1" "2+3+4" "5+6+7"
Sample	GM214
Speed	80%
Fractions:	"Zircon" "Ep" "1" "2+3+4+5+6+7"

Table A4: The paste and force used during the polishing of the zircon mounts. Each mount was polished in stages, a little at a time to expose the middle section of zircon. The polishing was conducted at the Natural History Museum in Stockholm.

Mount 1 CH2241/CH2249		
Paste	Force (N)	Time (s)
3 μm	5	60
		30
		30
		30
		60
		45
		30
		30
		30
		30
1 μm	5	30
Mount 2 CH2240/CH2243		
Paste	Force (N)	Time (s)
3 μm	5	60
		30
		30
		10
		30
1 μm	5	30
Mount 3 GM2103/GM2104		
Paste	Force (N)	Time (s)
3 μm	5	60
		30
		30
		30
		30
		30
		30
		45
1 μm	5	30

Table A5: The amount of flux (g) and sample (g) (5:2 ratio) used for the fusion of each sample, in preparation for the XRF analysis.

Crucible	Sample	Flux (g)	Sample (g)
1064	CH2231	4.9999	2.00009
1067	CH2232	5.00002	1.99998
1069	CH2233	5.00003	1.99998
2278	CH2240	5.00008	2.00004
2277	GM213	4.99998	2.00004
1070	GM214	4.99993	2.00005
1063	CH2249	5.00008	2.00002

Appendix B: Petrographic descriptions

GM212

Rock type: g-micaschist

Macroscopic aspect

The hand sample is brown-greyish, fine- to medium-grained and strongly crenulated.

Deformation

At the micro-scale, a main foliation is defined by the shape-preferred orientation of white mica. It is strongly folded (Fig. B1a).

Mineral composition

The main minerals are white mica (40%), quartz (30%), garnet (10%) and chlorite (10%) with accessory phases rutile (< 5%), titanite (< 5%), plagioclase (< 5%) and opaques (< 5%).

Timing of mineral growth with respect to deformation

The main foliation is strongly crenulated and defined by the shape-preferred orientation of white mica. The core of the fold hinge is filled with quartz. Garnet porphyroblasts are subhedral and wrapped by the main foliation. They contain inclusions of opaques, quartz and rutile. The inclusions do not mark an internal fabric but in the rim they are concentric.

Lozenge-shaped pseudomorphs (interpreted to be after glaucophane) are concentrated in the strongly crenulated areas parallel to the crenulation cleavage and consist of a fine-grained aggregate of chlorite, albite and quartz (Fig. B1b). Titanite is dispersed in the matrix as anhedral crystals. Plagioclase porphyroclasts are dispersed in the matrix and are partially replaced by opaques and white mica. Plagioclase is wrapped by the main foliation.

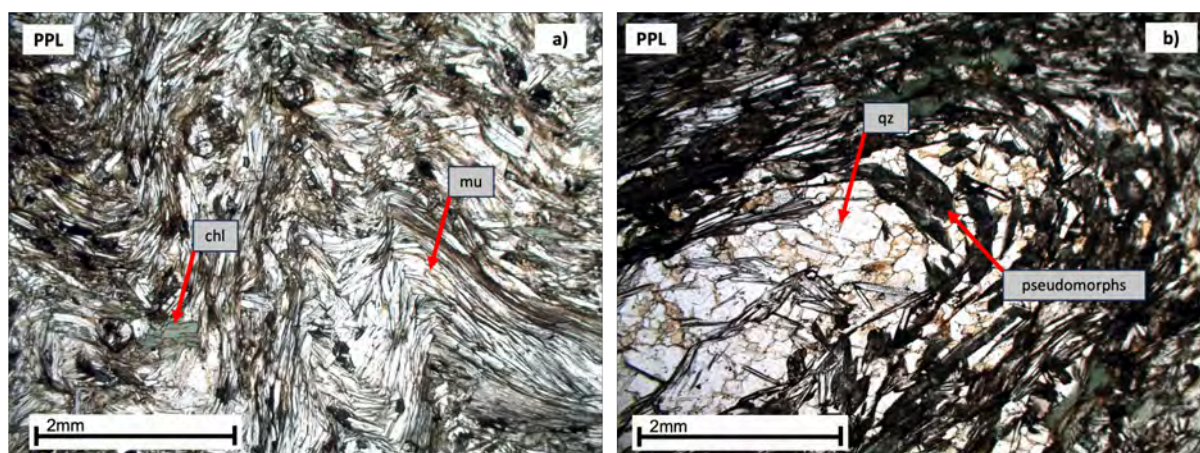


Figure B1: a) Main foliation is folded, which is clearly displayed by the orientation of white mica. b) Lozenge-shaped pseudomorphs of glaucophane are mainly concentrated in the fold hinges. Note that the thin section is thick, up to 40 μ m.

GM215**Rock type: Graphitic micaschist***Macroscopic aspect*

The hand sample is grey to dark grey, fine-grained and strongly foliated. The foliation is defined by alternating layers of quartz and graphite.

Deformation

At the micro-scale, a strong main foliation is defined by interlayering of quartz and graphite (Fig. B2a). The main foliation is folded.

Mineral composition

The main minerals are quartz (40%), graphite (40%), white mica (20%) and garnet (5%) with accessory phases chlorite (< 5%), epidote (< 5%) and plagioclase (< 5%).

Timing of mineral growth with respect to deformation:

The main foliation is defined by interlayering of quartz and graphite. Graphite is abundant and occurs as smeared layers with no clear grain boundary. It tends to occur in layers which are rich in white mica. The graphitic layers are weakly folded. White mica is partially recrystallised along its edges into fine-grained aggregates.

Garnet porphyroblasts are dispersed in the matrix and are up to 100 μm in size and subhedral. Garnet contains abundant inclusions, which are difficult to identify due to their small size. However, garnet contains inclusions of graphite (Fig. B2b). Plagioclase porphyroclasts are dispersed in the matrix and are heavily retrograded. They tend to occur in close association with the graphite and white mica-rich layers. Lozenge-shaped pseudomorphs (interpreted to be after glaucophane) are elongated along the main foliation and consist of a fine-grained aggregate of quartz and plagioclase.

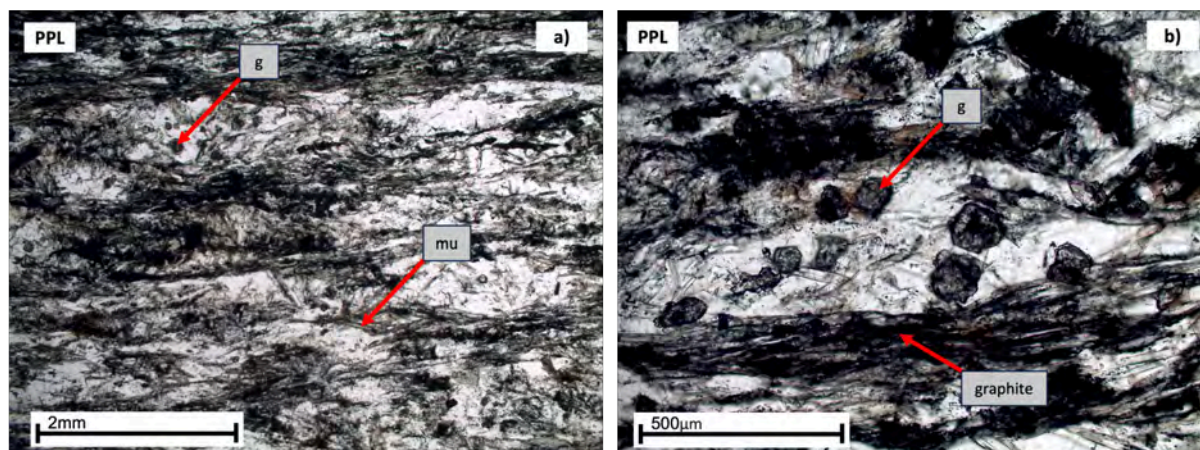


Figure B2: (a) Main foliation defined by smeared layers of graphite. (b) Garnet contains inclusions of graphite.

GM1406A-B

Rock type: g-micaschist

Macroscopic aspect

The samples are grey in colour and fine-grained. Sample 1406A displays a foliation whereas 1406B has less apparent foliation but displays folding.

Deformation

At the micro-scale, a main foliation is defined by the shape-preferred orientation of white mica. The foliation is strongly folded in sample 1406B (B3a) whereas the foliation is planar in sample 1406A. The foliation wraps the garnet porphyroblasts.

Mineral composition

The main minerals are quartz (30%), white mica (30%), plagioclase (20%), chlorite (10%) and garnet (5%) with accessory phases calcite (< 5%), biotite (< 5%), tourmaline (< 5%) and epidote (< 5%).

Timing of mineral growth with respect to deformation

The main foliation is defined by the shape-preferred orientation of white mica. Additionally, alternating layers of plagioclase and quartz are visible. White mica tends to occur in the plagioclase-rich layers. Garnet porphyroblasts are subhedral, up to 100 μm in size and wrapped by the main foliation. They contain inclusions of quartz, opaques and rutile. In the rim, the inclusions mark an internal fabric which is oriented parallel to the main foliation (Fig. B3b). Along the edges, garnet is partially replaced by opaques, quartz and white mica. The strain shadows mainly consist of quartz.

Plagioclase porphyroclasts are dispersed in the matrix and anhedral. They contain inclusions of white mica, biotite and quartz. The inclusions mark an internal fabric which is oriented parallel to the main foliation. Biotite and chlorite occur in the matrix and follow the main foliation, and biotite is almost fully chloritized. Epidote tends to occur in association with opaques and occur as anhedral grains. Calcite is anhedral and partially replaced by chlorite and plagioclase. Tourmaline is zoned with a green core and brown rim.

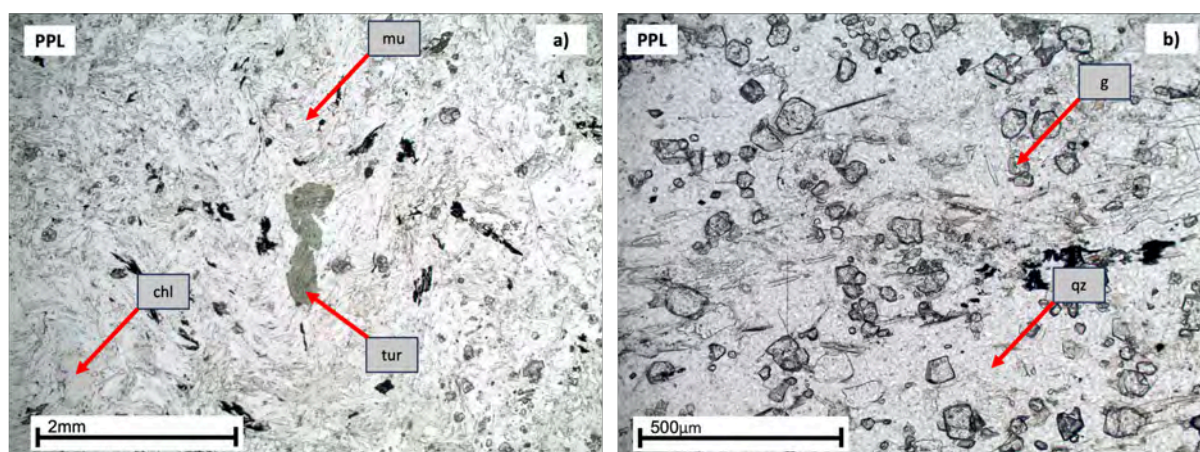


Figure B3: a) In sample 1406B, the foliation is strongly folded. b) Garnet porphyroblasts, up to 100 μm , are abundant in the matrix.

GM1920**Rock type: Graphitic paragneiss***Macroscopic aspect*

The hand sample is dark grey, very fine-grained and weakly foliated.

Deformation

At the micro-scale, a weak main foliation is defined by alternating layers of graphite and quartz (Fig. B4a). A weak second foliation is defined by the shape-preferred orientation of white mica which cross-cuts the main foliation.

Mineral composition

The main minerals are quartz (40%), graphite (30%) and white mica (20%) with accessory phases garnet (< 5%), chlorite (< 5%), rutile (< 5%), clino/zoisite (< 5%) and plagioclase (< 5%).

Timing of mineral growth with respect to deformation

The main foliation is defined by the interlayering of discontinuous graphite-rich layers and quartz-rich layers. Graphite occur as smeared anhedral fine-grained crystals. Garnet porphyroblasts are up to 100 μm , subhedral and wrapped by the main foliation. They contain inclusions of graphite and rutile. The inclusions mark an internal fabric which is sub-parallel to parallel to the main foliation (Fig. B4b).

Elongated, idioblastic clino/zoisite crystals are dispersed in the matrix and occur at an angle to the main foliation. Brown mica is dispersed in the matrix and occur as anhedral crystals. Occasionally, it shows an idioblastic shape and occurs at an angle to the main foliation. Plagioclase porphyroclasts are elongated and occur parallel to the main foliation. They are partially replaced by graphite, quartz and white mica.

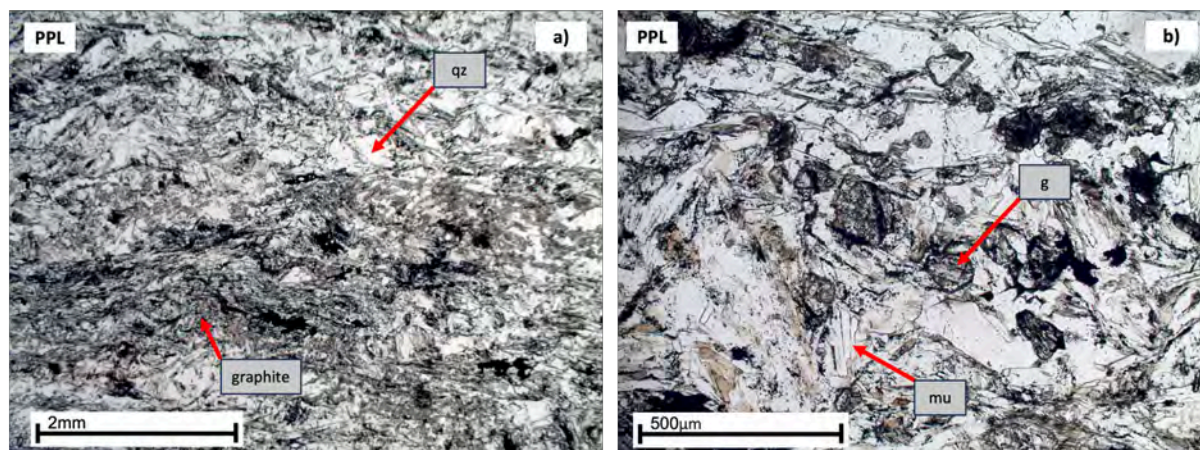


Figure B4: a) The foliation is poorly-defined and is displayed by interlayering of quartz and graphite. b) Garnet porphyroblasts are small, but contain abundant graphite inclusions which are sub-parallel to parallel to the main foliation.

GM1908

Rock type: Graphitic paragneiss*Macroscopic aspect*

The hand sample is very fine-grained, grey and shows moderate foliation. A slightly folding of the foliation is barely visible in hand specimen.

Deformation

At the micro-scale a main foliation is defined by quartz-layers and the shape-preferred orientation of white mica (Fig. B5a). The foliation is folded.

Mineral composition

The main minerals are quartz (45%), white mica (20%), plagioclase (10%), graphite (10%) and chlorite (10%) with accessory phases garnet (< 5%), biotite (< 5%) and opaques (< 5%).

Timing of mineral growth with respect to deformation

The main foliation is defined by alternating quartz layers and the shape-preferred orientation of white mica. It can be more or less developed in different domains, depending on the abundance of mica in the domain. Graphite occurs as anhedral, sub-rounded crystals aligned with the main foliation. Where the foliation is better-developed, graphite becomes more fine-grained and loses its' round shape. Plagioclase occurs as anhedral clasts in the matrix and is slightly elongated parallel to the main foliation. They contain inclusions of garnet, white mica, graphite, opaques and quartz. The inclusions mark an internal fabric which is parallel to the main foliation.

Garnet porphyroblasts are small, up to 100 μm , subhedral and wrapped by the main foliation. They contain inclusions of graphite which do not form an internal fabric (Fig. B5b). Garnet is altered along the edges into a brown-yellow alteration product, too fine-grained to be identified at the optical microscope. Biotite is dispersed in the matrix and is partially chloritized.

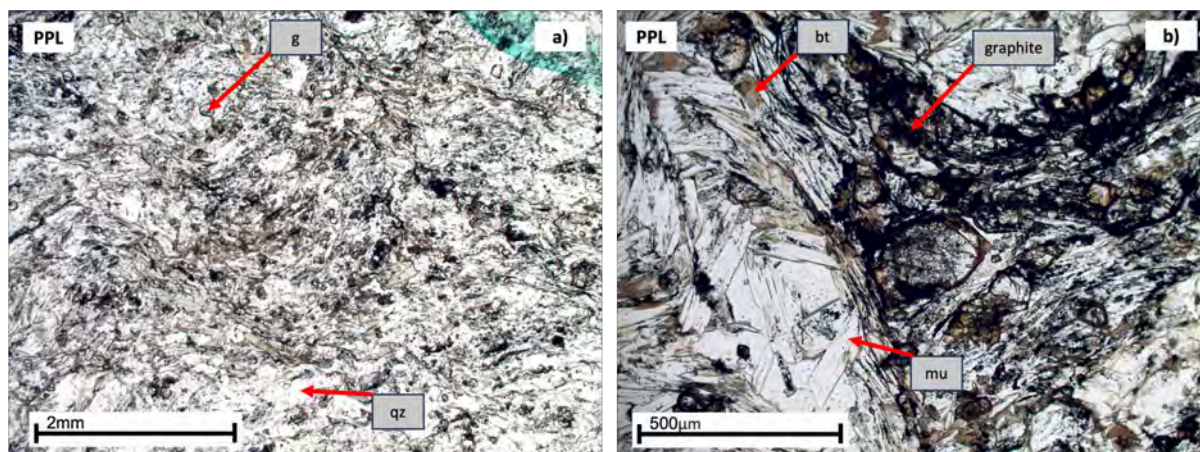


Figure B5: a) The main foliation is folded. b) Garnet contains abundant, randomly oriented graphite inclusions.

GM2157**Rock type: Paragneiss***Macroscopic aspect*

The hand sample dark grey and medium grained. It displays a weak foliation, which is slightly folded.

Deformation

At the micro-scale, the weak foliation is defined by the shape-preferred orientation of white mica (Fig. B6a). The foliation is weakly folded.

Mineral composition

The main minerals are quartz (40%), plagioclase (30%), chlorite (15%), garnet (10%) and white mica (5%) with and an accessory phase; titanite (< 5%).

Timing of mineral growth with respect to deformation

The main foliation is weakly defined by the shape-preferred orientation of white mica. Plagioclase occurs as sub- to anhedral crystals in the matrix. They contain inclusions of garnet, quartz and white mica. The inclusions do not mark an internal fabric. Plagioclase is partially replaced by chlorite.

Garnet porphyroblasts are small (up to 100 μm) and subhedral. They contain inclusions of quartz, titanite and white mica. Garnet appears cloudy, likely due to the abundance of small inclusions. There is an optical discontinuity between core and rim of garnet, that separates a pink core and a paler rim, which could indicate that there are two generations of growth (Fig. B6b). Elongated pseudomorphs (interpreted to be after glaucophane) are dispersed in the matrix and consist of a fine-grained aggregate of chlorite, quartz and albite. Biotite is dispersed in the matrix and partially chloritized. Plagioclase is partially replaced by chlorite along the edges.

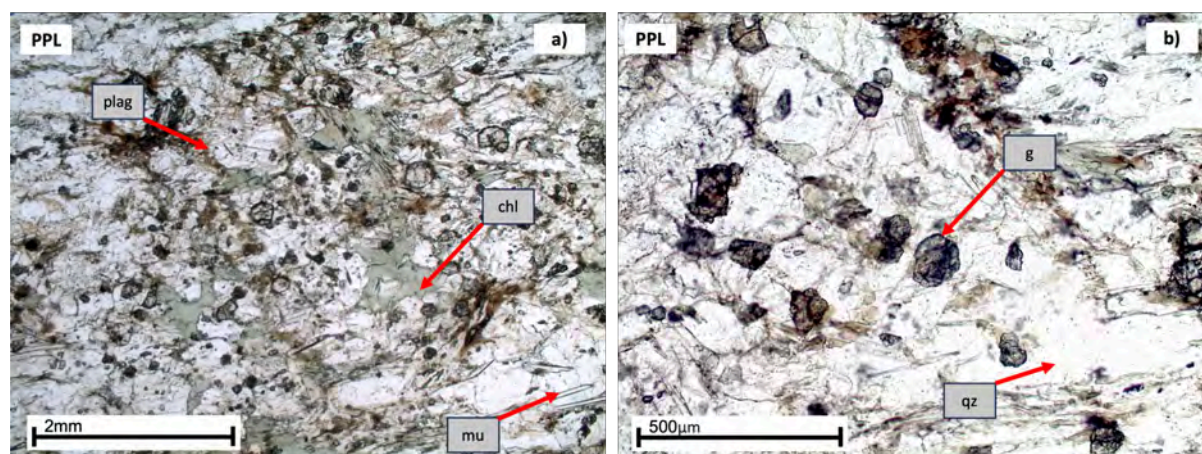


Figure B6: a) The main foliation is weakly defined by shape-preferred orientation of white mica. b) Garnet displays a pink core with a paler rim.

GM2035**Rock type: Paragneiss***Macroscopic aspect*

The sample is medium-grained and vary from grey to light grey. In hand sample is shows interlayering of light, felsic layers (quartz and plagioclase) and darker, mafic layers (chlorite).

Deformation

At the micro-scale, a main foliation is defined by alternating layers of quartz and plagioclase which contain varying amounts of white mica (Fig. B7a). The bands are gently folded.

Mineral composition

The main minerals are quartz (40%), white mica (30%), chlorite (15%), garnet (5%) and plagioclase (5%) with accessory phases titanite (< 5%), tourmaline (< 5%), rutile (< 5%), graphite (< 5%), epidote (< 5%) and opaques (< 5%).

Timing of mineral growth with respect to deformation

The main foliation is defined by alternating bands of quartz and plagioclase-rich layers. Garnet porphyroblasts are up to 400 μm in size, subhedral and wrapped by he main foliation. They contain inclusions of white mica and rutile. The inclusions mark an internal fabric which is sub-parallel to the main foliation and are concentric at the garnet rim (Fig. B7b). Garnets are locally fractured and replaced by chlorite, biotite and quartz along the fractures.

Plagioclase occurs in layers defining the main foliation and is anhedral. It contains inclusions of opaques, epidote, white mica and garnet. The inclusions mark an internal fabric which is oriented parallel to the main foliation. Plagioclase is partially replaced by quartz and white mica. Titanite is dispersed in the matrix and strongly altered. Biotite occurs as elongated crystals and is almost fully chloritized. Zoned tourmaline are dispersed in the matrix.

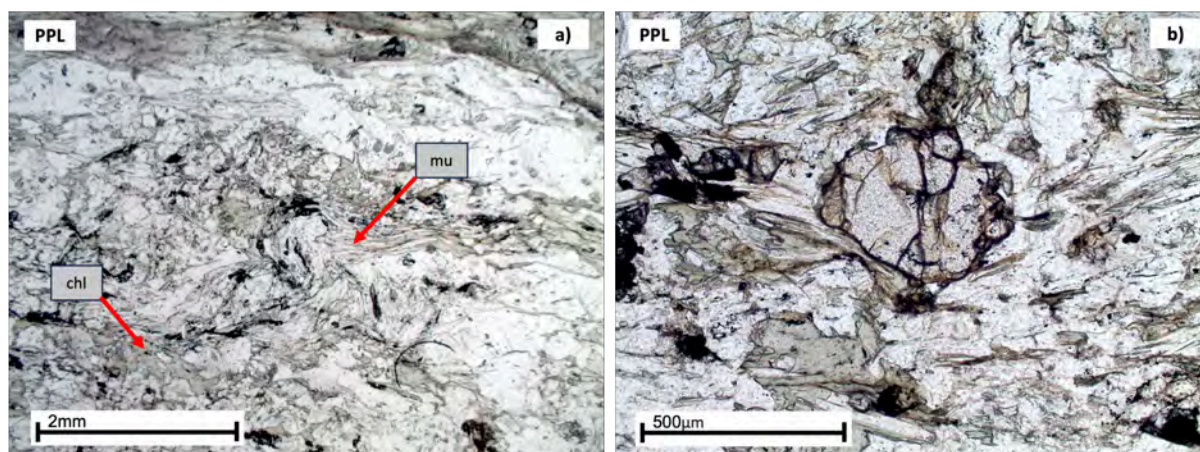


Figure B7: a) The main foliation is weakly folded and defined by the interlayering of quartz and plagioclase. b) Garnet contains inclusions with are parallel to the main foliation.

GM2158A-E**Rock type: ab-g paragneiss**

Macroscopic aspect The hand samples are grey and fine- to medium-grained. The fine-grained matrix contains large garnet porphyroblasts, up to 0.5 cm in size. The sample displays a strong foliation which wraps the garnet porphyroblasts.

Deformation

At the micro-scale, a main foliation is defined by the shape-preferred orientation of white mica and chlorite as well as quartz-rich layers (Fig. B8a). The garnet porphyroblasts are wrapped by the main foliation. The foliation is weakly folded.

Mineral composition

The main minerals are white mica (30%), plagioclase (20%), chlorite (10%), quartz (10%), garnet (10%), clino/zoisite (10%) and titanite (5%) with accessory phases rutile (< 5%) and ilmenite (< 5%).

Timing of mineral growth with respect to deformation

The main foliation is defined by the shape-preferred orientation of white mica and chlorite. Deformed plagioclase is abundant in the matrix, and it is subhedral and up to 1mm in size. Plagioclase contain inclusions of white mica, titanite and clino/zoisite. The inclusions define an internal fabric, which is parallel to the main foliation.

Garnet porphyroblasts are large, up to 0.5 cm, idioblastic and wrapped by the main foliation. They contain inclusions of quartz, white mica, opaques, rutile and ilmenite. There are two different types of garnet, one which is more skeletal with abundant quartz inclusions and one which is more pristine (Fig. B8b). Skeletal garnet tend to have inclusions of rutile concentrated in the core whereas ilmenite is concentrated in the rim. Pristine garnet has smaller inclusions which tend to concentrate in the core. Garnet is locally fractured and altered to chlorite along the fractures. At the rim, garnet is partially replaced by fine-grained aggregates of micas and chlorite. The strain shadow mainly consist of quartz, white mica and chlorite. There is an abundance of clino/zoisite in dispersed in the matrix, which occur as elongated crystals oriented parallel to the main foliation. Rutile is dispersed in the matrix and has a corona of titanite.

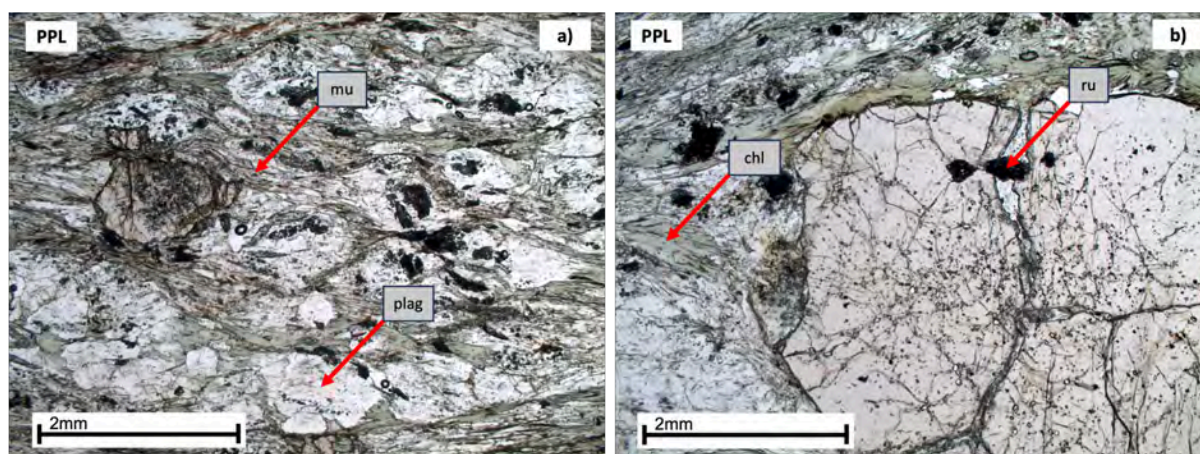


Figure B8: a The main foliation wraps around garnet and plagioclase. b) Garnets are large, up to 0.5cm, and contain rutile inclusions in the rim.

GM2158A1-21581B**Rock type: ab-g paragneiss***Macroscopic aspect*

The hand samples are grey and medium-grained. Sample GM2158A1 contains large garnet porphyroblasts (up to 0.4 cm) whereas sample GM21581B contains smaller garnets (up to 1mm). It displays a foliation which wraps the garnet porphyroblasts.

Deformation

At the micro-scale, a strong main foliation is defined by shape-preferred orientation of white mica and chlorite (Fig. B9a). The foliation is weakly folded and wraps the garnet porphyroblasts.

Mineral composition

The main minerals are quartz (20%), white mica (20%), plagioclase (20%), garnet (10%), chlorite (10%) and clino/zoisite (5%) with accessory phases titanite (< 5%) and rutile (< 5%).

Timing of mineral growth with respect to deformation

The main foliation is defined by the shape-preferred orientation of white mica and chlorite. White mica occurs as elongated crystals or as fine-grained aggregates which are wrapped by the main foliation (pseudomorphs of lawsonite?). Sample GM21581B has slightly smaller white mica in the matrix compared to sample GM2158A. Plagioclase occurs as deformed, subhedral crystals oriented parallel to the main foliation. Plagioclase contain inclusions of titanite, rutile and clino/zoisite. Rutile tends to concentrate in the rim and is partially replaced by titanite. The inclusions mark an internal fabric, which is parallel to the main foliation.

Garnet porphyroblasts are up to 0.5 cm in size and idioblastic. They contain abundant inclusions of quartz, white mica, rutile and titanite (Fig. B9b). Rutile tends to concentrate in the core whereas titanite tends to concentrate in the rim of garnet. The inclusions do not mark an internal fabric. Rutile is dispersed in the matrix and is partially replaced by titanite.

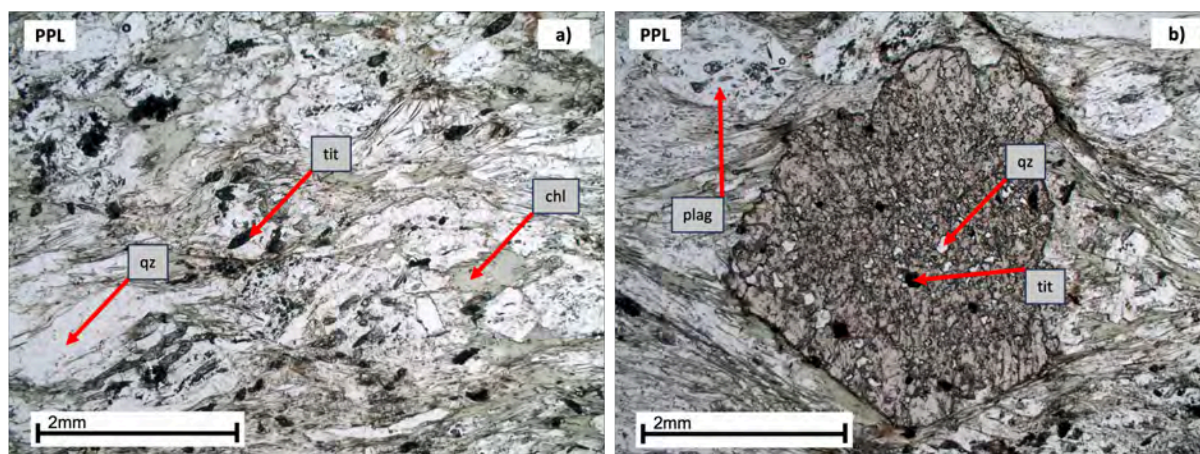


Figure B9: a) The main foliation is slightly folded. b) Garnet contains abundant inclusions of quartz and titanite.

GM2159A-C**Rock type: ab-g paragneiss***Macroscopic aspect*

The hand samples are grey and fine- to medium-grained. The samples contain large garnet porphyroblasts (up to 0.5cm). Both samples display a strong foliation.

Deformation

At the micro-scale, a strong main foliation is defined by the shape-preferred orientation of mica and chlorite (Fig. B10a). Garnet porphyroblasts are wrapped by the main foliation.

Mineral composition

The main minerals are plagioclase (35%), chlorite (15%), biotite (10%), garnet (10%), quartz (10%), white mica (5%) and clino/zoisite (5%) with an accessory phase rutile (< 5%) and epidote (< 5%).

Timing of mineral growth with respect to deformation

The main foliation is defined by the shape-preferred orientation of chlorite, white mica and biotite. A banding is defined by alternating layers of fine-grained biotite and plagioclase. Biotite layers are strongly altered and display varying degrees of chloritization.

Garnet porphyroblasts are large, up to 0.5 cm, subhedral and wrapped by the main foliation. They contain inclusions of quartz, rutile and opaques (Fig. B10b). The inclusions do not mark an internal fabric. Garnet crystals are locally fractured and partially replaced by chlorite and biotite along the fractures. There is abundant epidote and clino/zoisite dispersed in the matrix which occurs as elongated crystals oriented parallel to the main foliation. Epidote is partially replaced by chlorite.

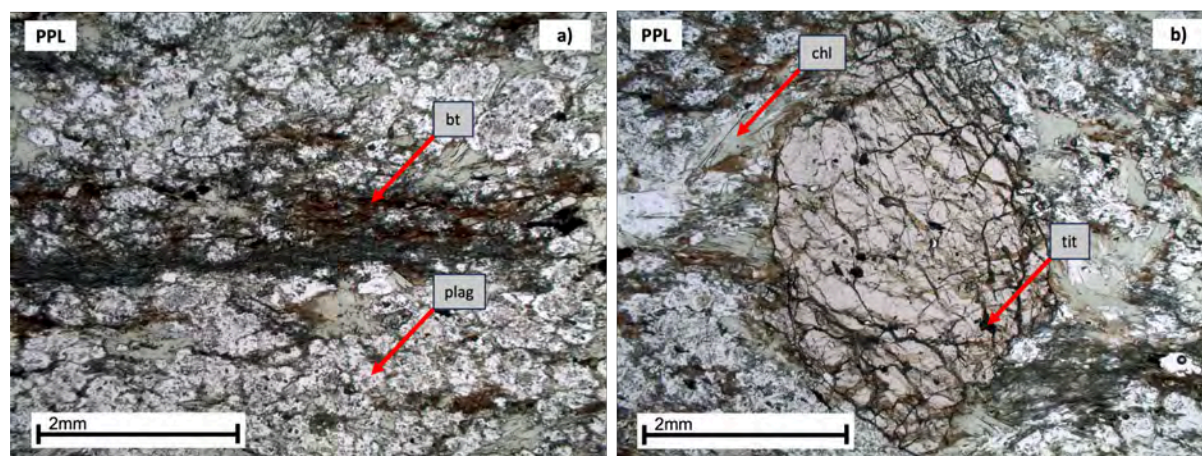


Figure B10: a) The main foliation is defined by the shape-preferred orientation of the micas. b) Garnet porphyroblasts are wrapped by the main foliation and contain inclusions of titanite.

GM2149**Rock type: Augengneiss***Macroscopic aspect*

The hand sample is creamy white to grey and medium-grained. It displays a foliation defined by fine-grained layers which are gently folded. There are large feldspar porphyroclasts, up to 3 mm, which are clearly visible on hand sample scale.

Deformation

At the micro-scale a strong main foliation is defined by quartz banding and the shape-preferred orientation of white mica (Fig. B11a). There is interlayering with mica and graphite. The feldspar porphyroclasts are wrapped by the main foliation.

Mineral composition

The main minerals are quartz (50%), albite (20%), white mica (15%), microcline (10%) and graphite (10%) with an accessory phase epidote (< 5%).

Timing of mineral growth with respect to deformation

The main foliation is defined by quartz which occurs as banding and by the shape-preferred orientation of white mica. Quartz displays a large variation in grain size. Albite porphyroclasts (up to 1 mm) are dispersed in the matrix and deformed. They are wrapped by white mica and graphite.

The larger feldspar porphyroclasts mainly consist of microcline and are large (up to 3 mm). They contain inclusions of opaques, epidote and white mica (Fig. B11b). The inclusions do mark an internal fabric, which is sub-parallel to the main foliation. Microcline and albite are strongly sericitized along the edges, but the albite tends to be less altered than microcline. White mica occurs as elongated crystals in the matrix but tend to be larger and idioblastic in close association to the feldspars.

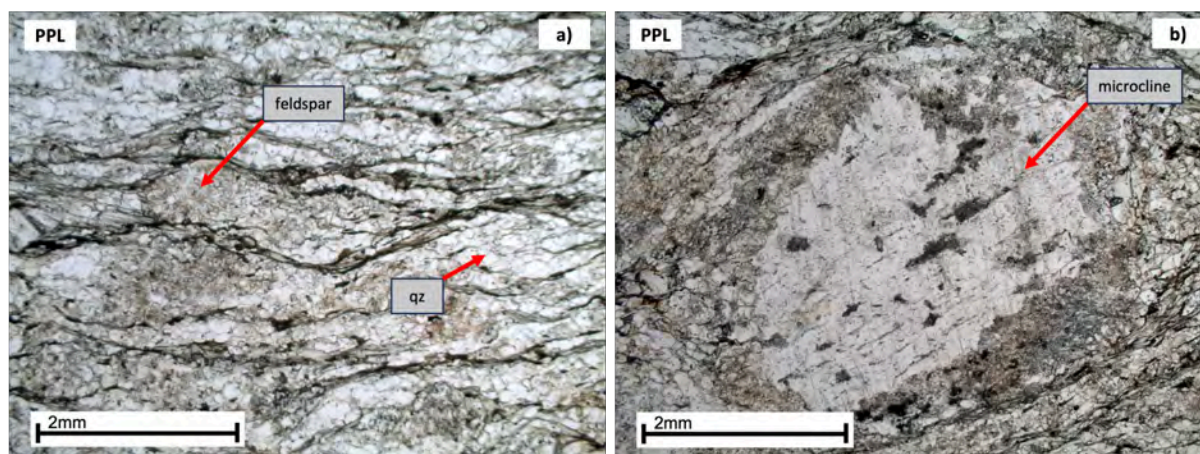


Figure B11: a) The main foliation is defined by quartz banding and wraps the feldspar porphyroclasts. b) Feldspar contains inclusions which are sub-parallel to the main foliation.

GM2034**Rock type: Augengneiss***Macroscopic aspect*

The sample is medium-grained and vary from light grey to white. It displays a foliation. It has a large feldspar porphyroclast (1 cm) which is wrapped by the foliation.

Deformation

At the micro-scale, a main foliation is defined by bands of quartz (Fig. B12a). The feldspar porphyroclast is wrapped by the foliation.

Mineral composition

The main minerals are quartz (40%), albite (30%), white mica (15%) and microcline (10%) with accessory phases biotite (< 5%) and graphite (< 5%).

Timing of mineral growth with respect to deformation

The main foliation is defined by quartz and feldspar banding. White mica is elongated and contains inclusions of biotite. Dispersed in the matrix, there are smaller albite porphyroclasts which define the feldspar-rich bands. These contain abundant inclusions of white mica and quartz. The inclusions do not mark an internal fabric. The large feldspar porphyroclast (1 cm in size) is wrapped by the foliation and likely represents an original magmatic K-feldspar site. The porphyroclast is now consisting of microcline with tartan twinning. Perthites in the original magmatic feldspar are still observable as the original plagioclase now consists of strongly sericitized albite (Fig. B12b). Inclusions of white mica are present in microcline and do not mark an internal foliation at the core, but are sub-parallel to the main foliation at the rim. Microcline displays tartan twinning along with a perthitic texture. The strain shadow mainly consist of quartz and white mica. Along the edges of microcline, there are inclusion-rich albite which are mm-sized.

Chlorite is dispersed in the matrix as elongated, anhedral crystals parallel to the main foliation. Fine-grained biotite occurs parallel to the main foliation and is partially chloritized.

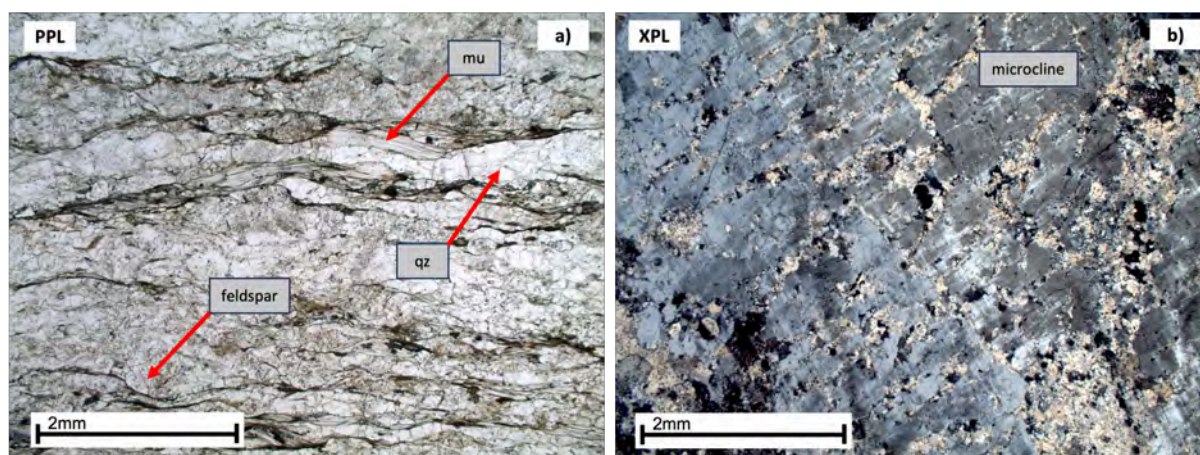


Figure B12: a) The main foliation wraps around the feldspar porphyroclasts and is defined by alternating quartz layers. b) Microcline shows tartan twinning and is strongly sericitized.

GM2036**Rock type: Augengneiss***Macroscopic aspect*

Hand sample is missing.

Deformation

At the micro-scale, a main foliation is defined by quartz-rich layers and the shape-preferred orientation of white mica (Fig. B13a). The main foliation wraps around feldspar porphyroclasts.

Mineral composition

The main minerals are quartz (40%), albite (30%) and white mica (20%) with accessory phases biotite (< 5%), titanite (< 5%), epidote (< 5%), microcline (< 5%), chlorite (< 5%) and opaques (< 5%).

Timing of mineral growth with respect to deformation

The main foliation is defined by the shape-preferred orientation of white mica and the alternation of quartz-rich layers. Albite is the most abundant feldspar but there are minor amounts of microcline. Albite forms porphyroblasts up to 3 mm in size, which are sub- to anhedral and wrapped by the main foliation. Albite sometimes displays polysynthetic twinning and a perthitic texture. It has inclusions of white mica, opaques and quartz (Fig. B13b). The inclusions mark an internal fabric which is sub-parallel to the main foliation. Smaller grains of microcline and albite are dispersed in the matrix and follow the main foliation. Albite is partially altered to microcline along the edges of the grain. The strain shadow mainly consists of quartz.

The albite is partially replaced by white mica along the edges. Chlorite is dispersed in the matrix as elongated or anhedral crystals which contain inclusions of white mica. Anhedral titanite is dispersed in the matrix, which contains inclusions of rutile. These tend to occur in close association with epidote.

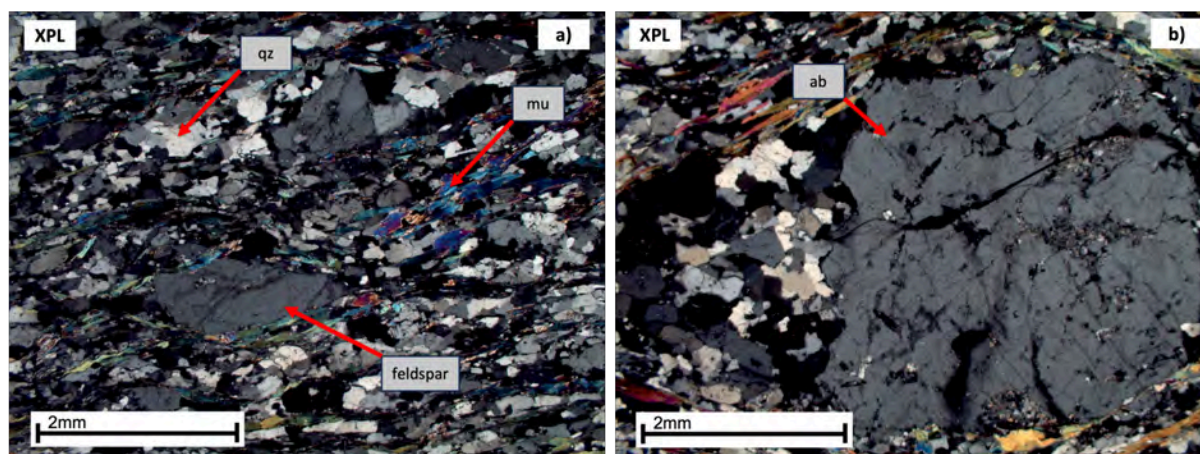


Figure B13: a) The main foliation wraps around the feldspar porphyroblasts. b) Inclusions in feldspar are oriented sub-parallel to the main foliation.

Appendix C: Bulk rock chemistry

Table C1: The values obtained during loss on ignition (LOI).

Sample nr	Crucible (g)	Sample + crucible (g)	After oven (g)	After oven (cool)
CH2231	28.75389	38.76036	38.5315	38.53618
CH2232	30.46896	40.59625	40.3697	40.37549
CH2233	24.54822	34.67595	34.4596	34.46518
CH2240	25.26763	35.30803	35.1832	35.18871
CH2249	25.60668	35.64676	35.56402	35.56807
GM213	24.07456	34.10672	33.77772	33.7865
GM214	24.31202	34.36695	34.12231	34.14044

Sample nr	Sample start (g)	Sample after oven (g)	H ₂ O (g)	LOI (%)
CH2231	10.00647	9.77761	0.22886	2.287120233
CH2232	10.12729	9.90074	0.22655	2.23702491
CH2233	10.12773	9.91138	0.21635	2.136214137
CH2240	10.0404	9.91557	0.12483	1.24327716
CH2249	10.04008	9.95734	0.08274	0.824097019
GM213	10.03216	9.70316	0.329	3.279453278
GM214	10.05493	9.81029	0.24464	2.433035337

Appendix D: U-Pb geochronology

Table D1: The operating conditions for the LA-ICP-MS during U-Pb dating on zircon.

Laboratory name	GeOHeLiS Analytical Platform, OSUR, Univ Rennes, France
Sample type/mineral	Zircon
Sample preparation	Conventional mineral separation, 1-inch resin mount, 1 μm polish to finish
Imaging	XL30 ESEM-FEG equipped with a Centaurus detector
Laser ablation system	
Make, Model & type	ESI NWR193UC, Excimer
Ablation cell	ESI NWR TwoVol2
Laser wavelength	193 nm
Pulse width	<5 ns
Fluence	6.6 J/cm ²
Repetition rate	4 Hz
Spot size	25 μm
Sampling mode / pattern	Single spot
Carrier gas	100% He, Ar make-up gas and N ₂ (3 ml/mn) combined using in-house smoothing device
Background collection	20 seconds
Ablation duration	40 seconds
Wash-out delay	15 seconds
Cell carrier gas flow (He)	0.76 l/min
ICP-MS Instrument	
Make, Model & type	Agilent 7700x, Q-ICP-MS
Sample introduction	Via conventional tubing
RF power	1350 W
Sampler, skimmer cones	Ni
Extraction lenses	X type
Make-up gas flow (Ar)	0.67 l/min
Detection system	Single collector secondary electron multiplier
Data acquisition protocol	Time-resolved analysis
Scanning mode	Peak hopping, one point per peak
Detector mode	Pulse counting, dead time correction applied, and analog mode when signal intensity $>\approx 106$ cps
Masses measured	²⁰⁴ (Hg + Pb), ²⁰⁶ Pb, ²⁰⁷ Pb, ²⁰⁸ Pb, ²³² Th, ²³⁸ U
Integration time per peak	10-30 ms (²⁰⁷ Pb)
Sensitivity / Efficiency	21000 cps/ppm Pb (50 μm , 10 Hz)
Data Processing	
Gas blank	20 seconds on-peak
Calibration strategy	GJ1 zircon standard used as primary reference material, Plešovice used as secondary reference material (quality control)
Common-Pb correction, composition and uncertainty	No common-Pb correction.
Reference Material info	GJ1 (Jackson et al., 2004), Plešovice (Sláma et al., 2008)
Data processing package	Iolite 4 (Paton et al., 2010)
Uncertainty level and propagation	Ages are quoted at 2 σ absolute, propagation is by quadratic addition according to Horstwood et al. (2016). Reproducibility and age uncertainty of reference material are propagated.
Quality control / Validation	Plešovice: concordia age = 336.8 +/- 1.1 Ma (N=48; MSWD=0.74)

Table D2: The operating conditions for the LA-ICP-MS during trace element analysis of zircon.

Laboratory name	GeOHeLiS Analytical Platform, OSUR, Univ Rennes 1, France
Sample type/mineral	Zircon
Sample preparation	Conventional mineral separation, 1-inch resin mount, 1 μm polish to finish
Laser ablation system	
Make, Model & type	ESI NWR193UC, Excimer
Ablation cell	ESI NWR TwoVol2
Laser wavelength	193 nm
Pulse width	<5 ns
Fluence	6.6J/cm ²
Repetition rate	4 Hz
Spot size	25 μm
Sampling mode/pattern	Single spot
Carrier gas	100% He, Ar make-up gas and N ₂ (3 ml/min) combined using in-house smoothing device
Background collection	20 seconds
Ablation duration	60 seconds
Wash-out delay	15 seconds
Cell carrier gas flow (He)	0.76 l/min
ICP-MS Instrument	
Make, Model & type	Agilent 7700x, Q-ICP-MS
Sample introduction	Via conventional tubing
RF power	1350 W
Sampler, skimmer cones	Ni
Extraction lenses	X type
Make-up gas flow (Ar)	0.67 l/min
Detection system	Single collector secondary electron multiplier
Data acquisition protocol	Time-resolved analysis
Scanning mode	Peak hopping, one point per peak
Detector mode	Pulse counting, dead time correction applied, and analog mode when signal intensity $>\approx 106$ cps
Masses measured	²⁹ Si, ³¹ P, ⁴⁹ Ti, ⁸⁹ Y, ⁹³ Nb, ¹³⁹ La, ¹⁴⁰ Ce, ¹⁴¹ Pr, ¹⁴⁶ Nd, ¹⁴⁷ Sm, ¹⁵³ Eu, ¹⁵⁷ Gd, ¹⁵⁹ Tb, ¹⁶³ Dy, ¹⁶⁵ Ho, ¹⁶⁶ Er, ¹⁶⁹ Tm, ¹⁷² Yb, ¹⁷⁵ Lu, ¹⁷⁸ Hf, ²⁰⁴ (Pb + Hg), ²⁰⁶ Pb, ²⁰⁷ Pb, ²⁰⁸ Pb, ²³² Th, ²³⁸ U
Integration time per peak	10 ms
Total integration time per reading	260 ms
Sensitivity / Efficiency	22000 cps/ppm Pb (50 μm , 10 Hz)
Data Processing	
Gas blank	20 seconds on-peak
Calibration strategy	NIST 612 as primary reference materials, 91500 zircon as secondary reference materials (quality control)
Reference Material info	NIST 612 91500 (Wiedenbeck et al., 2004)
Data processing package used	Iolite 4 (Paton et al., 2010)

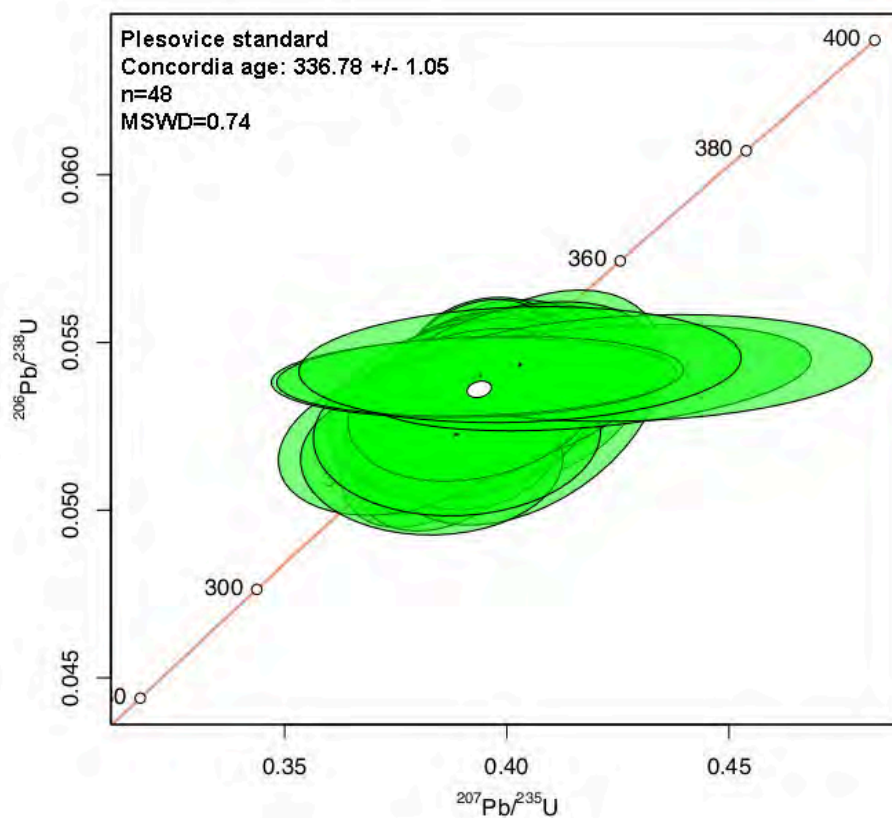


Figure D1: The analysis of the Plešovice standard yielded a concordia age of 336.78 +/- 1.05 Ma (n=48 and MSWD=0.74). The accepted value for Plešovice is 337 +/- 0.4 Ma.